Graduate Theses and Dissertations   Graduate School

April 2018

Initial Beam Access Schemes for Millimeter Wave Cellular Networks

Mohammed Jasim
University of South Florida, jasim@mail.usf.edu

Initial Beam Access Schemes for Millimeter Wave Cellular Networks

by

Mohammed Jasim

A dissertation submitted in partial fulfillment
of the requirements for the degree of
Doctor of Philosophy
Department of Electrical Engineering
College of Engineering
University of South Florida

Major Professor: Nasir Ghani, Ph.D.
Ismail Uysal, Ph.D.
Mahshid Naeini, Ph.D.
Yao Liu, Ph.D.
Chadi Assi, Ph.D.

Date of Approval:
March 22, 2018

Keywords: 5G, beamforming, sparse channels, meta-heuristic, link recovery

Dedication

This dissertation is dedicated to my role models in life, my parents Akeel and Wafa, for their tremendous motivation for higher education, to my lovely princesses, Sara and Wanas, to my brother Fadhil, and to Omar, my best friend of all times.

Acknowledgements

Table of Contents

List of Tables

List of Figures

Abstract

Millimeter wave technologies present an appealing solution for increasing data throughputs as they provide abundant contiguous channel bandwidths as compared to conventional microwave networks. However, millimeter wave technologies suffer from severe propagation limitations and channel impairments such as atmospheric attenuation and absorption, path and penetration losses, and blockage sensitivity. Therefore, phased arrays and beamforming technologies are necessary to compensate for the degraded signal levels due to the aforementioned factors. Namely, base stations and mobile stations utilize directional transmission in the control- and data- plane for an enhanced channel capacity, which results in initial access challenges due to the absence of omni-directional transmission. Here the base station and mobile station are compelled to exhaustively search the entire spatial domain, i.e., in order to determine the best beamforming and combining vectors that yield the highest received signal level.

Overall, a wide range of studies have looked at the initial beam access challenges in millimeter wave networks, with most efforts focusing on iterative and exhaustive search procedures, as well as subarrays schemes and out-of-band beam access. However, these studies suffer from significant signaling overhead attributed to the prolonged beam scanning cycle. In particular, access times here are excessively high that exceed control plane latencies and coherence times. Furthermore, existing work suffer from high computational complexity, power consumption, energy inefficiency, as well as low directivities and high outage probabilities.

In light of the above, the contributions in this dissertation propose fast initial beam access schemes based upon novel meta-heuristic search schemes and beamforming architectures. These contributions include modified search procedures inspired by Nelder Mead, Luss-Jaakola, divide-and-conquer with Tabu search, generalized pattern search, and Hooke Jeeves methods.

Furthermore, efficient and highly-directive access schemes are also developed in this dissertation levering sidelobe emissions, grating lobes and Hamming codes. The overall performance of the proposed solutions here is extensively evaluated versus traditional access schemes and incorporating different channel and path loss models.

Finally, this dissertation addresses the problem of link sensitivity and blockage effects in millimeter wave networks, a subsequent stage to beam access and link association. Nevertheless, a novel link recovery procedure is proposed here that features instantaneous link-recovery and high signal levels.

Chapter 1

Introduction

This dissertation addresses initial beam access using beamforming solutions in standalone millimeter wave (mmWave) cellular networks with sparse poor-scattering channels and propagation limitations. To properly introduce the work, this chapter briefly outlines the key benefits of mmWave technologies, and the major requirements for beamforming designs. The beam access problem is then introduced along with the overall motivations of this thesis. The core research contributions are then briefly highlighted followed by the dissertation outline.

1.1 Background Overview

Recently, the *3rd Generation Partnership Project* (3GPP) finalized the *new radio* (NR) spectrum as part of its 5G Phase I [1]. The main requirements for 5G transmission include 10 gigabits/sec (Gbps) throughput rates, 1 ms latency (versus 50 ms in 4G systems), much improved energy efficiency, and much higher density and coverage. Furthermore, mmWave transmission is also being promoted as a core technology for 5G systems to meet aforementioned requirements, i.e., as part of the NR for *enhanced mobile broadband* (eMBB) framework. Overall the move to mmwave frequencies has been driven by extreme spectrum congestion in current microwave cellular networks. This bottleneck is becoming a major impediment towards bandwidth throughput scalability. Furthermore, related bandwidth shortage and fragmentation concerns at decimeter *radio frequency* (RF) ranges is also limiting bandwidth growth, i.e., since most current allocations are below 100 MHz. By contrast, the mmWave bandwidth range extends from 500 MHz–2 GHz and provides abundant underutilized contiguous bandwidth regions for 5G

transmission. As a result, the United States *Federal Communications Commission* (FCC) has proposed the auctioning of *extremely high frequency* (EHF) bands, i.e., 27.5–28.35 GHz and 37–40 GHz ranges for commercial 5G cellular deployment [2]. In general, this trend follows the standardization of unlicensed bands, such as 57–71 GHz for wireless local area networks (WLANs) and will provide a 10–20 fold increase in carrier aggregation over current 4G systems.

Overall contiguous spectrum ranges offer a very suitable means for wideband single-carrier transmission. As a result, mmWave technologies can eliminate some of the key challenges associated with 3.9G *long term evolution* (LTE) and 4G *LTE-Advanced* (LTE-A) networks, i.e., such as adaptive subcarrier channelization and assignment, frequency synchronization, and phase noise. However, these higher-frequency spectral regions also suffer from very notable propagation impairments, e.g., including path loss, oxygen absorption, atmospheric attenuation, penetration losses, diffraction, and high reflection coefficients. The latter can result in further isolation between indoor and outdoor networks. Furthermore, mmWave systems are also characterized as power- and noise-limited rather than bandwidth- and interference-limited for conventional cellular networks. Finally, mmWave bands suffer from high noise power and poor channel characteristics, i.e., hence a sparse structure.

In light of the above, a host of challenges need to be investigated before mmWave technologies can be deployed in future 5G cellular networks. A major concern here is the use of omni-directional transmission, which introduces prolonged delay spread and severe *inter-symbol interference* (ISI) distortion in received signals. Now in general, these effects can be mitigated using beamforming arrays, i.e., where energy is captured from a reduced number of directions. Now most consider the fact that most mmWave wavelengths fall in the 5-10.7 mm range between 28-73 GHz, i.e., as per the wavelength-frequency equation, $\lambda = c/f_c$, where λ, c and f_c

denote the wavelength frequency, speed of light and carrier frequency, respectively. As a result, compact arrays can be designed for *mobile station* (MS) nodes using the same antenna sizes of current commercial systems: for example a 4x4 array with a dipole antenna size of $\lambda/2$ at 28 GHz will occupy approximately 1.5 x 1.5 cm^2 and can be incorporated in-package or on a chip at low cost [2]. As a result, compact substrate frontends can be designed for mmWave systems, thereby facilitating use of beamforming techniques to overcome channel and propagation deficiencies.

Now recent studies have shown that steerable beamforming technologies can significantly mitigate limitations in mmWave transmission [3]-[5]. Foremost, beamforming gains can help improve link margins, e.g., by compensating for severe path losses (30 dB at 200 m), overcoming noise power, and deploying high order modulation techniques with 512 or 1,024 *quadrature amplitude modulation* (QAM) constellations. In turn, these gains will improve the Shannon channel capacity and increase spectral efficiency. In addition, beamforming methods can also minimize the *root mean square* (RMS) delay spread and eliminate the need for sophisticated equalization requirements. Finally, these strategies can also reduce multi-user interference and lower delay spreads associated with large coherence bandwidths. As a result, phased arrays and beamforming technologies provide a very viable means to handle signal degradation in mmWave systems and extend coverage ranges for indoor users. Lowered footprints high reuse-factors at mmWave frequencies will also improve user density and bandwidth reuse/scalability.

1.2   Problem Statement

Despite the merits of using beamforming between *base stations* (BS) and *mobile stations* (MS), directional transmission and reception introduces key beam access challenges prior to data transmission, i.e., beam search or beam discovery. Namely, initial beam access requires beam

acquisition and association during the transition from sleep to idle mode, as shown in Figure 1.1. As a result, MS and BS nodes have to sweep over the entire azimuth or elevation planes to determine the best beam with the highest received signal level for sparse arrival clusters profile (in the time and space domains). Now traditional exhaustive beam search methods have very high computational burdens since both sides (BS, MS) must test all possible beamforming and combining vectors. This brute-force approach also results in increased signaling delays and prolonged access times, thereby worsening control plane latency (possibly exceeding mmWave channel coherence times). Further downsides also include RF power consumption (energy inefficiency) and time-frequency resource dissipation. As a result, efficient adaptive access techniques are vital for the proper realization and standardization of mmWave bands for cellular networks.

1.3 Motivations

As noted earlier, mmWave frequencies form a major component of the NR interface for eMBB transmission. Accordingly, the *International Mobile Telecommunications* (IMT) framework [1] specifies low control plane latencies for eMBB, i.e., below 10 ms. As a result it is essential to meet this design requirement for 5G systems, i.e., in addition to earlier-detailed requirements along with the computational complexity, time, power and energy metrics associated with beam access, as shown in Chapters 2 and 3. Overall, these challenges mandate the realization of new and improved access techniques that can operate with directional detection periods well below mmWave channel coherence times. Furthermore, fast beam access methods are also required for low-latency handovers, e.g., such as in frequency selective-fading channels and large Doppler spreads for high speed users.
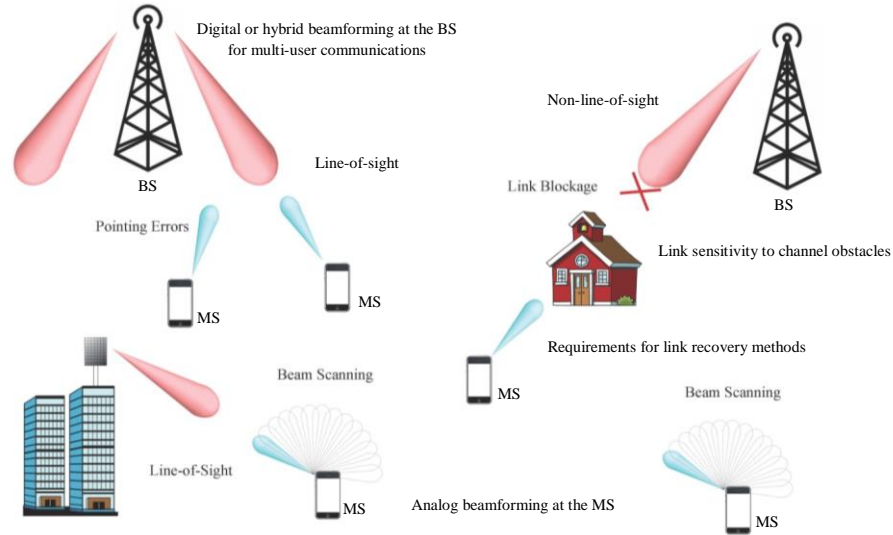
Figure 1.1: Directional transmission and reception between BS and MS nodes

In light of the above, this dissertation develops some novel fast and adaptive initial beam access techniques based upon meta-heuristic search methods and various beamforming architectures. These solutions feature low computational complexity, rapid access times, low power consumption levels and high energy efficiencies compared to many competing alternatives. Furthermore, the proposed methods are evaluated against various proposed alternatives in terms of key design metrics, e.g., such as computational complexity, access times, power consumption, energy efficiency, success rates, outage probability and directivity. Carefully note that this dissertation study does not assume omni-directional support from microwave frequencies in outdoor environment, i.e., microwave-assisted beam access, thereby enhancing standalone mmWave access performance.

1.4 Contributions

This dissertation addresses beamforming challenges in mmWave systems and proposes novel initial beam access schemes. The main contributions in this work are summarized as follows:

- Comprehensive survey on exiting mmWave access schemes

- Robust meta-heuristic schemes for adaptive beam search based upon observed objective function outputs, i.e., based upon *Nelder Mead* (NM), *Luus Jaakola* (LJ), *coordinated generalized pattern search* (CGPS), *divide-and-conquer* with *Tabu search* (DC-TS), and *Hooke Jeeves* (HJ) methods

- First in depth study of poor scattering properties in mmWave channels, including *bi-static radar cross section* (BRCS) modeling of geometric objects in propagation link

- Direct-pattern search scheme to capture sparse cluster arrival rates and help mitigate aggregated rays profile during directional search

- New simultaneous beam transmission model for analog beamforming architectures. First known solution for multi-beam transmission via a single RF chain

- New beam coding scheme for simultaneous transmitted beams based upon orthogonal extended Hamming codes, i.e., to generate distinguishable beams spatial directions

- First known use of grating lobes in analog beamforming to improve transmit diversity, directivity and detection probabilities for wide-beam access codebooks

- Novel sidelobe-based access scheme to reduce access times, representing one of the first such studies on sidelobe exploitation

- Bundle-beam beamformer design to enhance transmit diversity and improve richness of sparse scattering profile

- Detailed analysis of geometric channel model to fit mmWave channel delay profile, i.e., by considering aggregated rays within sparse clusters

Overall, the remainder of the dissertation is as follows. Chapter 2 presents an overview of mmWave channel and propagation characteristics, related design challenges, and a

6

comprehensive survey of current beam access techniques. Subsequently, novel beam access schemes based upon a range of meta-heuristic methods are introduced in Chapter 3. Chapter 4 then presents improved access solutions based upon phased arrays and beamforming architectures. A novel link recovery method based upon hybrid beamforming for near-instantaneous recovery times is also proposed in Chapter 5. Overall conclusions and future directions are then presented in Chapter 6.

Chapter 2

Background

This chapter presents an overview on mmWave channel propagation characteristics, along with a review of existing beamforming architectures and hardware design challenges. A comprehensive survey of existing initial beam access methods is then presented.

2.1 Millimeter Wave Propagation Characteristics

In order to properly detail the key challenges facing initial beam access in mmWave systems, it is important to first detail the main characteristics and properties of the associated transmission channels. In general, signal propagation through any wireless channel is impacted by a host of large and short scale fading properties, i.e., including path loss, diffraction, reflection and penetration, scattering, Doppler effects and delay spread. In turn these factors require effective and precise transceiver modeling and design at the physical and medium access layers. Along these lines, this section overviews the key channel propagation characteristics affecting mmWave channel transmission.

2.1.1 Path Loss

Path loss represents the loss of signal power as transmission propagates through a medium. In general, this value increases proportional to carrier frequency increments, i.e., based upon Friis transmission theory which equates *effective isotropic radiated power* (EIRP), power flux density and overall power levels at the MS and BS. To better illustrate relationship between path loss and frequency, Table 2.1 summarizes free-space path loss values at *ultra-high*

frequencies (UHF) conventional (microwave) cellular bands (460 MHz and 2.4 GHz), WLAN bands (2.4 GHz), and licensed/unlicensed mmWave bands (28, 38, and 73 GHz) at 100 m and 200 m separation distances. Clearly, the mmWave bands experience the most severe losses, i.e., 91.38-105.7 dB range to 67.55-76.06 dB for the other bands. However this link degradation can be compensated for by implementing antenna array gains. In other words, the same amount of energy can be captured as in conventional frequencies via increased aperture sizes. Furthermore, these requisite array gains in mmWave transceivers can still be achieved using similar physical aperture sizes as in quasi-omni antennas used in microwave transceivers. This mitigates wavelength dependence, allowing the aperture size to remain constant regardless of the operating wavelength. In short, larger large aperture sizes yield frequency-independent received power levels.

Table 2.1: Path loss levels at microwave, WLAN, and mmWave frequencies

Separation Distances (meters)	Microwave Frequencies	WLAN	mmWave Frequencies		
	1.8 GHz	2.4 GHz	28 GHz	38 GHz	73 GHz
100	67.55 dB	70.04 dB	91.38 dB	94.04 dB	99.71 dB
200	73.57 dB	76.06 dB	97.40 dB	100.1 dB	105.7 dB

To date, various measurement campaigns have been done for ultra-dense outdoor environments in order to model large-scale fading in rich reflective environments [6]-[8]. These effects utilize horn antennas with *half-power beamwidth* (HPBW) of 30^0 and 15 dBi gains. Also, BS and MS separation distances are varied from 10-450 m in *line-of-sight* (LoS) and *non-line-of-sight* (NLoS) settings. Overall, the recorded *power delay profiles* (PDP) show sparse *multipath components* (MPC) with high excess delays times. For example, the number of distinguished

resolvable MPCs is 8 in LoS setting (for $d \leq 200$ m) and 7 in NLoS setting (for $d \leq 100$ m).

Furthermore, access delay times at a distance of 50 m are recorded as 745 ns in LoS and 1,389 ns

in NLoS environments. Meanwhile, the *path loss exponents* (PLE) are measured as 2.3 dB and

3.9 dB for LoS and NLoS settings, respectively. Overall, these empirical findings indicate that

mmWave systems must handle a limited number of MPCs with large excess delays, i.e., sparse

clusteral arrival rates. These conditions impose further challenges for precise channel estimation,

i.e., in terms of *angle of arrival* (AOA), *angle of departure* (AOD), and path gains in highly-

dispersive channels (e.g., rapid channel fluctuations).

2.1.2   Diffraction

In general, diffraction defines the propagation of radio signals around an object. Hence

this effect impacts link detection when a MS is blocked or shadowed by an obstacle, or when a

MS transits from LoS to NLoS transmission. Now diffraction introduces high levels of signal

attenuation for small fractional movements at mmWave frequencies. For example, diffraction

losses are estimated at 30 dB when a MS node moves around the corner of a concrete building

structure at a frequency of 73 GHz as observed in [9]. Similarly in indoor networks, the signal

attenuation of diffracted signals is more severe at mmWave frequencies, e.g., about 10 dB

attenuation when a MS moves around a corner, and about 40 dB when a MS moves behind an

elevator shaft, see [10]. Overall, diffraction presents the weakest propagation component

impairment in mmWave mobile systems due to the relatively small wavelengths involved.

Meanwhile, scattering and reflection effects tend to be more dominant. These conditions contrast

with microwave frequencies, where scattering is the weakest propagation phenomenon and

diffraction offers favorable and robust signal propagation characteristics. However, beamforming

solutions at the MS and BS can still overcome diffraction-based attenuation effects by using

beam-steering techniques, i.e., in order to allocate reflections and scattered paths from nearby buildings or surfaces.

2.1.3   Reflection and Penetration

As noted in [11] and [12], mmWave transmission exhibits high reflection coefficients, i.e., low penetration levels for indoor and outdoor environments. For instance, the reflection coefficients of tinted glass and concrete materials are on the order of 0.88 and 0.80 at 10^0 beamwidth, respectively. In other words, mmWave signals cannot penetrate significantly through outdoor materials, i.e., 80-88% of incident waves are reflected with high penetration losses nearing 40 dB, i.e., weak reflected waves. Additionally, transparent glass and dry wall reflection coefficients have also been recorded at 0.75 and 0.71, respectively [13]. Overall, these high coefficients yield reduced interference levels at the detriment of isolated indoor and outdoor networks, i.e., more relays are required for connectivity. Consequently, higher synchronization and handover challenges are introduced here. Furthermore, beamforming solutions are also required to compensate for penetration levels and improve link margins, i.e., by taking into account angular spreads.

2.1.4   Doppler Effect

The Doppler effect represents a change in wavelength/frequency of an incoming signal at a moving receiver. Namely, the received frequency, f_d, is now dependent upon the receiver velocity, v, transmitter velocity, v_o, carrier frequency f_c , and is given by:

$$f_d = \left(\frac{c+v}{c-v_o}\right)f_c - f_c = f_c\left(\frac{c+v}{c-v_o}-1\right),$$

(2.1)

where f_c is the carrier frequency and c is the speed of light constant. From the above, a significant increase in Doppler effect can be caused by increments in carrier frequency or MS velocity. Overall, Doppler effects are expected to be 15-35 times greater at 28-73 GHz mmWave

bands versus microwave bands. Accordingly, Table 2.2 compares the Doppler levels at mmWave (73 GHz) and microwave frequencies (1.8, 28, and 38 GHz) for relatively slow and fast velocities. For example, consider a MS communicating at a carrier frequency of 38 GHz and travelling at a velocity of 100 km/sec. The Doppler spread here is 3.52 KHz compared to 164.38 Hz at 1.8 GHz for the same MS speed, i.e., 20 times higher.

Table 2.2: Doppler spread at different MS speeds for mmWave and microwave frequencies

MS Speeds	mmWave Frequencies			Microwave Frequencies
	28 GHz	38 GHz	73 GHz	1.8 GHz
1 m/sec	186.66 Hz	253.33 Hz	486.66 Hz	12 Hz
100 km/hr	2.6 KHz	3.52 KHz	6.76 KHz	163.38 Hz

Overall, the high Doppler rates here mandate adaptive and fast beam-tracking algorithms, i.e., with beam-switching times much lower than the coherence times needed to retrain communication sessions. In general, beamforming gives a limited number of specular-diffused MPCs, i.e., defined by the *two-wave with diffuse power* (TWDP) distribution [14]. Furthermore, when taking into account Doppler effects in time-varying channels, signal fading distribution will also depend upon the beamformer HPBW and number of MPCs. Hence the requistie fading channel models incorporating Doppler effects tend to follow a bi-modal *probability distribution function* (PDF) shown in [14]. Furthermore, the associated coherence time here (inversely proportional to Doppler spread) also depends on the beamwidth, frequency, system bandwidth and MS velocity.

Overall, mmWave channels will vary more rapidly in time in the presence of Doppler effects, i.e., mmWave channels fluctuate 10 times faster when Doppler spread is increased by a

factor of 10. Therefore channel retraining times and transmission frame sizes need to be proportionally reduced, since the Doppler spread range determines the time interval over which the channel is static. As a result, shorter frame times and packets durations are required for mmWave systems, i.e., commensurate with the low-latency requirements [15]. Indeed, the channel time interval is a crucial parameter in the design of phase shifters (e.g., beam-switching speed), equalizers, and encoders.

In light of the above, new mmWave channel tracking algorithms need to be developed to incorporate beamwidth, channel *impulse response* (IR) and motion speed at shorter synchronization times and symbol times. Expectedly, frame times and packet durations will be proportionally reduced when transferring operating frequencies from the microwave to mmWave bands. Note that this reduction can also be achieved by improved coherence times due to beamforming utilization.

2.1.5 Scattering

Unlike microwave bands, scattering is a critical propagation phenomenon at mmWave frequencies, i.e., since physical objects and obstacles in the channel are relatively larger than the propagated wavelength (e.g., pedestrians, lamp-stops, cars and walls). As a result, illuminated scatterers can build substantial mmWave propagation paths, i.e., enriched multipath profiles. Now the impact of scattering in any propagation environment is largely determined by the *radar cross section* (RCS) of its obstacles, i.e., in addition to surface roughness. Specifically, the received power from a scattered wave is a product of the RCS of a particular obstacle and the scattered field. Now the RCS profile defines the electromagnetic field scattering behavior of an object, i.e., it represents an object in terms of an aperture with a particular area (measured in m^2). Furthermore, this value can be categorized into *monostatic cross section* (MCS) and *bi-static*

cross section (BSC) components. Namely, the MCS portion relates to backscattering and defines an electromagnetic field scattering in the direction of the transmitter (BS) when the receiver (MS) and transmitter are co-located. Meanwhile, the BSC portion defines an electromagnetic field scattering at the receiver when the transmitter and receiver are not co-located. Specifically, the BSC of an obstacle is defined as [16]:

$$\sigma_{3D}= \lim_{r\to\infty}\left[\frac{4\pi r^2 S_s}{S_i}\right]= \lim_{r\to\infty}\left[\frac{4\pi r^2 |E_s|^2}{|E_i|^2}\right], \tag{2.2}$$

where σ_{3D}, S_s and S_i denote the 3-dimensional RCS, the scattered power density, and the incident power density, respectively. Furthermore, the variables E_s, E_i and r in Eq. (2.2) represent in order the scattered electric field, the incident electric field, and the distance between the transmitter and receiver. Note that Eq. (2.2) ignores polarization effects, i.e., the low cross-polarization properties at mmWave bands. Furthermore, the RCS-based received power from a scattered ray is given by [17]:

$$P_r[\text{dBm}]=P_t[\text{dBm}]+G_t[\text{dBm}]+20\log_{10}\lambda +\text{RCS}[\text{dBm}^2]\text{-}30\log_{10}(4\pi)\text{-}20\log_{10}(d_t)\text{-}20\log_{10}(d_r), \tag{2.3}$$

where P_t, P_r, G_t, d_t, d_r denote in order the transmit power level, the received power level, antenna (or array) gain at the transmitter, the separation between the scattering object and transmitter antenna, and the separation between the scattering object and receiver antenna. Hence, higher power levels can be received from a scattered ray from object with higher RCS values.

Furthermore, the impact of the surface roughness of an obstacle is also essential in modeling its scattering properties, e.g., intensity, direction and power level. For example smooth surfaces are less common to exist in outdoor settings, i.e., dominated by concrete and bricks, whereas indoor settings generally have smoother scattering slabs. Now the total RCS of a rough

surface can be derived based upon the scattering properties of a smooth surface summed over the cross-sectional scattering area (attributed to surface roughness) [18],[19]:

$$\sigma_{tot} = \sigma_{tot} + |X_s|^2 \sigma_{smooth}, \tag{2.4}$$

where σ_{rough} and σ_{smooth} are the scattering areas of the rough and smooth surfaces. Meanwhile, X_s in Eq. (2.4) represents the surface roughness and is given by [19]:

$$X_s = \exp(-k_0^2 \langle h_s^2 \rangle^2 \cos^2(\theta_i)) = \exp\left(-\left(\frac{2\pi}{\lambda}\right) \langle h_s^2 \rangle^2 \cos^2(\theta_i)\right), \tag{2.5}$$

where k_0, $\langle h_s^2 \rangle$, and θ_i denote in order the wave number, average surface roughness (i.e., mean square height of the small-scale features of the surface), and the incident angle, respectively. Carefully note that the impact of scattering becomes more negligible in determining the total RCS of the scatterer as the surface roughness increases. Here σ_{rough} in Eq. (2.4) is basically determined by the reflection coefficient of a rough surface given by [19]:

$$\sigma_{rough} = R e^{-2k_0^2 \langle h \rangle^2 \cos(\theta_i)}, \tag{2.6}$$

where R is the specular reflection coefficient for waves scattering off smooth surfaces. Also note that the scattering direction for smooth surfaces is specified by Snell's law.

Overall, an object's roughness levels are considerably higher at mmWave frequencies as compared to microwave frequencies. Meanwhile, illuminated smooth surfaces, e.g., such as outdoor lampposts and road signs, also contribute more to the multipath profile at mmWave frequencies than at microwave frequencies [20],[21]. Nevertheless, rough surfaces here are less effective in shaping the received profile, i.e., since the physical and electrical sizes of these surfaces largely exceeds mmWave wavelengths. Hence these surfaces tend to contribute to signal degradation, e.g., high penetration losses, and blockage. In short, illuminated smooth surfaces

such as lampposts and other metallic outdoor objects contribute to dominant NLoS paths between a BS and MS at 38 and 60 GHz [22].

2.1.6 Delay Spread

Delay spread defines the overall time interval over which the entire temporal MPCs are recorded. In other words, it represents the time difference between the arrival times of the first and last MPC components, i.e., difference between minimum excess delay and maximum propagation time. Meanwhile, the RMS delay spread defines the temporal dispersion between arriving components, e.g., temporal spreading between dominant rays (of each cluster) in the mmWave profile. Additionally, the RMS delay spread is also related to the *power delay profile* (PDP), i.e., mean received power.

Now the delay spread values in mmWave channels differ notably from their counterpart values in microwave channels. This variation is attributed to the use of highly-directional arrays, low angular spreads, and poor-scattering environments. Intuitively, the use of mmWave omni-directional transmission should reduce excess delays and overcome wide noise bandwidths, i.e., due to reduced number of received MPCs with high *signal-to-noise ratio* (SNR). Therefore the impact of beamwidths has to be taken into account when modeling delay spreads. Now outdoor channel measurements at 28 and 38 GHz in [23],[24] have shown that wide beams yield larger delay profiles and smaller PLEs versus to narrow beams over shorter distances. These changes are caused by larger aperture sizes at wider beams, i.e., as needed to capture more incident energy. However, small array gains become ineffective over larger distances in NLoS settings. Overall, the use of beamforming in mmWave systems helps shorten delay spreads, and hence the scale of frequency selective-fading is lower than microwave systems (which utilize quasi-omni and omni-directional transmissions).

2.2 Design Constraints and Challenges

In addition to channel impairments and propagation limitations, mmWave transceiver designs also face many additional challenges and constraints. Some of these are now detailed.

2.2.1 Radio Frequency (RF) Safety Requirements

Generally, mmWave radiation is non-ionizing in nature. Hence the main health and safety concern at these frequencies is RF heating, i.e., limiting exposure to mmWave radiation when the user is in the near field of radiating sources (MS device). As a result, power flux density limits in the near field should be regulated to determine limits for tissue heating as noted in [25]. Now carefully note that beamforming can control the amplitude and phase in antenna arrays to create destructive or constructive electric field patterns near the surface of the body, i.e., see Figure 2.1 [25]. Therefore, the overall exposure to heat radiation can be compensated for by using beam-steering arrays. For example, experiments in [26] have shown that the use of such techniques reduces penetration depth and power absorption in the head and skin to 3 mm and 90 mW/g, respectively, i.e., versus 40-45 mm and 1 mW/g at microwave ranges (see also Figure 2.1).

2.2.2 Noise Bandwidth Limitations

In general, mmWave channels operate at bandwidths ranges between 0.5-1 GHz versus 5-20 MHz in LTE networks. Consequently, increased noise power levels are introduced for larger mmWave bandwidths, i.e., since noise power spectral density is constant. Furthermore, these noise levels cannot be compensated for by simply increasing transmitted power levels, i.e., transmitted power cannot exceed a few *milliwatts* (mWatts) due to RF safety corners. As a result, a more feasible approach for improving SNR is to use larger antenna gains.
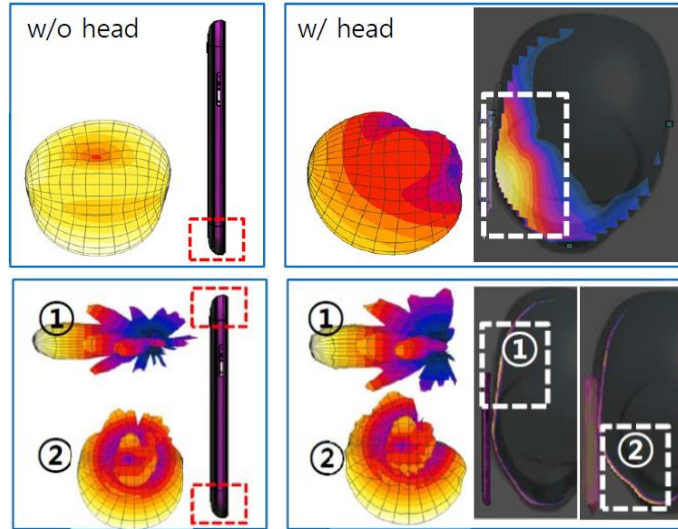
Figure 2.1: MmWave RF heating at surface of human head

2.2.3 Power Consumption

Hardware power consumption presents another significant performance consideration for mmWave transceivers, i.e., as these designs have many components such wideband signal processing chips, large number of arrays, mixers, phase shifters, filters and amplifiers. As a result, power consumption tends to increase linearly with sampling rate and exponentially with the number of bits/samples [27],[28]. In light of the above, power consumption efficiency should also be taken into account here, particularly for the design of beamforming architectures.

2.3 Beamforming Architectures

Now various beamforming techniques have been used in earlier 4G networks based upon open- and closed- loop configurations with 2-8 antennas [29], i.e., to complement data-plane stage and improve spectral efficiency. However, this stage follows the control-plane procedure that is performed in omni-directional mode. Overall, this 4G approach contrasts with mmWave systems, where beamforming is used in both the control- and data- planes, e.g., with larger 32-256 antenna elements. Additionally, traditional beamforming systems require limited feedback (information transmission) from the MS to the BS to determine instantaneous *channel state*

information (CSI), i.e., since the channel can be estimated by the MS. However this simplified strategy is infeasible in mmWave systems owing to shorter coherence times. Instead, a blind beamforming technique is the most viable solution for mmWave transceivers. In addition, earlier beamforming techniques also perform signal processing at microwave bands in the digital baseband domain, i.e., versus mmWave bands which require spatial filtering in the analog domain. Overall, beamforming architectures in mmWave networks impose new design aspects and requirements as compared to conventional cellular networks. Foremost, the reduced dimensionality of mmWave band antennas offers compact packaging and fabrication options in cascaded arrays, e.g., linear, circular and planar arrays. This saliency allows designs to utilize phased arrays for beamforming architectures. Along these lines, several arrays and beamforming designs for mmWave systems have already been considered, and these are now detailed.

Overall, beamforming uses traditional array signal processing and spatial filtering techniques to adaptively control the amplitude and phase weights of multiple signals fed to each antenna. Hence a desired radiation beam pattern can be formed by combining these individual antennas wave-fronts and directing them in the most favorable propagation direction. Beamforming also requires further provisions at both the BS and MS. Namely, both transmit and receive beamforming vectors (combining vectors) are designed based upon array architectures. In general, beamforming sets the maximum link gains by selecting the dominant right and left singular vectors of the complex channel for the beamforming and combining vectors, respectively.

In general, beamforming provides a range of benefits including spatial selectivity, sufficient array gain, enhanced SNR, and improved link quality and margins. As a result, this technique can combat mmWave propagation losses and channel impairments. Beamforming also

provides adaptive beam-steering support to help adjust to rapid channel state fluctuations, i.e., the steering capability captures highest signals from scattering and reflections. Another key benefit here is also null-steering, which can be used for suppressing undesired signals and mitigating *co-channel interference* (CCI), e.g., such as zero-forcing beamforming. Finally, beamforming provides an underlying enabling technology for spatial diversity and spatial multiplexing support to improve spectral efficiency. However, the choice of spatial diversity and spatial multiplexing schemes should always governed by the instantaneous CSI, where switching between these two schemes should be considered. Overall, several types of beamforming architectures have been studied for mmWave systems, including analog, digital, and hybrid solutions. These architectures are now overviewed.

2.3.1 Analog Beamforming Schemes

Analog beamforming techniques use a single RF chain connected to an antenna array and a set of phase shifters. In particular, Figure 2.2 illustrates the main components of the analog beamformer composed of digital baseband unit, single RF chain, phase shifters, antennas and *low-noise amplifiers* (LNA). This design generates a single-beam radiated along a particular direction, i.e., single data stream. Now beamforming is done here in the analog domain after the up-conversion to envelope-carrier frequencies. Specifically, analog beam-steering control is performed at intermediate frequencies using selective RF switches and passive or active phase shifters as proposed in [30],[31]. Note that the use of quantized phase shift values and constant modulus constraints imposes limits the choice of phase shifters here, i.e., for highly-adaptive shifting functions. Overall, the digitally-controlled phase shifters implement the core functionality of analog beamforming, e.g., number of phase shift states and switching speeds. As a result, active or passive phase shifter effects have to be taken into account in such designs, e.g.,

including noise and non-linearity, as well as the resolution of the quantized phases (which determines power consumption). In practice, active phase shifters are more favorable owing to their compact physical designs and reduced insertion losses [32].
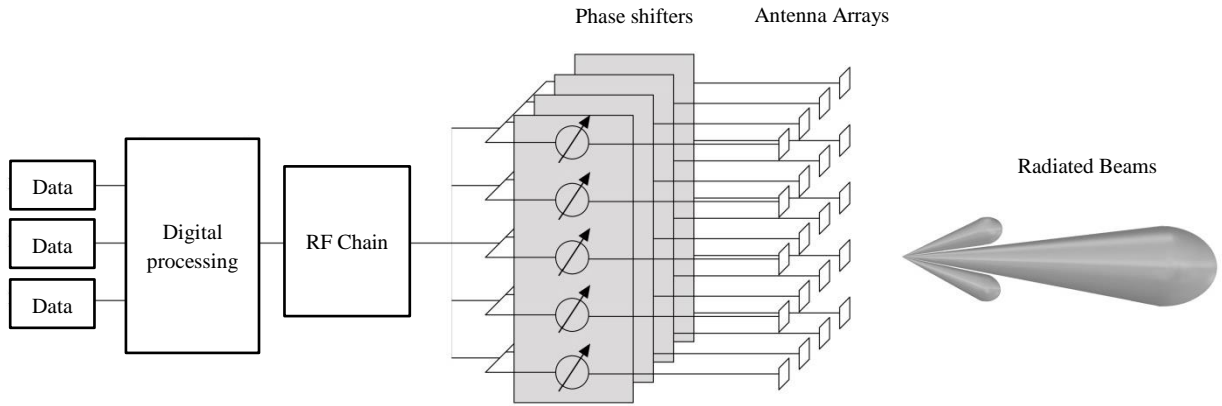
Figure 2.2: Overview of analog beamforming approach

Overall, analog phase shifters are more viable for mmWave systems due to their continuous scanning capability, i.e., unlike digital phase shifters which perform step scanning in discrete directions. In other words, digital phase shifters provide lower switching speeds versus analog shifters, enabling beamformer scanning speeds under excess delay spread. In particular, loaded-line varactor phase shifters present a favorable choice for mmWave analog beamforming due to their wider scanning ranges and nano-second switching speeds. However, the use of a single RF chain here, Figure 2.1, complicates multi-streaming and multi-user transmission support. Hence one feasible solution here is to use sequential multi-streaming via a *time-division multiplexing* (TDM) scheme. Overall, spatial diversity is more suitable for mmWave low-rank channels, e.g., design of simultaneous beam transmission analog beamformers. Another limitation of analog beamforming is beam-squint, also known as beam deflection caused by phase offsets. However, this effect can be mitigated if the antenna array is in the far-field of the impinged-waves (in order to generate planar-waves). This approach can also avoid wave

impingement at the spacing (nulls or gaps) between adjacent antenna elements, i.e., array boresight reception. Regardless, beam-squint becomes negligible when using adaptive phase shifters to adapt beamformer lobe orientations in the best direction. Also, transverse mmWave oscillations generate low cross-polarization (high co-polarization), and this also mitigates beam-squint.

2.3.2 Digital Beamforming Schemes

Digital beamforming dedicates a full RF chain (baseband and RF hardware unit) for each antenna. Namely, the number of RF chains is now equal the number of antennas in the arrays, as opposed to analog beamforming approach which uses single RF chain, see Figure 2.2. Now one of the main benefits is support for precoding and multi-streaming in the digital baseband domain. As a result, digital beamforming offers high a *degree of freedom* (DoF) and improved system performance, particularly in highly-dispersive channels. However, these gains are contingent to high channel rank and rich-scattering properties, i.e., in contrast to mmWave networks that attribute low channel ranks and poor-scattering propagation.

In general, digital beamforming forms the core constituent of *multiple-input multiple-output* (MIMO) architectures and gives the highest spectral efficiency. However, in practice, yhis approach has relatively high power consumption owing to the large number of required components, e.g., such as *power amplifiers* (PA), *digital-to analog-concerts* (DAC), *analog-to-digital-converts* (ADC), *voltage-controlled oscillators* (VCO), baseband filters, and *data interface cards* (DIC). Most notable here are the ADC and DAC components which must run at *giga-sample per second* (Gsample/sec) conversion for the ADC and DAC. Another main limiting factor here is also the physical footprint of digital beamforming devices, i.e., since a separate RF unit and data converter is required for each antenna. As a result, RF components have to be

designed in a compact manner in order to fit into very small physical area. In turn, this presents major fabrication challenges to overcome high substrate losses, along with insertion and return losses, e.g. matching circuits design. Overall, the above factors complicate digital beamforming designs and mandate rather sophisticated RF front-ends.

2.3.3 Hybrid Beamforming Schemes

Hybrid beamforming offers a compromise between analog and digital beamforming in terms of hardware simplicity, power consumption and spectral efficiency. Namely, a limited number of RF chains are now dedicated to a sectional group of antennas, as shown in Figure 2.4. As a result, the number of antennas is larger than the number of RF chains here. Consequently, there are fewer converters per antenna, which helpds lower power consumption overheads versus pure digital beamforming. Note however, that the DoF is also reduced here, i.e., limited simultaneous multi-streaming and multi-user support (equal to the number of RF chains). Also, precoding is now done jointly in the digital baseband and analog domains, and hence the overall precoding matrix is composed of analog and digital beamforming vectors.

Overall, the analog section of hybrid beamformer design (Figure 2.4) can be built using phase shifters, RF switches, or continuous aperture dielectric lens arrays. Specifically, implementing passive lens arrays at the (BS, MS) front-ends offers direct channel access in the beam-space, i.e., by computing a spatial Fourier transform [33]. Carefully note that the design of analog and digital beamforming and combining matrices should also take into account mmWave channel sparsity i.e., by leveraging sparse recovery algorithms for channel estimation.

However, a key limitation with hybrid beamforming is the need for explicit channel estimation, i.e., since the overall precoding matrix is composed of analog precoders and combiners with different constraints. Namely, the mmWave channel here is only seen by the

analog focal lenses, i.e., it is frequency-flat in the analog spatial signal processing domain and frequency-selective in the digital domain (broadband channels). In light of the above, new channel estimation algorithms are required based upon the CSI. Furthermore, hybrid beamforming designs must also be able to enhance the precision of the analog domain, e.g., mitigate residual multi-streaming interference [34].
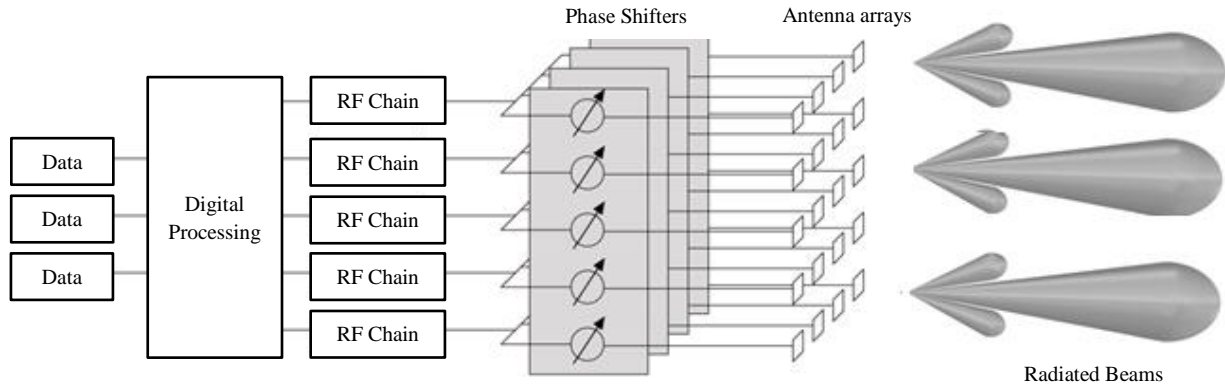
Figure 2.3: Overview of digital beamforming approach

Overall, digital beamforming is a more desirable choice at the BS since it can support multi-user in frequency selective channels. Meanwhile, analog and hybrid solutions are favored at the MS. Now the choice between analog and hybrid beamformers is governed by a range of factors, including SNR regime, battery life, and power consumption levels. Nevertheless, despite the tremendous potential benefits of beamforming design, this directional transmission/reception approach imposes critical initial beam access challenges, as noted in Chapter 1. Hence in order to facilitate the further discussion of initial access in mmWave cellular networks, initial beam access (cell discovery) procedures in conventional LTE networks are presented next.
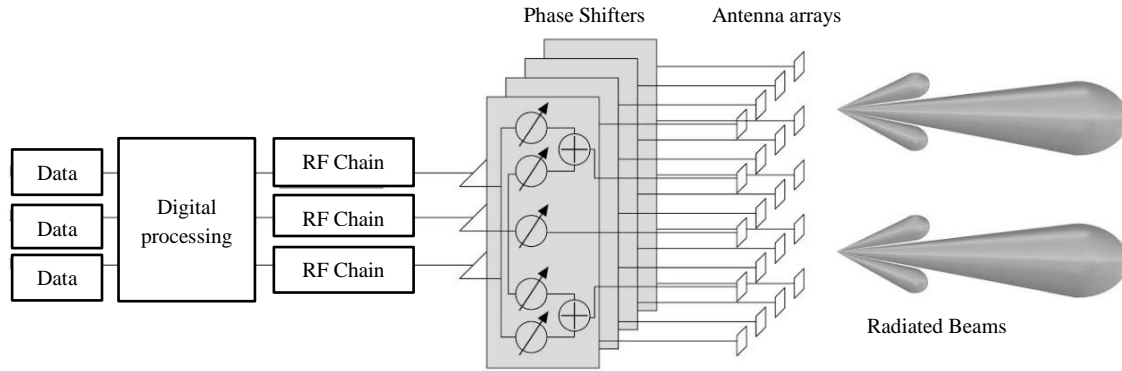
Figure 2.4: Overview of hybrid beamforming approach

2.4 Initial Beam Access in LTE Networks

Initial access in older 3GPP LTE networks is composed of several key steps, including initial synchronization (cell search and cell selection), system information acquisition, and random access. However, this section only addresses initial synchronization procedure, since it is equivalent to mmWave beam access. In general, most LTE networks use a hierarchical search procedure which radio cells are identified. Specifically, 504 physical layer cell identities are defined for LTE, and these are further divided into 168 unique cell layer identity groups in the physical layer. Here each group has also three physical layer identities, and this information is continuously transmitted via *primary synchronization signal* (PSS) and *secondary synchronization signal* (SSS) transmission.

Overall, the LTE cell search procedure is mainly centered around finding the cell identity. Namely, each BS in LTE, also termed as *evolved NodeB* (eNodeB), periodically transmits the two synchronization control signals (PSS and SSS). Meanwhile, the *user equipment* (UE) conducts eNodeB search by scanning different frequency bands, i.e., signal detection is done via an omni-directional antenna. The main purpose here is to detect a PSS transmission and obtain a coarse estimate of the frame-timing, frequency offset, and receive power. Specifically, the PSS is transmitted in the last *orthogonal frequency-division multiplexing* (OFDM) symbol of

the first time slot of the first sub-frame in downlink frame structure, i.e., twice per radio frame. This setup allows a UE to acquire the slot boundary independently from the chosen *cyclic prefix* (CP). Next, the UE searches for the SSS transmission to obtain complete radio frame timing and the cell (eNodeB) group identity. Here the SSS is periodically transmitted in the symbol before the PSS, i.e., in the first and sixth subframes (5 ms periodicity).

After the initial synchronization is completed, the UE decodes the *physical broadcast channel* (PBCH), i.e., which is scrambled and modulated with a cell-specific sequence, Thereafter, the UE retrieves the *master information block* (MIB) and *system information blocks* (SIB), which carry essential system information. The link betweek the UE and eNodeB is now setup for random access, and the user enters idle mode. Overall, this LTE network cell discovery procedure relies upon omni-directional periodic transmission of synchronization signals, i.e., beamforming solutions are not adopted in LTE networks cell discovery. By contrast, 5G cellular networks plan to implement beamforming for initial access for the first time in mmWave systems. As such, related access procedures differ drastically here, as detailed next.

2.5 Related Work on mmWave Initial Access

As opposed to existing LTE access schemes, mmWave initial beam access requires many steps, i.e., control preamble broadcast signaling, BS detection, random access, beam scanning and alignment, and beam refinement. Indeed, this process constituents a major part of mmWave control plane, i.e., to establish mmWave links. As a result, many studies have looked at developing effective, fast and robust access schemes. Hence, this section presents a detailed survey of the most recent solutions here, along with their merits and limitations. In particular, these methods include position context-information methods, single-sided search, exhaustive search, iterative search and auxiliary transceivers schemes.

2.5.1   Position Context Information Methods

Position context schemes assume the availability of *global positioning systems* (GPS) at the MS nodes. Hence geographical context information for the BS beam direction can be retrieved at the MS without the need for spatial domain beam scanning. This information allows a MS node to immediately point its main lobe in the direction of the BS beam, yielding faster/reduced initial beam discovery times. For example, the work in [35] leverages such context information at the MS only to adjust its combining vector in the BS direction in a single step during random access. Nevertheless, the similar use of context information at the BS is not feasible since multiple MS devices can share the same geographical area (with the same best combining vector spatial directions). By contrast, BS nodes generally have unique geographical locations, and hence a MS can probe a single BS to form a single beam in the best direction.

Nevertheless, this GPS-based discovery scheme here suffers from high power consumption as it relies upon continuous GPS connectivity. Moreover this solution is only effective in outdoor settings, and is also highly-dependent upon GPS position accuracy. Furthermore this method will degrade in the presence of sectorization, *remote radio heads* (RRH) deployment, and overlaid BS nodes. Also, this GPS-based discovery scheme has an inherent mismatch scheme has a mismatch between the discoverable area (control-plane range) and the mmWave service area (data-plane range) due to the use of low-resolution beams.

Meanwhile, other studies in [36],[37] also propose an *enhanced discovery procedure* (EDP) to overcome the above limitation. Specifically, GPS information is now used by the BS to estimate MS position based upon user distribution. This data is then conveyed to the mmWave network and leveraged for transmit beamforming directions, i.e., to facilitate synchronization signaling acquisition. Namely, the EDP scheme first scans large azimuth angles and then extends

its range by using narrower beams. Findings show that using sectors marginally improves rendezvous times, i.e., delayed probing of far-away areas. Meanwhile, using a larger number of sectors increases the number of required switches, i.e., heightened sensitivity to azimuthal location errors. For example, 3 sectors are needed for 10 m location accuracy error (120^0 each). However, when location error exceeds 15 m, wider sectors must be deployed. The performance here is governed by user density, user distribution, forbidden zones and position accuracy. Consequently, this scheme degrades significantly in denser MS areas. Overall, the authors recommend using wider sectors at the detriment of low link capacity, i.e., in order to reduce error sensitivity with narrow sectors.

Furthermore, work in [38] proposes a greedy algorithm to reduce the effects of user distribution, termed as *discovery greedy search* (DGS). Here the serving mmWave BS quickly computes the beamwidth and its associated pointing direction when a new MS randomly tries to access the network. Now if the estimated MS position is inaccurate, then the MS is misdetected and the BS tries to scan the region surrounding the MS using circular sectors. Specifically the first scanned sector covers adjacent beam directions using fixed beamwidth in alternating *clockwise* (CW) and *counter-clockwise* (CCW) directions. If the MS is still not detected here, then the BS adaptively reduces its beamwidth and repeatedly directs its transmit vector towards the estimated MS position. Furthermore, if no precise MS is detected after scanning the sector, then same per-sector beam scanning procedure is repeated for all the other adjacent sectors, i.e., alternating CW and CCW sectors. This process either ends with successful or failed MS detection. However, the design of a proper beamforming vector here implies perfect knowledge of path loss and channel models between the mmWave BS and the intended MS (unreliable). In

addition, the best spatial direction estimated by the microwave BS using anchor-based prediction can differ from that seen by the mmWave BS.

2.5.2 Single-Sided Search Schemes

In this scheme, a single side (BS or MS) initially performs directional search while the other side uses omni-directional antenna, then the roles here are reversed. The authors in [39] also propose a combined omni-directional and random directional transmission access scheme in order to reduce the number of measurements and discovery time (search delay). Namely, the BS transmits control signals using an omni-directional antenna, whereas the MS directionally scans the channel domain using a narrow beam hybrid beamformer, e.g., as shown in Figure 2.5 (detection of two MPCs is shown in blue and grey). The MS then selects a random initial main lobe direction and exhaustively scans the entire spatial domain to detect the direction returning the highest signal. As a result, the MS effectively selects a unique beam vector that returns the highest spatial direction. The MS and BS roles are then reversed. Namely, a BS transmits pilot signals in the best direction using narrow beam, whereas the MS uses omni-directional transmission. This approach allows both sides to determine directions for highest signal receptions. Overall, this scheme simultaneously initiates directional transmission and reception for the data plane, i.e., no additional omni-directional transmission is required. Moreover after this handshake, channel estimation is finalized by transmitting the relative channel gains values, along with the estimated AoAs and AoDs.

Nevertheless, omni-directional transmission and reception at mmWave frequencies yields in reduced coverage areas, i.e., less MS and BS separation distance. Hence a further mismatch is introduced between the area at which a MS can detect a BS, and also the area at which a MS can be served by a BS, i.e., distantly located due to the directional beams. Also, omni-directional

transmission does not compensate for high path losses and random sequential search methods also give larger delays. Overall, these limitations mandate the need for more effective beam discovery schemes.
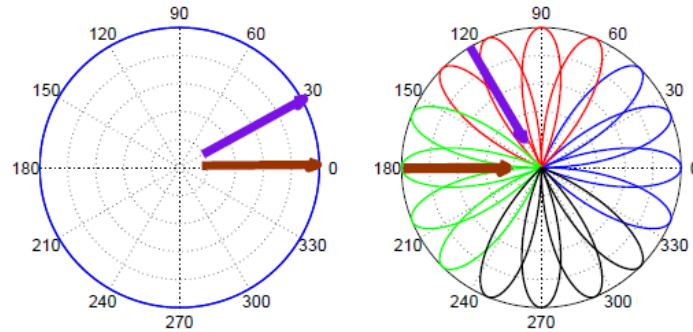
a) BS transmits omni-directional   b) MS scans multiple directions
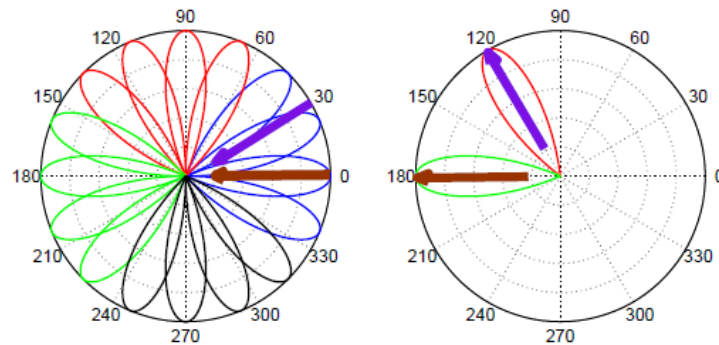
c) BS transmits in the direction of its AoDs   d) MS scans multiple directions

Figure 2.5: Single-sided beam search

2.5.3 Exhaustive Search Schemes

Exhaustive methods perform simultaneous beam search at both the MS and BS nodes. Namely, these scans are done over the entire angular space using narrow beams generated by a high number of antennas, i.e., brute-force method [40]. Both sides start with a random beam direction (such as one of the 64 predefined directions in Figure 2.6) and sequentially scan the entire azimuth plane in a time sliced (TDM) manner. Now when a MS initiates network random access, it essentially probes for synchronization signals transmitted by the BS beamforming

vectors. This technique returns the highest directivity and ranges across all discovery methods, at the expense of very high computational complexity and prolonged access times. Furthermore, the received signal levels at each narrow beam (at the MS) also have to be examined for all beams from the BS, and vice versa. The beam vectors returning the highest signal levels are then selected for data-plane transmission. Nevertheless, this scheme can also yield additional delays for cell discovery due to the random nature of the MS locations and the lack of context information.

a) MS beams   b) BS beams
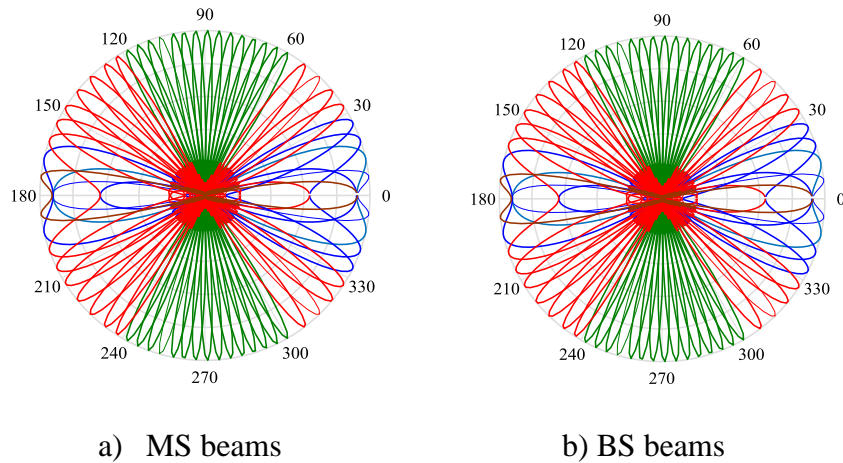
Figure 2.6: Exhaustive search between MS and BS nodes

2.5.4   Hierarchical Codebook Search Schemes

Hierarchical search performs beam scanning over a set of stages composed of wide and narrow beams [41]. This scheme presents a compromise between the omni-directional and exhaustive search methodologies as shown in Figure 2.7. In Stage I, both the BS and MS nodes use the same beam discovery process here, with each one starting a random search with wide beams, see Figure 2.7. Specifically, both sides start with one wide beam and then conduct a sequential search (up to 4 predefined wide beams) in other spatial directions (broadside and end-fire) using the same array size, Figure 2.7(a). Hence, after the scanning cycle is completed, a single wide beam is selected at the MS and BS in the initial stage.

31
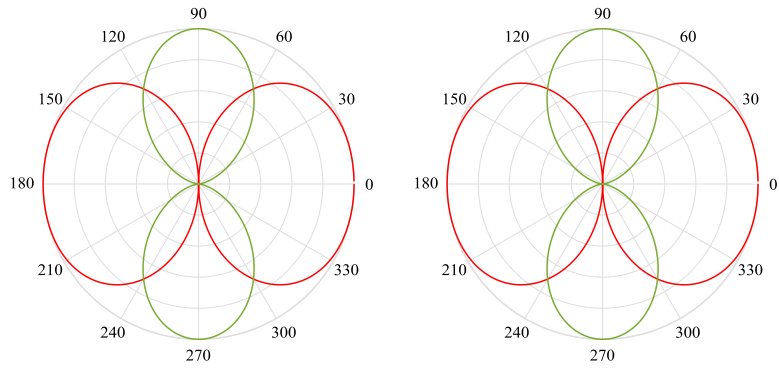
(a) Codebook Stage II: BS and MS beams
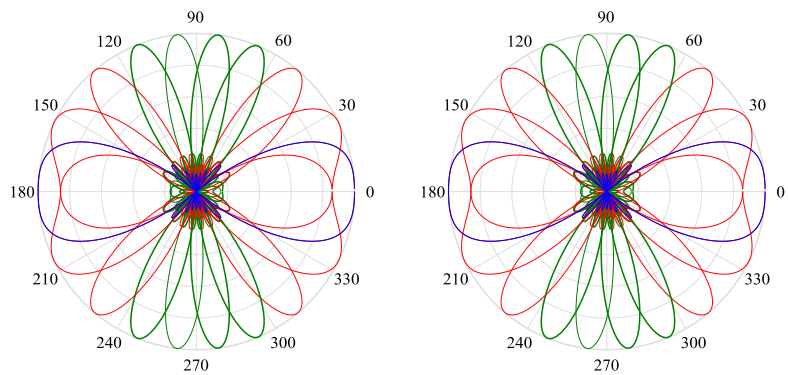
(b) Codebook Stage II: BS and MS beams
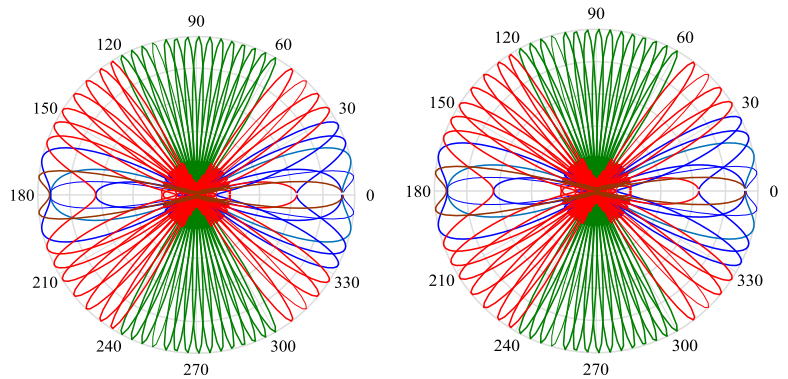
(c) Codebook Stage III: BS and MS beams

Figure 2.7: Hierarchical codebook search between MS and BS nodes

Carefully note that the detection of the best wide beam requires the highest signal within the range of this beam, whereas the other wide beam locations are discarded and are not

considered further in the successive search stages (beam refinement). Based upon this, Stage II further restricts the search to the angular range of the best detected beam, i.e., to better allocate this direction. Namely, a group of narrow beams are defined within this region, and the search is conducted using a single narrow beam over 4 directions selected from 16 beams, e.g., as shown in Stage II in Figure 2.7(b). This search process is repeated in codebook Stage III until the highest signal is detected using a pencil beam, as per Figure 2.7(b).

However, hierarchical codebook search still entails high computational complexity and access times. In addition, the use of wide beams yields lower gain and directivity levels. Finally, selecting an incorrect combiner in the initial scanning stage can also cause access errors in the subsequent refinement stage.

2.5.5 Subarrays Beam Access Schemes

Subarrays access schemes perform beam scanning over a set of cascaded sectional arrays that compose the overall beamformer architecture, where each subarray conducts beam search over a small predefined angular range, i.e., the set of the subarrays here achieve complete search over the entire angular range $[0, 2\pi]$. As an example, the authors in [42] propose a beamtraining approach to estimate the *antenna weight vectors* (AWV) using spatial multiplexing, i.e., based upon codebook-based hybrid beamforming in LoS scenarios. Namely, the antenna arrays at the MS and BS are grouped into sections of subarrays with a predefined subarray separation, i.e., so that the resultant beam at each subarray points in a different spatial direction. Hence the scheme preforms initial coarse beamtraining in the inner-subarray followed by beam refinement, i.e., inter-subarray spatial multiplexing. In the former step, the best quasi omni-directional transmit and receive patterns are selected from a small set of pair-wise AWVs. Overall, results show that this subarray scheme significantly reduces beamtraining complexity and feedback overhead

versus *stochastic gradient algorithm* (SGA) blind beamforming beamtraining., i.e., 25% reduction. This solution can be also refined by using beamtraining selection based upon MIMO capacity at the inter-subarray spatial multiplexing level.

Meanwhile, the work in [43] presents a similar approach that iteratively refines beamforming vectors based upon maximum instantaneous channel capacity. Namely, this method searches for best codebook beams from a subset of the RF chains at a time, i.e., while keeping the other chain beams fixed. The chain returning the highest cumulative capacity is then chosen, and t procedure is repeated until convergence, i.e., highest chain pair-wise capacity.

Nevertheless, both of the above subarrays schemes impose restrictions on RF chain subset sizes at the MS and BS nodes. Hence overall search complexity is controlled by subset size, e.g., search complexity is linear for a single subset. Furthermore, pencil beam transmissions introduce further exponential complexity, i.e., power consumption overheads can become practically infeasible.

2.5.6 Auxiliary Transceiver Schemes

Auxiliary transceiver schemes assume that the MS nodes are quipped with a single array connected to two transceivers, i.e., hybrid auxiliary narrowband and digital wideband transceivers. This additional transceiver is purely digital and basically consists of narrowband RF chains (narrowband ADC and DAC). Note that the narrowband transceiver is used for initial access and control signaling purposes, i.e., other wideband hybrid transceiver is responsible for data transmission only. Although, both transceivers operate simultaneously using *frequency division multiple access* (FDMA) mode, the digital transceiver consumes most of the bandwidth here, i.e., since the auxiliary transceiver requires narrow/reduced bandwidth for control signaling purposes (small beacon overhead). Namely, the auxiliary transceiver performs beam scanning,

whereas the digital transceiver performs beamforming in the best direction. Now the initial access procedure here is composed of three stages including *downlink* (DL) cell detection, *uplink* (UL) access request, and access grant and resource allocation, see [44] for details

Meanwhile, the work in [45] develops another auxiliary scheme for a multi-BS access. Namely, all BS nodes here transmit beacon signals using orthogonal preambles generated by their auxiliary transceivers. Now when a MS node accesses the mmWave network, frame detection is done akin to the single BS case using all available preambles. The MS node then selects the best detected beacons based upon the received power level, and thereafter it decodes the highest beacon signal. In general, the MS ranks the highest power levels across all detected beacon signals, and alternative beacon signals are used in case of link degradation or blockage. The overall performance of this scheme is compared to a hybrid beamforming access scheme in terms of beacon overhead and duration. This latter scheme performs sequential rather than simultaneous beacon and data transmission. Results indicate much lower beacon overheads for 0.1 ms sub-frame lengths, i.e., close to the fully-digital scheme. Note that beacon overhead and duration also depend upon the bandwidth of the auxiliary transceiver, i.e., lower bandwidth can result in lower beacon overheads. Results also show that the duration of the auxiliary transceiver beacon exceeds its hybrid counterpart due to its narrowband specifications. Therefore, the associated beam acquisition delays are still relatively small (3-5 ms range) as compared to the hybrid case (8-10 ms range).

Finally, the work in [46] proposes a new beamforming architecture using hybrid wideband and auxiliary digital MIMO narrowband transceivers. This solution exploits the long beacon durations (narrow beacon bandwidth) associated with digital auxiliary transceiver to reduce beacon overhead and beam alignment delays. Additionally the narrowband ADC and

DAC at the auxiliary transceiver also yield lower quantization resolution, thereby reducing cost and complexity. However this approach consumes excessive power due to simultaneous operation of two transceivers and scanning operations across multiple parallel beams. In fact, these levels can even exceed the requirements for digital and analog beamformers combined.

2.5.7   Coordinated Triangulation Access Schemes

A coordinated triangulation technique for clustered *mmWave small cells* (mmSCs) is proposed in [47] to reduce access times. This method is best suited for ultra-dense LoS standalone networks without overlaid legacy networks. Namely, the mmSCs (or BSs) within each clustered coverage area perform initial access in a coordinated fashion using PDP measurements, i.e., the mmSCs are synchronized to start beam-scanning simultaneously. Meanwhile, the MS beam directions are randomly chosen in an exhaustive brute-force manner. The beam access procedure is then performed jointly between the entire mmSCs in the coverage cluster. Overall, the proposed access scheme is divided into several key phases, i.e., PDP measurement (Phase I), coordinated beam sweep reordering (Phase II), initial access (Phase III), and asymmetric multi-cell association (Phase IV). In Phase I, the initial beam directions are randomly selected by the mmSC nodes. Here, each mmSC calculates PDP values for each beam cycle duration to generate PDP peak reports. Note that the number of peaks is equal to the number of transmit beams at the MS, i.e., each corresponds to a single beam index. Overall, Phase I measures the PDP of the received preambles and shares this information with the other mmSCs in the cluster through LoS backhaul links. Next in Phase II, the mmSCs jointly order the power levels for the various spatial direction associated with the preambles. The best beam direction is then computed based upon the measurements reports. Meanwhile, the MS also conducts coarse beam scanning for a given beam-triplet until an uplink connection to the MS is

successfully established (Phase III). Namely, the mmSC is discovered if the PDP peaks are above a detection threshold based upon the target false alarm detection probability. Finally, in Phase IV the existing uplink connection is used to setup additional connections with the same or different mmSC for improved spectral efficiency.

Overall, a key limitation of coordinated triangulation scheme is position estimation accuracy, i.e., the MS location can only be approximated and the central direction of the MS beam may not be perfectly aligned with the direction of a single mmSC. Hence the chosen beams at the mmSCs may not point towards the actual MS location due to such estimation errors. Furthermore, estimation accuracy can only be improved by using more than three measurement reports at the expense of higher access times. Nevertheless, a key advantage of the proposed scheme is its reduced measurement reporting overheads, i.e., only a few bits are required to carry the index of the beam. Results confirm that this algorithm delivers fast access times without results overhead between mmWave and overlaid legacy networks.

Now carefully note that the coordinated triangulation scheme is only applicable in LoS scenarios between the mmSCs and the MS. Hence if the LoS link is blocked, the MS beam can potentially point to a reflector, i.e., forming a NLOS link. However this setup is contingent upon the scattering and reflection properties of the cannel obstacles. Also, the estimated MS position also differs from the actual location. As a result, none of the mmSCs can precisely adjust their transmit beam directions. Nevertheless, the robustness of the proposed algorithm is highly-dependent upon network deployment densification. Furthermore, this scheme is only practical in smaller dense networks, since three mmSCs are required to perform simultaneous preamble reception.

2.6   Open Challenges

Overall, beam access scheme remains a major challenge in mWwave networks. Despite the some existing proposals to minimize beam access overheads, many open challenges still remain here. Foremost there is a critical need to reduce beam access times to meet the tight control latency requirements for 5G systems. Namely, efficient and fast beam access schemes are needed to handle the sparse nature of mmWave channels. Furthermore, these solutions must present feasible beamforming architectures, i.e., in terms of power consumption, energy efficiency and channel rank. Also, these access schemes must incorporate a range of channel models for LoS and NLoS environments, such as Rayleigh and Rician path gains. Finally, there is also a further need to develop reliable link recovery schemes subsequent to the initial beam access stage, i.e., that incorporate channel blockage models. Accordingly, these various challenges form the main motivating factors for this dissertation research.

Chapter 3

Initial Beam Access Schemes: Efficient Search Solutions

As noted in Chapter 2, existing initial beam access methods suffer from high computational complexity and prolonged access times (latencies). Hence fast and power efficient schemes are necessary for highly-directional beamforming architectures in mmWave networks.

In light of the above, this chapter presents rapid access schemes based upon gradient-free heuristics. First, the access problem is formulated as a search model composed of a search grid (angular domain) and beam indices. Direct pattern search procedures are then developed for LoS and NLoS propagation environments. These procedures are inspired by the Nelder Mead (NM), Luus Jaakola (LJ), divide-and-conquer (DC), Tabu search (TS), coordinated generalized pattern search (CGPS), and Hooke Jeeves (HJ) search methods. Namely, instead of testing all possible beamforming combinations, these procedures are designed to only evaluate a limited number of beamforming and combining vectors to estimate the best direction with reduced computational complexity. The performance evaluation of these solutions is then analyzed in details compared to some existing methods in terms of computational complexity, access times, power and energy consumption, and success rates. See Figure 3.1 for the overall structure of this chapter.

First, the system framework is presented to introduce a multi-resolution hierarchical codebook and array model for the beamformer, along with the signal and channel models. The beam access problem formulation is presented next, followed by the access procedures and performance evaluation.
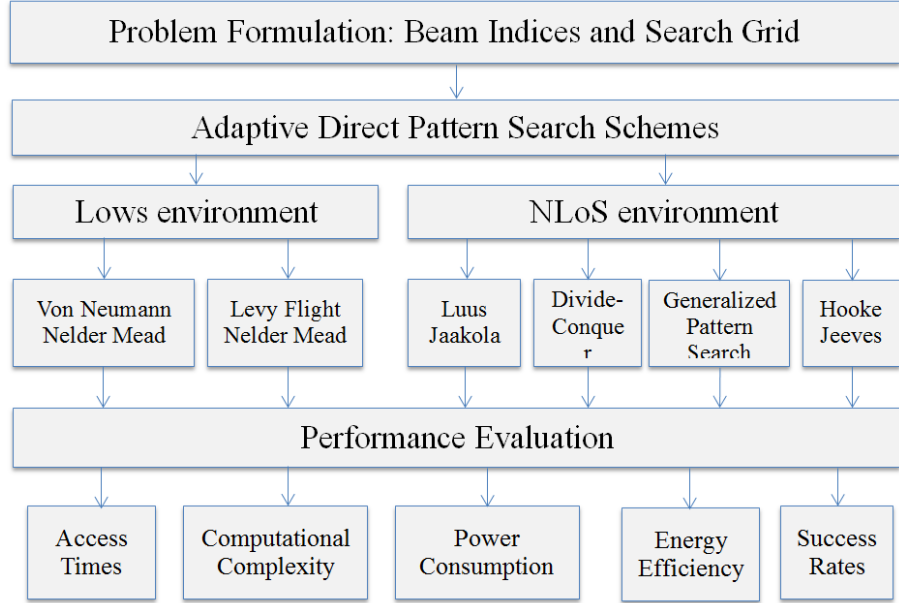
Figure 3.1: Adaptive pattern search schemes for LoS and NLoS environments

3.1 System Framework

In general, digital beamforming techniques can enhance spatial multiplexing and high spectral efficiencies. However, these gains come at the detriment of high power consumption as discussed in Chapter 2. Hence analog beamforming solutions are proposed for BS and MS access. Namely, these methods can provide reduced power consumption in MS front-ends and are suitable for the low-rank mmWave channels, i.e., sparse analog precoding matrix. Along these lines, corresponding codebook structure and array model is presented for the analog beamformer. The requisite signal and the sparse channel models are also detailed, i.e., for subsequent use in the proposed beam access solution. Note that beamforming design is only presented for the MS (solution at the BS can be defined similarly).

3.1.1 Codebook Structure

The overall system model assumes that the BS and MS nodes are both equipped with a multi-resolution cascaded codebook, i.e., for beam reciprocity between the downlink and uplink directions. Furthermore, each codeword specifies a predefined beam steering weight to drive

40

discrete phase shifters. Namely, this codebook consists of $y = 1, 2, \ldots, Y$ stages, where each stage defines $b = 1, 2, \ldots, B$ wide beams $\in [0, 2\pi]$ generated by N_{MS}^y antennas at each codebook stage y, $Y \neq B$, where $B = 2\pi/\phi_0^{MS}\big|_{y=1}$ and ϕ_0^{MS} is the beamwidth for the observation angle at the MS, i.e., at broadside or endfire directions $\{\phi_0^{MS}: \phi_{brd}^{MS}, \phi_{endfire}^{MS}\}$. Each beam vector in b is also divided into $\check{b}$ narrow beams for $y > 1$, where $\check{b} = 1, 2, \ldots, B$ ($\check{b} \subseteq B$, $\phi_{\check{b}} \subseteq \phi_b$) for a total of $B_T^y = 4^y$ beams in each stage. For example, Figure 3.2(a)-(c) illustrates a sample codebook design for $Y = 3$ stages. Here the initial stage performs beam search using wider beams to capture higher power intensity at the expense of lower gains. The beam with the highest detected power is then selected for further refinements in the latter stages.

(a) Codebook Stage I

(b) Codebook Stage II

(c) Codebook Stage III

Figure 3.2: Cascaded codebook with $Y = 3$ stages and $B = 4$ beams

3.1.2 Array Model

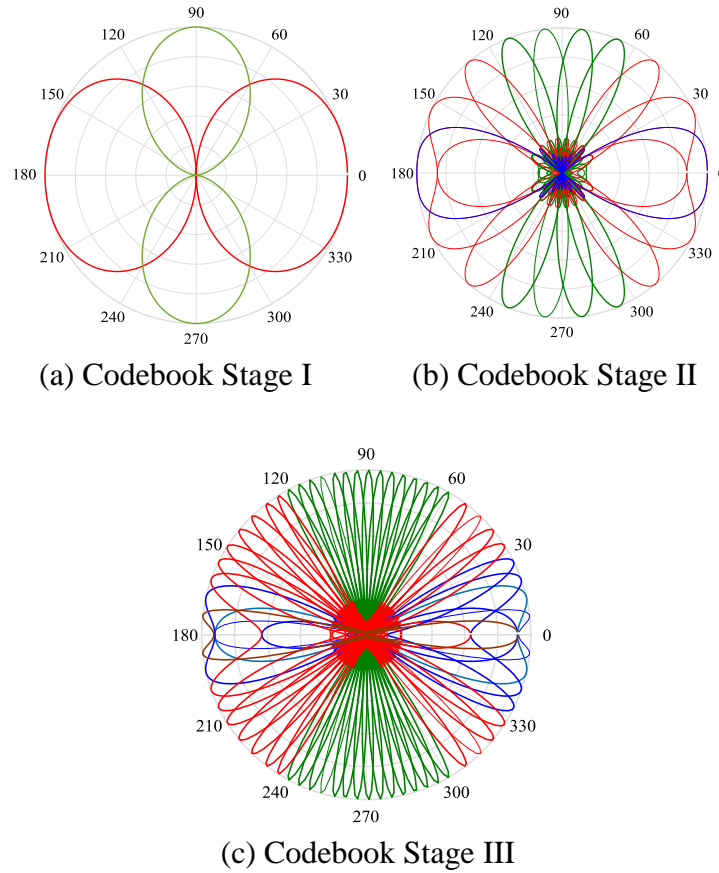Now consider a BS and MS pair equipped with N_{BS}^{T} and N_{MS}^{T} co-polarized antenna elements, respectively, where $N_{MS}^{T}=2\sum_{y=1}^{Y}N_{MS}^{y}$, $N_{BS}^{T}=2\sum_{y=1}^{Y}N_{BS}^{y}$. Here the ABF design is constructed using a single RF chain with back-to-back *uniform amplitude linear arrays* (ULA) having uniform inter-element spacing $d_n = \lambda/2$, where λ is the wavelength. Now in order to avoid grating lobes and pattern blindness, the antenna elements displacements must be small enough such that $d_n < 1+\left|\cos\theta_0^{MS}\right|$, where θ_0^{MS} is the observation angle at the MS. Based upon the above setup, the closed-form normalized array response vector at the MS, A_{MS}, is given by the periodic array factor. Specifically, this response at azimuth scanning directions in stage y is given by [48]:

$$A_{MS} = \frac{1}{N_{MS}^{y}}\sum_{n=1}^{N_{MS}^{y}}a_n\exp(j(N_{MS}^{y}-1)(k_v d_n \cos\theta_0^{MS} + \beta_{MS}), \tag{3.1}$$

where a_n is the n-th element amplitude excitation, $k_v = 2\pi/\lambda$ is the wave number, and β_{MS} is the incremental progressive phase shift between the antenna elements at the MS. Also, $\varphi_{MS}= k_v d_n \cos\theta_0^{MS} + \beta_{MS}$ is the array phase function at the MS with a visible region varying between $-k_v d_n \leq \varphi_{MS} \leq k_v d_n$. Furthermore, the array beamwidth in the broadside and scanning directions $\forall\theta_0^{MS}\left(\theta_0^{MS}: 0 < \theta_0^{MS} \leq \pi\right)$ for each stage is [49]:

$$\phi_{brd}^{MS} = \cos^{-1}\left(\frac{\lambda}{2\pi d_n}k_v d_n\cos\theta_0^{MS} \pm \frac{2.782}{N_{MS}^{y}}\right), \quad 0 < \theta_0^{MS} \leq \pi, \tag{3.2}$$

Finally, the beamwidth at codebook stage y in the end-fire direction is given by:

$$\phi_{endfire}^{MS} = 2\cos^{-1}(1-1.391\lambda/N_{MS}^{y}d_n), \textit{ for } \theta_0^{MS} = 0, \pi. \tag{3.3}$$

Overall, the spatial footprint of the array increases proportionally to a broadening factor σ_b, where $\sigma_b = 1/\cos\theta_0^{MS}$ for directions scanned off the broadside [49]. Also, the array gain is given by $G_{A_{MS}}= A_{MS}G_a$, where G_a is the gain for a single element. In particular, a gain of 3-5 dBi

is reasonable for a microstrip rectangular patch antenna design of the commonly used in mmWave applications [50].

3.1.3 Signal and Channel Models

In general, mmWave systems are best-suited for low mobility outdoor pedestrian environments. Hence considering a single stationary MS in LoS, the received single carrier waveform for the downlink is given by:

$$y_l = u_l^{\mathrm{H}}(\theta_0^{\mathrm{MS}}) \mathrm{H}_{\mathrm{LoS}} v_l(\theta_0^{\mathrm{BS}}) z + w_l, \qquad (3.4)$$

where $(.)^{\mathrm{H}}$, $u_l(\theta_0^{\mathrm{MS}})$ and $v_l(\theta_0^{\mathrm{BS}})$ are the Hermitian operation, beamforming and combining vectors for the l-th channel path, respectively, i.e., $\|u_l^2\| = N_{\mathrm{MS}}^y$, $\|v_l^2\| = N_{\mathrm{BS}}^y$. The observation angles here (θ_0^{MS} and θ_0^{BS}) also represent the angles of arrival and departure at the MS and BS, respectively. Note that $u_l = A_{\mathrm{MS}}^{\mathrm{T}}$ and $v_l = A_{\mathrm{BS}}^{\mathrm{T}}$ due to the absence of a baseband precoding stage in analog beamformer, where $(.)^{\mathrm{T}}$ represents the transpose operation. Therefore the channel gain, $\mathrm{H}_{\mathrm{LoS}}$, for LoS environment is defined as:

$$\mathrm{H}_{\mathrm{LoS}} = h_{\mathrm{LoS}} u_l v_l^{\mathrm{H}}, \qquad (3.5)$$

where h_{LoS} is the small-scale fading coefficient (rank one) for the LoS path. Furthermore, z in Eq. (3.4) is the control signal carrying the primary and secondary synchronization signals (PSS, SSS) in which the cell number is modulated using the Zadoff Chu sequence, where P_{tr} is the transmit power constraint. The *additive white Gaussian noise* (AWGN) component is also given by $w_l \sim N(\partial, \sigma^2)$, with mean ∂ and variance σ^2. Meanwhile for NLoS channels, the complex channel gain, $\mathrm{H}_{\mathrm{NLoS}}$, is defined using the geometry-based stochastic channel model [41]:

$$\mathrm{H}_{\mathrm{NLoS}} = \sqrt{\frac{N_{\mathrm{MS}}^{\mathrm{T}} N_{\mathrm{BS}}^{\mathrm{T}}}{P_l}} \sum_{s=1}^{S} \sum_{l=1}^{L} h_{\mathrm{NLoS}} u_l(\theta_0^{\mathrm{MS}}) v_l^{\mathrm{H}}(\theta_0^{\mathrm{BS}}), \qquad (3.6)$$

where P_l is the path loss between the BS and MS, h_{NLoS} is the complex gain of the NLoS path for L total number of rays (paths) arriving in S clusters (spatial lobes). The channel is also S-sparse here, i.e., S is the number of non-zero elements in the channel matrix (total number of resolvable clusters). Note that the choice of a geometric channel model here is mainly driven by the BRCS properties of obstacles and the reduced energy levels captured via beamforming. Overall, this selection results in a low-rank angular sparse channel with low density impulse response (IR). Meanwhile, the path loss (P_l) is given by the floating intercept model using least square fit [51] for outdoor environments, expressed by:

$$P_l[\text{dB}] = \alpha_{fl} + \rho_{sl}10\log_{10}(r) + \xi_{sf}, \tag{3.7}$$

where α_{fl} is the floating intercept in dB, ρ_{sl} is the intercept slope, and ξ_{sf} represents shadow fading, i.e., $\xi_{sf} \sim logN(0, \sigma_s)$ with 0 dB mean and σ_s standard deviation. Alternatively, the path loss model can also be based upon the reference model defined in [52] for outdoor settings, i.e.:

$$P_l = 20\log_{10}(4\pi r_0/\lambda) + 10\eta\log_{10}(\frac{r}{r_0}), \tag{3.8}$$

where η, r and r_0 represent the PLE, the BS and MS separation and reference distances, respectively. These two path loss models are adopted in this chapter, where approximate path loss levels are achieved.

3.2 Beam Access Problem Formulation

The initial mmWave access problem is now modeled. Foremost, let the beamforming and combining vectors for the l-th path (u_l, v_l) be denoted by the r_i and s_j beam indices, respectively, where $i, j = 1, 2,..., B$, and $r_i = \forall u_l(\theta_0^{\text{MS}}) \in [0, 2\pi]$ and $s_j = \forall v_l(\theta_0^{\text{BS}}) \in [0, 2\pi]$. Namely, these vectors span the overall spatial domain using the proposed multi-stage codebook in Section 3.1.1. Hence the η-dimensional search grid is given by $\hat{G} = \{\forall(r_i, s_j)\}$, where $\hat{G} \in \mathbb{R}^\eta$ represents an angular space

44

of $[0, 2\pi]$ with P_k points, $k=1,2,...$, ij, and P_k is a beam index pair (r_i, s_j). This grid corresponds to all possible azimuth combination for the beam directions at the BS and MS.

Based on the above, the overall objective function is defined using the received signal power level at point P_k at the MS after the combining vector stage (or at the BS after the beamforming vector), i.e., $y_l(P_k(r_i, s_j))$. The overall goal of the mmWave access scheme here is to find the best pair that maximizes the signal level (objective function) in LoS and NLoS settings, given by:

$$(r_i, s_j)_{bst_y} = max\{y_l(P_k(r_i, s_j)) | P_k \subset \hat{G}\}, \text{ s.t. } i, j, \in[1, B]. \tag{3.9}$$

Figure 3.3 shows an example of the received signal profile at codebook stage $y=1$ ($B=4$) in a LoS environment at a distance separation (r) of 200 m and scalar channel gain, i.e., $h_{LoS}=1$ (see Table 3.1 for other parameter settings). Hence, the goal here is to detect the single best index pair that gives the highest signal level of -47 dBm.
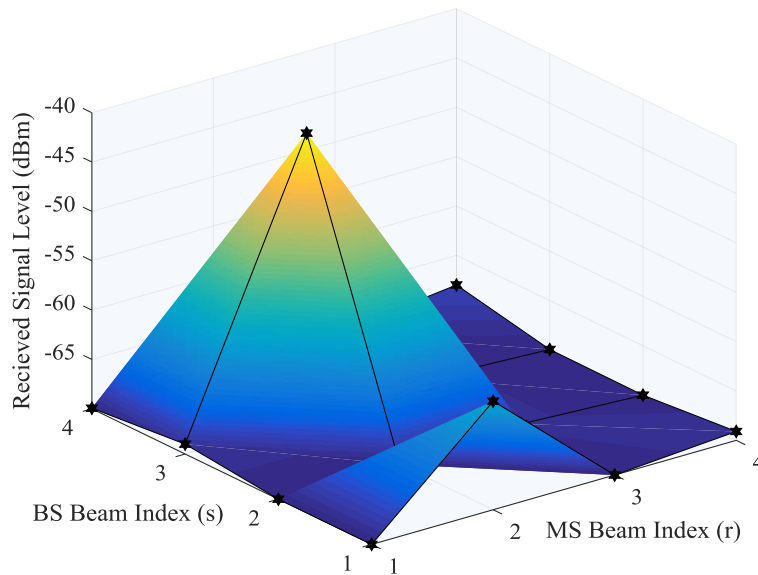

Figure 3.3: Received signal profile in LoS for codebook Stage I ($y=1$, $B=4$)

Note that Figure 3.3 also shows a local maximum corresponding to a low received signal level attributed to the detection of the undesired *side lobe levels* (SLL), i.e., when the BS and MS main

beams are not perfectly aligned (e.g., -63 dBm). The sparse structure of the received signal levels in the NLoS case is also evident here in Figure 3.4.
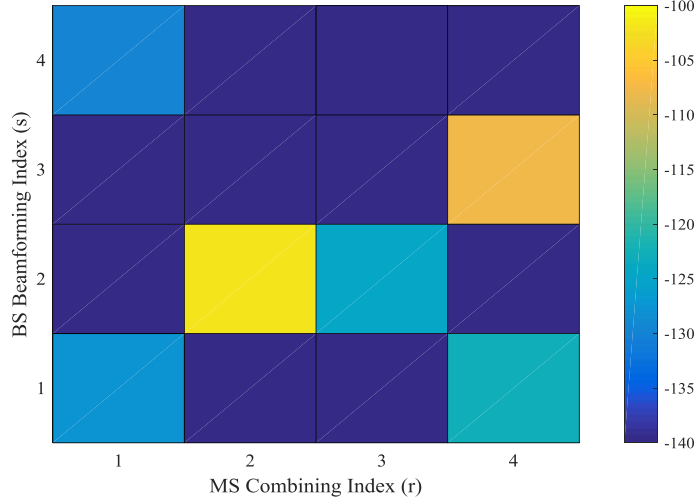
Figure 3.4: Received signal profile in NLoS for codebook Stage I (y =1, B=4)

Table 3.1: System settings for the proposed Nelder Mead schemes

Category	Parameters	Value
System	f_c (GHz), BW (MHz), y_{th} (dBm)	28, 100, -55
Channel	η, h_{LoS}, ∂, σ^2, r (m), r_0 (m)	2, 1, 0, 1, 1, 50
ULA	P_{tx}(dBm), G_a, $N_{MS,BS}^{S1}$, $N_{MS,BS}^{S2}$, $N_{MS,BS}^{S3}$, a_n	35, 5, 2, 6, 19, 1
Codebook	Y, B, B_T^1, B_T^2, B_T^3	2, 4, 4, 16, 64
NM schemes	Γ, δ, ζ_r, n_r, μ, ρ_c, d_c	2, 2, 1, 1, 2, 0.5, 1
Power (mW)	P_{ADC}, P_{BB}, P_M, P_{LO}, P_{LPF}, P_{AMP}, P_{LNA}, P_{PS}^{S1}, P_{PS}^{S2}, P_{PS}^{S3}	20, 20, 19, 5, 14, 5, 20, 10, 45, 78
PSS time	t_{PSS} (μs)	200

It is clear that the objective function in the NLoS case consists of few dominant and resolvable clusters, i.e., a single global maximum (e.g., -102 dBm) corresponding to a unique (r_i, s_j) pair, and a local maximum (e.g., -110 dBm) resulting from undesired SLL similar to the LoS case. Consider here the memoryless probability for the direct pattern search schemes

detecting the highest received signal at $P_k(r_i, s_j)$, i.e., $\acute{y}_l((r_i, s_j)_{bst_y})$, after $\acute{t}$ trials, $\acute{t} = 1, 2, ..., \acute{T}$. Namely, this value is given by:

$$\mathbb{P}\left[\acute{y}_l\left(P_k(r_i, s_j)\right)_{bst_y}\right] = \begin{cases} \dfrac{1}{B^2}, \; for \; k = 1, \\[4mm] \dfrac{1}{B^2 - (k-1)} \displaystyle\prod_{\acute{t}=1}^{\acute{T} = k-1} \dfrac{B^2 - \acute{t}}{B^2 - (\acute{t}-1)}, for \; k \geq 2. \end{cases} \tag{3.10}$$

Additionally, the conditional probability of an event $\check{C}$ successfully detecting the highest signal at $P_k(r_i, s_j)$ after $\acute{t}$ trials given F previous failures is:

$$\mathbb{P}\left(\check{C}\,\middle|\,F\right) = \frac{\mathbb{P}(\check{C} \cap F)}{\mathbb{P}(F)} = \frac{\mathbb{P}(\check{C})\mathbb{P}(F)}{\mathbb{P}(F)} = \frac{1}{B^2 - (\acute{t}-1)}, \; \acute{t} = 1, 2.., k. \tag{3.11}$$

In light of the above, nonlinear search methods for LoS and NLoS are now presented to solve the aforementioned objective function with least possible number of measurements.

3.3 Efficient Search Schemes for LoS Environments

The search schemes proposed here try to solve Eq.(3.9) with a reduced number of measurements. In particular, the proposed beamforming solutions for (single-rank) LoS settings use an enhanced version of the downhill simplex method. Consider the details.

The Nelder Mead (NM) search method is shown in Figure 3.5. This meta-heuristic can be used to find a global maximum for a smooth unimodal function within a few steps. Multiple key variables are further proposed here in efforts to achieve acceptable convergence rates for the NM method, i.e., based upon Von Neumann and Chebyshev distances search, and Levy Flight random walk.

Now the traditional NM method starts by constructing a simplex of $\Delta = \Gamma_{NM} + 1$ vertices $\in \mathbb{R}^2$, where Γ_{NM} is the number of variables in the NM scheme that identify the beamforming and combining vectors (beam indices). Namely, each vertex here represents a beam pair that will

be tested to maximize the objective function. The scheme then adapts the shape and location of the simplex based upon the outcomes of the objective function until a maximum is found at which time the search prodecure terminates.

Now three points are used to form the initial simplex here, i.e., denoted by $P_1(r_1, s_1)$, $P_2(r_2, s_2)$ and $P_3(r_3, s_3)$. Although this set can be randomly selected anywhere in the search space, it is generally favorable to start from the edges to test different regions in ascending or descending order (and thereby strengthen the convergence behaviors). Note that the boundaries of the search space are also confined by the predefined set of MS and BS codebooks. Additionally, the dimension of the simplex is governed by the step size, δ, away from P_1. Hence in order to accelerate the search process and avoid exceeding the lower and upper bounds of the beam sequences, the step size is critically chosen as $\delta = B/2$. After the simplex is constructed, the search procedure runs the key steps of the modified NM scheme:

1) Ranking

The objective function is first evaluated at the three vertices: $y_l'(P_1(r_i, s_j))$, $y_l'(P_2(r_i, s_j))$, and $y_l'(P_3(r_i, s_j))$. The results are then sorted, as best (P_B), intermediate or good (P_G), and worst (P_W) [53] according to the detected signal levels, i.e., worst corresponds to the lowest value of the objective function across all three vertices, i.e.:

$$P_W = P_1(r_i, s_j),\ P_G = P_2(r_{i+\delta}, s_{j+\delta}),\ \text{and}\ P_B = P_3(r_i, s_{j+\delta}). \tag{3.12}$$

Carefully note if all vertices deliver equal signal levels, then the ranking is based upon the location of the vertex, with the worst vertex corresponding to the lowest subscript order. This choice migrates the search away from poor regions when the objective function may be equal at all vertices.

2) Reflection

This step formulates and examines a new point that is distantly located from P_W and in the proximity of P_G and P_B, i.e., to reinforce the prediction of the best pair location. In particular, this "reflected" point is calculated as per [54]:

$$P_R = (1 + \zeta_r)\overline{P}_c - \zeta_r P_W, \ \zeta_r \in \mathbb{R} \mid \zeta_r > 0, \tag{3.13}$$

where $\overline{P}_c$ is the centroid of the line joining P_G and P_B given by $\overline{P}_c = (P_B + P_G)/2$, and ζ_r is the reflection coefficient away from P_W. Note that if $y_l(P_R) > y_l(P_W)$, then P_W is replaced with P_R to formulate a new simplex.

3) Von Neumann and Chebyshev Distances Search

This step amends the traditional NM method to achieve more accurate convergence towards the highest signal level. Namely the objective function is now computed in a *Von Neumann* (VN) squared lattice neighborhood of the (above-computed) reflected points, $P_{R1, R2}^{vn}(r_i, s_{j\mp n_r})$ and $P_{R3, R4}^{vn}(r_{i\mp n_r}, s_j)$, where $n_r = \delta/2 \in [1, B]$ is the Von Neumann neighborhood range. A single reflection point is then selected after which expansion is performed. This approach avoids formulating unnecessary redundant triangles in case all initial vertices are equal. Hence the Von Neumann distance satisfies:

$$N_{(r_i, s_j)}^v = \{(r, s): |r - r_i| + |s - s_j| \leq n_r\}. \tag{3.14}$$

To further increase the robustness of the search procedure, the Chebyshev distance, d_c, is also considered here, i.e., to improve performance at the expense of increased computational complexity. Namely, this latter value is calculated at the refection point as: $P_{R1, R2}^{cv}(r_{i\mp d_c}, s_j)$, $P_{R3, R4}^{cv}(r_i, s_{j\mp d_c})$, $P_{R5, R6}^{cv}(r_{i\mp d_c}, s_{j+d_c})$, and $P_{R7, R8}^{cv}(r_{i+d_c}, s_{j\mp d_c})$, where $d_c = \delta/2 \in [1, B]$.

4) Expansion

In case the Von Neumann or Chebyshev reflection schemes give a new local maximum, the search grid can be expanded to point P_E, defined as $P_E = \mu P_R + (1-\mu)\overline{P}_c$, where μ is the expansion coefficient, $\mu > 1$. However, if both reflection and expansion cannot extract the maximum, then subsequent contraction and shrinkage operations are performed jointly.

5) Contraction

If the objective function at the reflected point $\acute{y}_l(P_R)$ is equal to the worst point $\acute{y}_l(P_W)$, i.e., $\acute{y}_l(P_R) = \acute{y}_l(P_W)$, then additional beam pairs must be tested. Now the maximum is expected to fall within the interior of the simplex rather than along the outer grid region. Hence two mid-points $P_{C1, C2}$ are symmetrically constructed around the line segments P_W-P_M and P_M-P_R, respectively, expressed by $P_{C1, C2} = \rho_c P_W \mp (1-\rho_c)\overline{P}_C$, where ρ_c is the contraction coefficient $\in (0, 1]$. The point that returns $max\,(\acute{y}_l(r_i, s_j))$ is denoted as P_C, and the new simplex is given by P_B-P_G-P_C.

6) Shrinkage

Now if the objective function at the contraction point $\acute{y}_l(P_C)$ is less to that at the worst point $\acute{y}_l(P_W)$, i.e., $\acute{y}_l(P_C) < \acute{y}_l(P_W)$, then P_G and P_W are shrunk toward P_B by replacing them with $P_M = (P_G + P_B)/2$, and $P_S = (P_W + P_B)/2$, respectively.

Overall, the NM scheme terminates when a new simplex has been formed after the expansion or shrinkage steps and a sufficient signal level has been detected, i.e., to exceed the receiver threshold, $\acute{y}_l((r_i, s_j)) \gg \acute{y}_{th}$.

Inputs: *Y*, *B*, Γ, δ, n_r, ζ_r, μ, ρ_c

For $y \geq 1$, $y \leq Y$, $\forall (r_i, s_j) \in [1, B]$ *// Start Nelder Mead search with codebook Stage I*

  $P_\Delta(r_i, s_j)$: $P_1(r_i, s_j)$, $P_2(r_{i+\delta}, s_j)$, $P_3(r_i, s_{j+\delta})$, i, j = 1, 2, …, B *// Construct initial simplex*

  $\acute{y}_l(\forall P_\Delta(r_i, s_j))$ *// Measure signal level at the initial simplex*

  Rank: P_B, P_G, P_W *// Rank the simplex vertices as best, good and worst*

  Reflection: $P_R = (1+\zeta_r)\bar{P}_c - \zeta_r P_W$ *// Reflection point*

  Von Neumann Search: $P_R^{vn}(r_i, s_j) = P_{R1, R2}^{vn}(r_i, s_{j \mp n_r})$, $P_{R3, R4}^{vn}(r_{i \mp n_r}, s_j)$ *// Von Neumann (VN) Reflection points*

  max $\acute{y}_l(P_R^{vn}(r_i, s_j))$, $P_R \leftarrow P_R^{vn}$ *// Measure signal at the VN points, select the best point as the new refection point*

  Chebyshev Search: $P_{R1, R2}^{cv}(r_{i \mp d_c}, s_j)$, $P_{R3, R4}^{cv}(r_i, s_{j \mp d_c})$, $P_{R5, R6}^{cv}(r_{i \mp d_c}, s_{j+d_c})$, and $P_{R7, R8}^{cv}(r_{i+d_c}, s_{j \mp d_c})$

  max $\acute{y}_l(P_R^{cv}(r_i, s_j))$, $P_R \leftarrow P_R^{cv}$ *// Measure signal at the Chebyshev points and select the best reflection point*

    If $\acute{y}_l(P_R) > \acute{y}_l(P_G)$

        If $\acute{y}_l(P_R) < \acute{y}_l(P_B)$, $P_W \leftarrow P_R$

           Else $P_E(r_i, s_j) = \mu P_R + (1-\mu)\bar{P}_c$, $\mu = \delta$ *// Expansion point*

               $\acute{y}_l(P_E)$ *// Measure signal a the expansion point*

               If $\acute{y}_l(P_E) > \acute{y}_l(P_R)$, $(r_i, s_j)_{bst_y} \leftarrow P_E$, $y \leftarrow y+1$ *// Expansion point is the best beam indices pair*

                  Else $(r_i, s_j)_{bst_y} \leftarrow P_R$, $y \leftarrow y+1$ *// Reflection point is the best beam indices pair*

             End if

          End if

      Else *// $P_R < P_G < P_B$*

        If $\acute{y}_l(P_R) > \acute{y}_l(P_W)$, $P_W \leftarrow P_R$

           $P_{C1, C2} = \rho_c P_W \mp (1-\rho_c)\bar{P}_c$ *// Contraction*

           $P_c \leftarrow$ *max* $\acute{y}_l\{P_{C1}, P_{C2}\}$ *// Calculate best contraction point*

          If $\acute{y}_l(P_C) > \acute{y}_l(P_W)$, $P_W \leftarrow P_C$ *// New simplex is constructed*

             $(r_i, s_j)_{bst_y} \leftarrow$ *max max* $\acute{y}_l\{P_\Delta(r_i, s_j)\}$, $y \leftarrow y+1$

          Else $P_S = (P_B + P_W)/2$, $P_M = (P_B + P_G)/2$ *// Shrinkage*

              $\acute{y}_l(P_S)$, $\acute{y}_l(P_M)$, $P_S \leftarrow P_W$ & $P_M \leftarrow P_G$

              $P_\Delta(r_i, s_j) \leftarrow P_B - P_M - P_S$ *// New simplex is constructed*

              $(r_i, s_j)_{bst_y} \leftarrow$ *max* $\acute{y}_l\{P_B, P_M, P_S\}$, $y \leftarrow y+1$ *// Measure signal at the new simplex*

        End if

        Else *// Do contraction and shrinkage for ΔWGB*

             $(r_i, s_j)_{bst_y} \leftarrow$ *max* $\acute{y}_l\{P_B, P_M, P_S\}$, $y \leftarrow y+1$

        End if

      End if

  End if

End for

Figure 3.5: Von Neumann and Chebyshev Nelder Mead initial beam access schemes

A further modified scheme is also presented to improve search success rates and reduce computational complexity, as detailed in Figure 3.6. Specifically, this approach uses an access

Inputs: δ, *Y*, *B*

For $y \geq 1$, $y \leq Y$, $\forall (r_i, s_j) \in [1, B]$ // *Start Levy Flight NM scheme with Codebook Stage I*

  Δ_1: $P_1 \leftarrow (r_{i_{min}}, s_{j_{min}})$, $P_2 \leftarrow (r_{i_{min+\delta}}, s_{j_{min}})$, $P_3 \leftarrow (r_{i_{min}}, s_{j_{min+\delta}})$ // *Construct first simplex*

  $y_l(\Delta_1)$: $y_l(P_1)$, $y_l(P_2)$, $y_l(P_3)$, $P_{B1} \leftarrow max\ y_l(\Delta_1)$ // *Measure signal at first simplex and choose best point* P_{B1}

  Δ_2: $P_4 \leftarrow (r_{i_{max}}, s_{j_{max}})$, $P_5 \leftarrow (r_{i_{max-\delta}}, s_{j_{max}})$, $P_6 \leftarrow (r_{i_{max}}, s_{j_{max-\delta}})$ // *Construct second simplex*

  $y_l(\Delta_2)$: $y_l(P_4)$, $y_l(P_5)$, $y_l(P_6)$, $P_{B2} \leftarrow max\ y_l(\Delta_2)$ // *Measure signal l at second simplex and choose best point* P_{B2}

  If $y_l(P_{B2}) > y_l(P_{B1})$ // *If the highest signal level exists in the best point* P_{B2} *of the second simplex*

     If $P_5 = P_{B2}$, $\bar{\bar{P}}_4 \leftarrow (r_{i_{max-\delta/2}}, s_{j_{max}})$, $\bar{P}_5 \leftarrow (r_{i_{min}}, s_{j_{max}})$ // *Explore the vicinity of* P_5

        $P_8 \leftarrow (r_{i_{max-\delta}}, s_{j_{max-\delta/2}})$, $y_l(\bar{\bar{P}}_4)$, $y_l(\bar{P}_5)$, $y_l(P_8)$

        $(r_i, s_j)_{bst_y} \leftarrow max\ y_l$, $y \leftarrow y + 1$ // *Select the point that maximizes the received signal level*

     Else if $P_{\Delta 2B}$, $\bar{P}_6 \leftarrow (r_{i_{max}}, s_{j_{min}})$, // *If the highest signal exists in the best point* P_{B1} *of the first simplex*

         $P_9 \leftarrow (r_{i_{max-\delta/2}}, s_{j_{max-\delta}})$ // *Construct additional points in the vicinity of* P_{B1}

         $y_l(\bar{P}_6)$, $y_l(P_9)$ // *Measure the signal level at these new points*

         $(r_i, s_j)_{bst_y} \leftarrow max\ y_l\{P_{\Delta 2B}, \bar{P}_6, P_9\}$, $y \leftarrow y + 1$ *select the point that maximizes the received signal*

     Else if $P_4 = P_{B2}$, $\bar{P}_4 \leftarrow (r_{i_{max}}, s_{j_{max-\delta/2}})$, $y_l(\bar{P}_4)$, $y_l(\bar{\bar{P}}_4)$ // *Explore the vicinity of* P_4

         $(r_i, s_j)_{bst_y} \leftarrow max\ y_l\{P_4, \bar{P}_4, \bar{\bar{P}}_4\}$, $y \leftarrow y + 1$

     Else $P_7 \leftarrow (r_{i_{max-\delta/2}}, s_{j_{max-\delta/2}})$, $P_9 \leftarrow (r_{i_{max-\delta/2}}, s_{j_{max-\delta}})$ // *Explore the vicinity of* P_7

         $y_l(P_7)$, $y_l(P_8)$, $y_l(P_9)$, $(r_i, s_j)_{bst_y} \leftarrow max\ y_l\{P_7, P_8, P_9\}$, $y \leftarrow y + 1$

    End if

  Else if $y_l(P_{B2}) < y_l(P_{B1})$ // *If the highest signal level exists in the best point* P_{B1} *of the first simplex*

     If $P_1 = P_{B1}$, $\bar{P}_1 \leftarrow (r_{i_{min+\delta/2}}, s_{j_{min}})$, $\bar{\bar{P}}_1 \leftarrow (r_{i_{min}}, s_{j_{min+\delta/2}})$ // *Explore the vicinity of* P_1

        $P_{11} \leftarrow (r_{i_{min+\delta/2}}, s_{j_{min+\delta/2}})$, $y_l(\bar{P}_1)$, $y_l(\bar{\bar{P}}_1)$, $y_l(P_{11})$, $(r_i, s_j)_{bst_y} \leftarrow max\ y_l\{\bar{P}_1, \bar{\bar{P}}_1, P_{11}\}$, $y \leftarrow y + 1$

     Else if $P_2 = P_{B1}$, $y_l(\bar{P}_1)$, $y_l(\bar{P}_6)$, $y_l(P_9)$ // *Explore the vicinity of* P_2

        $(r_i, s_j)_{bst_y} \leftarrow max\ y_l\{\bar{P}_1, \bar{P}_6, P_9\}$, $y \leftarrow y + 1$

     Else if $P_3 = P_{B1}$, $(r_i, s_j)_{bst_y} \leftarrow max\ y_l\{\bar{\bar{P}}_4, \bar{P}_5, P_8\}$, $y \leftarrow y + 1$ // *Explore the vicinity of* P_3

     Else $y_l(P_7)$, $y_l(P_8)$, $y_l(P_{11})$, $(r_i, s_j)_{bst_y} \leftarrow max\ y_l\{P_7, P_8, P_{11}\}$, $y \leftarrow y + 1$

    End if

  Else   // *Do contraction and shrinkage for the first and second simplexes*

  End if

End for

Figure 3.6: Levy Flight Nelder Mead initial beam access schemes

technique that is implicitly derived from the Levy Flight random walk, i.e., step-lengths feature heavy-tailed probability distribution. Hence two oppositely-located simplexes are formed in the search space $(r_i, s_j) \in [1, B]$, i.e., Δ_1 and Δ_2. For example, one can migrate from one

edge of the search grid to the opposite (diagonal) side to form the second counterpart simplex, i.e., while keeping the same step size δ and simplex dimensions. Hence the locations of the two simplexes are inherently analogous to a Levy Flight random walk. The objective function is then evaluated at all vertices of Δ_1 and Δ_2 and the simplex with the highest value of the objective function is chosen for the next stage. Subsequently, a global maximum search is carried out in the vertex neighborhood of this simplex. Now if the objective function is equal at all six vertices (very unlikely), then any single simplex can be chosen and contraction and shrinkage procedures executed (as detailed previously). For instance, when all vertices are equal at Δ_1, then the points P_1, $\overline{P}_1$, P_2, P_3, $\overline{P}_5$, P_9 and P_{11} are tested. Alternatively, the points P_4, $\overline{P}_4$, P_5, P_7, P_6, $\overline{P}_6$ and P_8 are tested if all vertices are equal at Δ_2. Now the overall schematic sequences for the proposed Von Neumann and Levy Flight Nelder Mead schemes are shown in Figure 3.7(a)-(b), respectively.

(a) Von Neumann Nelder Mead access   (b) Levy Flight Nelder Mead access
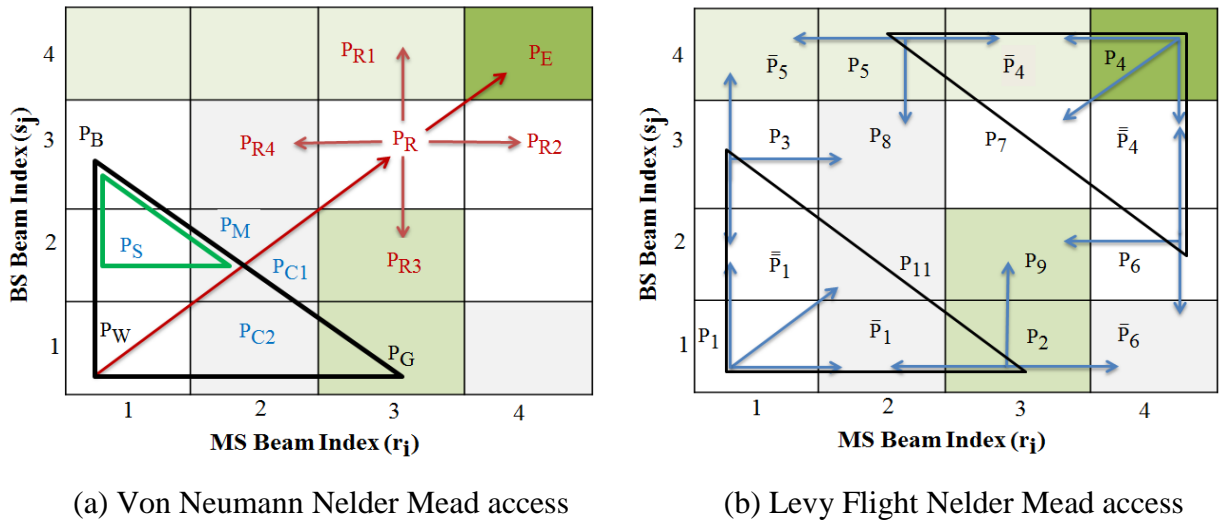
Figure 3.7: Nelder Mead procedures for initial beam access

Overall, the key advantage of the Levy Flight NM scheme is that it tests adjacent beam pairs located at two azimuthally-opposite directions separated by the maximum progressive phase shift, β_{max}. This strategy can help accelerate the detection process versus sequential regional pair testing. The Levy Flight NM approach also reduces the chances of finding a local

maximum region, i.e., potentially triggered by detectable SLL at the array aperture which may perturb the search procedure and cause premature termination.

The proposed NM schemes are now analyzed using network simulation. The overall setup assumes an interference-free LoS environment with a single BS and MS. The operating frequency here, f_c, is set to 28 GHz and the channel bandwidth (BW) is set to 100 MHz. The other related parameters for the proposed NM schemes are also listed in Table 3.1. Detailed results are now presented for performance metrics to evaluate the efficiency of the above schemes.

First, the computational complexity of the beam access scheme is gauged using the total number of objective function evaluations for the beamforming and combining pairs (across all the hierarchical codebook stages). Namely, if $y_l(P_R) > y_l(P_W)$, the total number of measurements for the Von Neumann NM scheme, S_{VN}, is given by:

$$S_{VN}|y_l(P_R) > y_l(P_W) = Y(S_\Delta + S_{ref} + S_{nbr} + S_{exp}),$$ (3.15)

or if $y_l(P_R) > y_l(P_W)$, the number of measurements is given by:

$$S_{VN}|y_l(P_R) < y_l(P_G) = Y(S_\Delta + S_{ref} + S_{nbr} + S_{con} + S_{shr}),$$ (3.16)

where in order the variables S_Δ, S_{ref}, S_{nbr}, S_{exp}, S_{con}, and S_{shr} are defined as the number of steps at the traditional NM simplex, reflection point, Von Neumann locations, expansion point, contraction point, and shrinkage point. Similarly for the Levy Flight NM scheme, the number of measurements, S_{LF}, is given by:

$$S_{LF} = Y(S_{\Delta_1} + S_{\Delta_2} + S_B^{nbr}),$$ (3.17)

where S_{Δ_1}, S_{Δ_2}, and S_B^{nbr} are the number of steps in the initial two simplexes for the Levy Flight and the neighborhood of the best vertex, respectively. Based upon the above evaluations, Figure 3.8 plots the complexity of the proposed NM schemes compared to the conventional access

54

methods. Namely, Levy Flight NM features 99.3% and 78% reduction in computational complexity versus the exhaustive search [40], and the subarrays, single-sided and GPS schemes [42],[39],[35], respectively. The Levy Flight NM also performs its beam measurements by 43% and 25% less steps versus the iterative search and the beamtraining method for indoor WLAN in [58]. Among the proposed NM schemes, the Von Neumann search yields the lowest complexity, i.e., 25% and 10% less than the Chebyshev and traditional NM schemes.
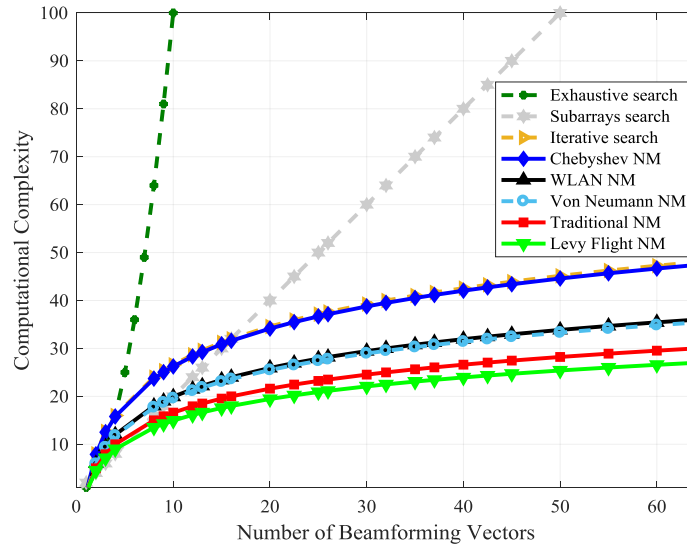

Figure 3.8: Nelder Mead computational complexity for different beamforming vectors

Now access time is another key performance parameter for beam access schemes. In particular this value, denoted here as T_a, is determined by the beamforming scan cycle time over all azimuth spatial directions in which PSS signaling is transmitted periodically on each beamforming/combining vector [55]. As a result, the access times for the Von Neumann and Levy Flight NM schemes in order are as $T_a = S_{VN} t_{PSS}/R_{MS}$ and $T_a = S_{LF} t_{PSS}/R_{MS}$, where t_{PSS} and R_{MS} are the PSS duration and the number of RF chains at the MS, respectively. These associated results are also shown in Figure 3.9.

Moreover, the Levy Flight NM scheme achieves the shortest access durations versus traditional access methods. Namely, its associated scan cycle is 99.3% shorter than the exhaustive search, 78% faster than subarrays method, the single-sided scheme, and the GPS search. Also, the Levy Flight NM converges 43% and 25% faster than the iterative search and the indoor WLAN access method. Indeed, the Levy Flight NM search also outperforms the traditional and Chebyshev NM schemes in terms of access times, i.e., 5.3 ms versus 5.8 ms and 8.5 ms, respectively.
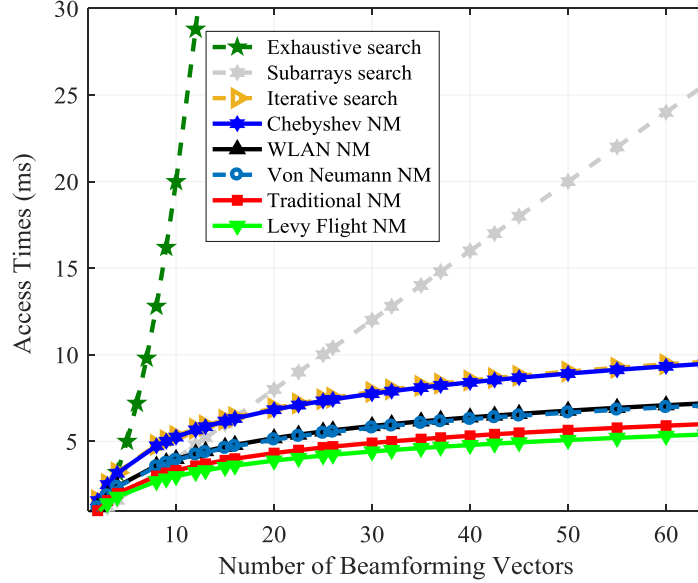
Figure 3.9: Access times for Nelder Mead techniques for different beamforming vectors

Furthermore, energy efficiency is another critical parameter for NM schemes. Specifically this value is computed as the power consumption (in millijoules) during the beam access time interval, i.e., given by $E_C = P_{MS}^{ABF} T_a$, where P_{MS}^{ABF} is the power consumption in the ABF at the MS and is defined as:

$$P_{MS}^{ABF} = 2[R_{MS}(N_{MS}^1 P_{PS}^1 + N_{MS}^2 P_{PS}^2 + N_{MS}^3 P_{PS}^3) + P_{LNA}(N_{MS}^1 + N_{MS}^2 + N_{MS}^3) + (P_{RF} + P_{ADC}) + P_{BB}], \quad (3.18)$$

$$P_{RF} = P_M + P_{LO} + P_{LPF} + P_{AMP}, \quad (3.19)$$

$$P_{ADC} = E_{ADC}^{step} Sr_{ADC} 2^W, \quad (3.20)$$

where N_{MS}^1, P_{PS}^1, N_{MS}^2, P_{PS}^2, N_{MS}^3, and P_{PS}^3 in order are the power consumption levels for the number of antennas and phase shifter in the three codebook stages at the MS. Furthermore, P_{LNA}, P_{RF}, P_{ADC}, P_{BB}, P_{M}, P_{LO}, P_{LPF}, and P_{AMP} denote in order, the power consumption for the *low noise amplifier* (LNA), RF chain, ADC, *baseband combiner* (BB), *mixer* (M), *local oscillator* (LO), *low pass filter* (LPF) and the *baseband amplifier* (AMP). Additionally, the terms $E_{\text{ADC}}^{\text{step}}$, Sr_{ADC}, and W in Eq. (3.20) denote the energy consumption per conversion, the sampling rate and the total number of bits, respectively [56]. Based upon the above, the total power consumption is plotted in Figure 3.10 (and the related consumption values in milliwatts for the different components are also summarized in Table 3.1, as derived from earlier studies in [57]).

Overall, the energy consumption results confirm that the proposed Levy Flight NM scheme herein delivers the minimum energy consumption levels over existing methods. Specifically, it requires 7.5 mJ to scan over 40 number of beamforming vectors compared to 13 mJ for the WLAN access method, 15 mJ for the iterative search, and 28 mJ for the subarrays, single-sided and GPS methods.
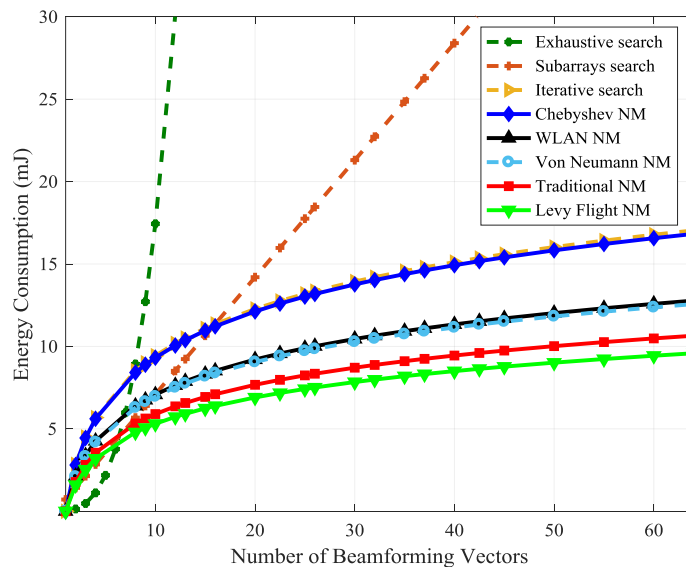
Figure 3.10: Nelder Mead energy consumption for different beamforming vectors

Finally, the success rates for the various NM schemes correspond to cases at which the received signal level exceed the predefined signal threshold, $y_{th}^\cdot$, that is sufficient to enable data transmission. Accordingly, Figure 3.11 plots the objective function (received signal levels) for the various access schemes in a large iterations window. Here the traditional, Von Neumann, Chebyshev and Levy Flight NM schemes give success rates of 87%, 97% and 100%, respectively. Based upon these findings, it is concluded the proposed NM schemes present very reliable techniques for rapid mmWave initial beam access.
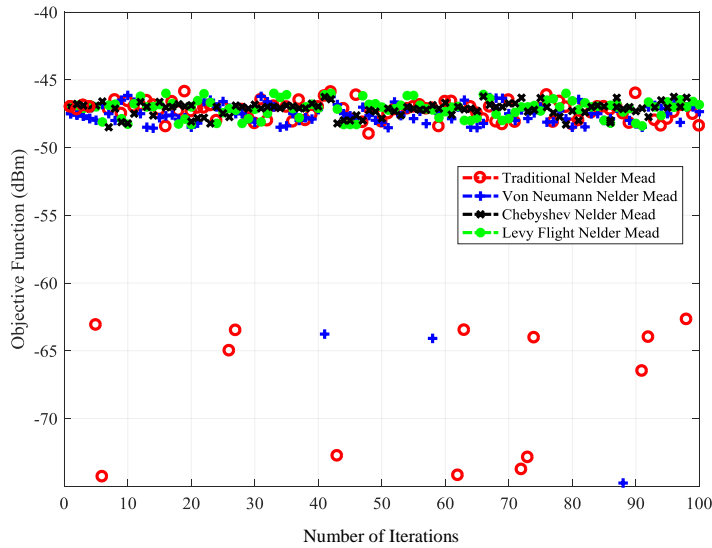
Figure 3.11: Number of iterations for the proposed Nelder Mead schemes

3.4 Efficient Search Schemes for NLoS Environments

Although mmWave networks are well-suited for LoS settings, wireless channels generally exhibit various fading levels and path gains. Hence further beam access procedures are required for NLoS propagation. Overall, the sparsity structure of such spatial mmWave channels can be exploited to relax beam search procedures. In particular, the presence of scarce local maxima can be utilized to adapt the search sequence and accelerate the detection of candidate spatial directions, i.e., where MPCs are collectively concentrated in a few *S* clusters. Along these lines, global optimization techniques are developed to detect the best beamforming directions in

NLoS environments, i.e., for different channel sparsity levels. In particular, these schemes utilize several global search methods, including Luus Jaakola (LJ), hybrid divide-and-conquer with Tabu search (DC-TS), coordinated generalized pattern search (CGPS) and Hooke Jeeves (HJ) methods.

3.4.1   Uniform Local Search Schemes

In general, uniform local search access schemes divide the search grid into congruent sections with uniform intervals, i.e., in order to improve search efficiency and convergence accuracy. The LJ and DC-TS schemes are classified as such are detailed first. Namely, a drastically-modified version of the traditional heuristic LJ scheme [59] is proposed for improved beam access. The modified LJ scheme in Figure 3.12 here constructs two adjacent sub-regions with uniform intervals, i.e., interior sub-region R_1 and exterior sub-region R_2. An arbitrary single point is then selected from each sub-region. Namely, a primary point P_1 is chosen from interior sub-region $R_1 \in R$ with boundaries specified by R_1^r and R_1^s,

$$R_1 = (R_1^r, R_1^s) \in \mathbb{R}^2 | R_1^r \sim U(r_{i_{min}}, r_{i_{min+\delta}}), R_1^s \sim U(s_{j_{min}},\ s_{j_{min+\delta}}), \tag{3.21}$$

and a secondary point P_2 is chosen from the exterior sub-region R_2, $P_2 \in R_2$, where $R_2(R_2^r, R_2^s)$ $= R - R_1$ and $R_1 \cup R_2 = R$. An auxiliary location is then constructed as $P_3 = P_1 + P_2$ and compared with P_2 for better assessment of candidate solutions in the exterior sub-region. Consequently, the point with the highest objective function (received signal) is set as the best exterior point, P_{ext}.

Now if the objective function at the exterior point $y_l(P_{ext})$ is less than the objective function at the primary point $y_l(P_1)$, i.e., $y_l(P_{ext}) > y_l(P_1)$, then the proposed LJ scheme explores the exterior sub-region defined by shrinking the sampling interval of the exterior point P_{ext} by the step size δ, i.e., to formulate a shrinkage point, P_{shr}. However, if the objective function at the

59

Inputs: Y, B, Q, δ.

$\delta = B/4, \delta \leq B\text{-}1$ // *Step size*

Initialization: $q = 0$ // *Iterations counter*

For $y \geq 1, y \leq Y, \forall\{(r_i, s_i)| 1 \leq r_i \leq B, 1 \leq s_j \leq B\}$ // *Start with codebook Stage I*

While $q < Q$ // *Number of iterations Bound*

  $P_1(r_1, s_1), P_1 \in R_1, \acute{y}_l(P_1)$ // *Select a primary point from sub-region R_1*

  $P_2(r_2, s_2), P_2 \in R_2, \acute{y}_l(P_2)$ // *Select a secondary point from sub-region R_2*

  $P_3(r_3, s_3) = P_1 + P_2$ // *Construct an auxiliary point*

  $P_{ext}(r_{ext}, s_{ext}) \leftarrow max\{\acute{y}_l(P_2), \acute{y}_l(P_3)\}$ // *Determine the exterior point*

    If $\acute{y}_l(P_{ext}) > \acute{y}_l(P_1)$

       $P_{shr}(r_{shr}, s_{shr}), P_{shr} \in R_{shr}, R_{shr} = (R_{shr}^r, R_{shr}^s)$ // *Shrinkage*

       $R_{shr}^r \sim U(r_{ext\text{-}\delta}, r_{ext+\delta}), R_{shr}^s \sim U(s_{ext\text{-}\delta}, s_{ext+\delta})$ // *Shrinking the sampling interval of the exterior point*

       $\acute{y}_l(P_{shr})$ // *Evaluate the objective function at the shrinkage point* P_{shr}

         If $\acute{y}_l(P_{shr}) > \acute{y}_l(P_{ext})$

            $P_1 \leftarrow P_{shr}, R_1 \leftarrow R_{shr}$

             If $q == Q, (r_i, s_j)_{bst_y} \leftarrow P_1, y \leftarrow y + 1$

               Else $q = q + 1$

          Else

            $P_1 \leftarrow P_{ext}, R_1 \leftarrow R_{ext}$

            If $q == Q, (r_i, s_j)_{bst_y} \leftarrow P_1, y \leftarrow y + 1$ // *The best point is selected for codebook Stage I*

               Else $q = q + 1$

            End

        End

    Else $\acute{y}_l(P_{ext}) \leq \acute{y}_l(P_1)$

        $P_1^{exp}(r_1^{exp}, s_1^{exp}), P_1^{exp} \in R_{exp}, R_{exp} = (R_{exp}^r, R_{exp}^s)$

        $R_{exp}^r \sim U(r_{i_{min}}, r_{i_{min+2\delta}}), R_{exp}^s \sim U(s_{j_{min}}, s_{j_{min+2\delta}})$

        $\acute{y}_l(P_1^{exp})$

          If $\acute{y}_l(P_1^{exp}) > \acute{y}_l(P_1)$

            $P_1 \leftarrow P_1^{exp}, R_1 \leftarrow R_{exp}$

            If $q == Q, (r_i, s_j)_{bst_y} \leftarrow P_1, y = y + 1$ // *The best point is selected for codebook Stage I*

              Else $q = q + 1$

            End

          Else

            If $q == Q, (r_i, s_j)_{bst_y} \leftarrow P_1, y = y + 1$ // *The best point is selected for codebook Stage I*

              Else $q = q + 1$

            End

          End If

      End If

  End While

End For

Figure 3.12: Luus Jaakola (LJ) beam access scheme

shrinkage point $y_l(P_{shr})$ is higher than the objective function at the exterior point $y_l(P_{ext})$, i.e., $y_l(P_{shr}) > y_l(P_{ext})$, then P_1 and P_{ext} are discarded and P_{shr} is set as the new primary point, $P_1 \leftarrow P_{shr}$. Otherwise, P_{ext} is considered as the primary point, $P_1 \leftarrow P_{ext}$. Conversely, if $y_l(P_{ext}) < y_l(P_1)$, then the exterior exploratory search has failed to return any candidates, and the vicinity of P_1 is chosen as the feasible sub-region. The LJ scheme then proceeds to expand around the vicinity of P_1, scaled by the step size in order to construct P_{exp}. This procedure is repeated for a number iterations $q=1,2,\ldots,Q$ with a stopping criterion set to $Q=B\text{-}1$, at which point the LJ scheme adapts the location of the primary point and the size of the sampling interval at each iteration.

Now a crucial design parameter for the proposed LJ scheme here is the interval length. If this value is too small relative to the feasible region, the search procedure can get trapped in a local maximum. Conversely, if the interval is too large, it may result in inaccurate and rapid convergence. However, this vulnerability can be easily mitigated by setting the step size of the uniform interval size relative to the feasible region, i.e., a rule of thumb is $\delta = B/4$. Note that the number of iterations grows linearly with the dimension of the feasible region, thus requiring a higher number of iterations to accurately converge in large search grids. As a result, the LJ scheme generally performs better in smaller feasible regions for solely-cascaded codebooks.

Furthermore, the primary point in the aforementioned LJ scheme can be alternatively selected by applying a hybrid pattern search procedure based upon the divide-and-conquer with Tabu search method [60], i.e., termed as DC-TS scheme. The first phase (Phase I) of this scheme is termed as the parallel sub-region search and divides the feasible region R into $\mathfrak{r}_b$ equally-adjacent sub-regions, $\mathfrak{r}_b \subseteq R, \sum_{\mathfrak{r}_b \in \mathbb{R}^2} \mathfrak{r}_b = B$. Next, the DC-TS scheme performs an inner pattern search (Phase II) in each sub-region, where a single random point is selected from each, $P_1^{\mathfrak{r}_b} \in \mathfrak{r}_b$.

Inputs: Y, B, δ

$\delta = B/4$ // *Step size*

Initialization: $T_L := \{\}$ // *Initial Tabu list is a null set*

For $y \geq 1$, $y \leq Y$, $\forall\{(r_i, s_j): 1 \leq r_i \leq B, 1 \leq s_j \leq B\}$

  Phase I: Parallel sub-region search

  $ᵹ_1(r_{ᵹ_1}, s_{ᵹ_1})$: $r_{ᵹ_1} = U(r_{i_{min}}, r_{i_{min+\delta}})$, $s_{ᵹ_1} = U(s_{j_{min}}, s_{j_{min+\delta}})$ // *Construct first sub-region and choose primary points*

  $ᵹ_2(r_{ᵹ_2}, s_{ᵹ_2})$: $r_{ᵹ_2} = U(r_{i_{min+2\delta}}, r_{i_{min+3\delta}})$, $s_{ᵹ_2} = s_{ᵹ_1}$ // *Construct a second sub-region and choose primary points*

  $ᵹ_3(r_{ᵹ_3}, s_{ᵹ_3})$: $r_{ᵹ_3} = r_{ᵹ_1}$, $s_{ᵹ_3} = U(s_{j_{min+2\delta}}, s_{j_{min+3\delta}})$ // *Construct a third sub-region and choose primary points*

  $ᵹ_4(r_{ᵹ_4}, s_{ᵹ_4})$: $r_{ᵹ_4} = r_{ᵹ_2}$, $s_{ᵹ_4} = s_{ᵹ_3}$ // *Construct a fourth sub-region and choose primary points*

  Phase II: Inner pattern search

  $P_1^{ᵹ_1} \in ᵹ_1$ // *Select a random primary point $P_1^{ᵹ_1}$ from sub-region*

  $P_1^{ᵹ_2} \in ᵹ_2$ // *Select a random primary point $P_1^{ᵹ_2}$ from sub-region*

  $P_1^{ᵹ_3} \in ᵹ_3$ // *Select a random primary point $P_1^{ᵹ_3}$ from sub-region*

  $P_1^{ᵹ_4} \in ᵹ_4$ // *Select a random primary point $P_1^{ᵹ_4}$ from sub-region*

  $P_1^{bst} \leftarrow max\{P_1^{ᵹ_b}: y(P_1^{ᵹ_1},..., P_1^{ᵹ_b})\}$ // *Identify the best point among all sub-regions*

  $ᵹ_H \leftarrow ᵹ_b | ᵹ_b \supset P_1^{bst}$ // *Select highest sub-region and highest primary points*

  $T_L \leftarrow \{ᵹ_b: \forall ᵹ_b < ᵹ_H\}$ // *First Tabu list*

  For $b = 1: B$-1

   If $\forall\{y_l': y_l'(P_1^{ᵹ_b})\} == y_l'(P_1^{ᵹ_{b+1}})$ // *If all signal levels are equal at all primary points*

    For $b = 1: B$

     $P_2^{ᵹ_b} | P_2^{ᵹ_b} \in ᵹ_b$ // *Select a random secondary point from each sub-region*

     $P_2^H \leftarrow max\{P_2^{ᵹ_b}: y_l'(P_2^{ᵹ_1},..., P_2^{ᵹ_b})\}$ // *Select the besy secondary point*

     $ᵹ_H \leftarrow ᵹ_b | ᵹ_b \supset P_2^{bst}$ // *Identify the highest sub-region $ᵹ_H$ containing the best secondary point*

     $T_L \leftarrow \{ᵹ_b: \forall ᵹ_b < ᵹ_H\}$ // *Second Tabu list*

    End For

   End If

  End For

  $P_1(r_1, s_1) \leftarrow P_1^{bst}$ // *Best primary point for the LJ scheme*

  $q = Q$ // *Terminate iterations*

  Start LJ scheme

  End For

Figure 3.13: DC-TS initial beam access scheme

Furthermore, the sub-region with the highest value of the objective function, $ᵹ_H$, that contains the best point $P_1^{bst} \in ᵹ_b$, is selected as the interval of the primary point in the LJ scheme. Meanwhile, other sub-regions are discarded and considered as Tabu sub-regions, $ᵹ_T$, i.e., $ᵹ_T \subseteq R$. These sub-regions have null feasible solutions, $S \notin ᵹ_T$, and hence are defined as prohibited sub-regions which the hybrid scheme cannot revisit. As a result, these regions are stored in a Tabu list, T_L, in order to be excluded from the primary point selection in the LJ

scheme, $\exists r_T | y_l'(\forall P(r_i, s_j) < y_{th}', \forall P(r_i, s_j) \in r_b)$. Note that the Tabu list is reset after the selection of the primary point in each codebook stage. Furthermore, if the function values at all sub-regions are equal, then an additional random point $P_2^{r_b} \in r_b$ is also selected from each sub-region in order to determine the best sub-region. Overall, the hybrid DC-TS scheme returns r_b function outcomes in Phase II and only a single point is fed into the LJ scheme. Subsequently, LJ scheme is initiated and the exterior regional search is triggered. The overall sequence for this search scheme for $B=4$ is illustrated in Figure 3.13.

Overall, the proposed hybrid DC-TS scheme has several key advantages. First, it yields a reduced search space, thereby linearly increasing the detection probability by a rate of B. Also, this method reduces the tendency to get trapped in plateau regions when the feasible region is large. Moreover, the Tabu search mechanism also eliminates recursive searches in sub-regions with poor objective function values, i.e., in which such-regions are unable to return global or local maxima after Q iterations. Such conditions may occur when the zero elements of the channel sparse matrix fall at the array boresight.

The proposed LJ and DC-TS uniform local search schemes are now evaluated for a single BS communicating with a single MS. In contrast to the previous LoS scenario, the operating frequency (f_c) is now set to 38 GHz and the channel bandwidth (BW) is set to 500 MHz, i.e., in order to introduce more severe sparsity levels. However the same beamformer in Section 3.1 is also used here (see Table 3.1 for codebook and ULA settings), and the various other system parameters are summarized in Table 3.2. Detailed NLoS results are now presented for a range of performance evaluation metrics.

Foremost, the computational complexity in the worst case scenario for LJ scheme, S_{LJ}, is gauged by the total number of measurements at each codebook stage, given by:

$$S_{\text{LJ}} = Q(S_{\text{pri}} + S_{\text{sec}} + S_{\text{aux}} + S_{\text{shr (exp)}}), \tag{3.22}$$

where the variables S_{pri}, S_{sec}, S_{aux}, and $S_{\text{shr (exp)}}$ in order are the number of steps for the objective

function evaluations at the primary, secondary, auxiliary and shrinkage (or expansion) points.

Meanwhile for DC-TS scheme, this modified count at each codebook stage is given by:

$$S_{\text{DC-TS}} = B(S_{\text{pri}} + S_{\text{sec}}) + S_{\text{LJ}}|_{Q=1}, \tag{3.23}$$

where $S_{\text{LJ}}|_{Q=1}$ is the objective function evaluation steps for the LJ scheme for a single iteration,

i.e., Eq. (3.22). The results are plotted in Figure 3.14 and confirm that the proposed LJ and DC-

TS schemes can perform beam search with much fewer measurements versus existing solutions

(as a function of beamforming vectors). Note that the complexity of both schemes exhibits

logarithmic growth as the number of beamforming vector increases, modeled as $O(S_{\text{LJ}} \log_4(B^2))$

and $O(S_{\text{DC-TS}} \log_4(B^2))$ for the LJ and DC-TS schemes, respectively. Namely, LJ and DC-TS

schemes require 99.12%, 71.87%, and 25% less measurements (steps) for the objective function

compared to the exhaustive, iterative, single-sided and subarrays search methods. Here, these

schemes require 36 steps to detect the highest signal using a three-staged codebook of 64 pencil

beams. This is compared to 48, 128 and 4096 steps for the iterative, subarrays (single-sided), and

exhaustive search methods.

Table 3.2: System settings for the LJ, DC and TS beam access

Category	Parameters	Value
System	f_c (GHz), BW (MHz), y_{th}	38, 500, -128 [61]
Channel	∂, σ_w^2, r (m)	0, 1, 50
Uniform local search schemes	δ, Q	1, 3
Path loss, *LogN*	α_{fl}(dB), ρ_{sl} (dB), σ_s(dB)	117, 0.4, 8.3
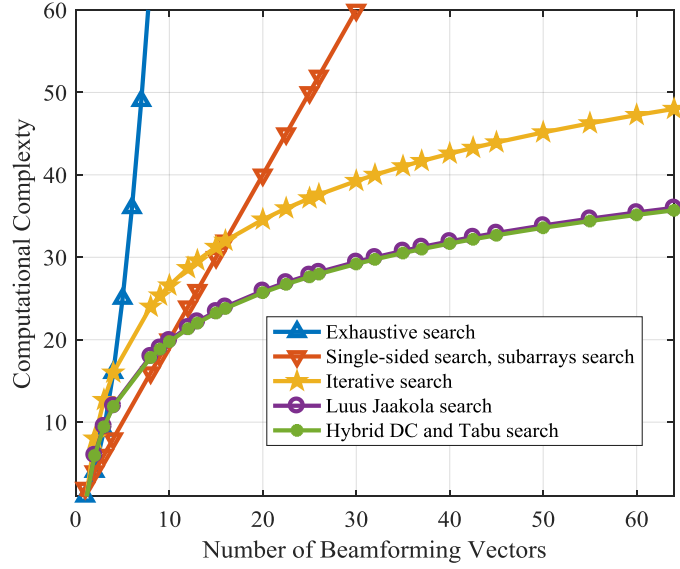
Figure 3.14: Computational complexity for uniform local search schemes

Meanwhile, the access time T_a is also shown in Figure 3.15 and is computed in a similar manner to the previous access schemes, i.e., $T_a = S_{LJ} t_{PSS}/R_{MS}$ and $T_a = S_{DC\text{-}TS} t_{PSS}/R_{MS}$ for the LJ and DC-TS schemes, respectively. These results confirm that the proposed search LJ and DC-TS search schemes also deliver significant improvements versus existing solutions. Specifically, the proposed LJ and DC-TS schemes are 99.12%, 71.87%, and 25% faster than the exhaustive, the iterative, the single-sided and subarrays search methods. Namely, LJ and DC-TS schemes require 7 ms to detect the highest signal level using 64 beams, compared to 10-820 ms for the other methods.
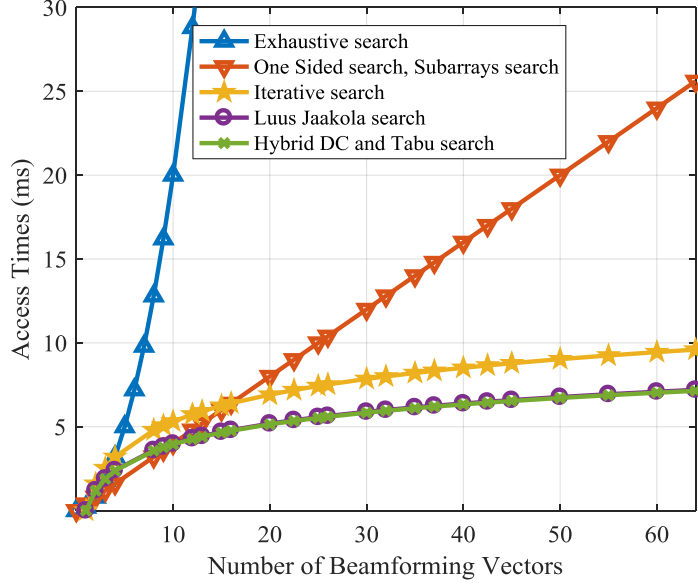
Figure 3.15: LJ access times for different beamforming vectors

3.4.2 Coordinated Generalized Pattern Search (CGPS)

Another NLoS access solution is also developed based upon the coordinated generalized pattern search (CGPS) method. Namely, it was originally developed in [62] and works by locally polling the objective function in an asymptotically dense set of directions around an incumbent solution, i.e., forming a search pattern. Hence, this method is also applied to beam access and is comprised of both exploratory bisectional and polling phases. Namely, the beam search sequence is adopted based upon the outcomes of the objective function. Furthermore, instead of sweeping the entire spatial plane, only a limited number of directions are tested here in order to determine the best beamforming and combining vectors. The overall access pseudocode for the proposed CGPS scheme is presented in Figure 3.16 and consists of two stages. Consider the details.

1) Phase I: Exploratory Bisection Search

The first phase of the CGPS scheme searches for a candidate incumbent point using bisectional filtering, where the search grid $\hat{G}$, is divided into $\mathcal{B}_x$, equally-sized bisections, $\mathcal{B}_x \subset \hat{G}$, $\mathcal{B}_x \in \mathbb{R}^\eta$, $x=1, 2,\ldots, X$, $X = ij/2\eta$. Here the size and boundaries of each bisection, $\Lambda_{\mathcal{B}_x}$, are

66

determined by the mesh scale parameter, δ (as used in Figure 3.16). Furthermore, each $\mathcal{B}_x$ consists of finite set of mesh points $\acute{P}_m$, $m=1, 2,\ldots,M$. Initially, a primary point is selected from each mesh within each bisection, $\acute{P}_m^a \in \mathcal{B}_x$, and the scheme returns a total of X objective function evaluations at each bisection. The bisection returning the highest value of objective function, $\mathcal{B}_x^{\mathrm{Hi}}$, that contains the highest (best) point, $\acute{P}_m^{\mathrm{Hi}} \in \mathcal{B}_x^{\mathrm{Hi}}$ is then selected for further mesh refinement in the polling phase. However, if Phase I does not return a candidate bisection, $\nexists\, S \in \mathcal{B}_x$, $\forall y_l'(\acute{P}_m) = y_l'(\acute{P}_{m+1})$, then the CGPS scheme examines a secondary point, $\acute{P}_m^b \in \mathcal{B}_x$.

2) Phase II: Polling Search

This phase performs deterministic local exploration in the vicinity of the incumbent solution, $\acute{P}_m^{\mathrm{Hi}}$. Namely d_p polling directions are centered at $\acute{P}_m^{\mathrm{Hi}}$, denoted as $d_p = 1, 2,\ldots, D_p$, $d_p \subset D_p, D_p = 2\eta, D_p \in \mathbb{R}$. A set of polling points is then constructed as well, Ч$_p$, $p=1,2,\ldots,P$, $P = D_p$. In particular, these points are spaced at distance Δ from $\acute{P}_m^{\mathrm{Hi}}$ along D_p, i.e., Ч$_p = \{\acute{P}_m^{\mathrm{Hi}}(r_{i\pm\Delta},\, s_{j\pm\Delta})\}$, where Δ is the direction scale size, $\Delta = B/X$. Hence the objective function is evaluated at all points in Ч$_p$, and the highest value, Ч$_p^{\mathrm{Hi}} = (r_i,\, s_i)_{bst_y}$ is chosen as the best point for y and inserted into the successive codebook stage.

Overall, the proposed CGPS scheme presents several key advantages. Foremost, its non-sequential beam index search effectively examines distantly-separated angular directions that resemble the behavior of sparsely-received spatial lobes. Also, the detection of an incumbent solution (after the first phase) yields a reduced search space which linearly increases detection probability. Consequently, the probability of detecting high signal at the input of the polling phase is:

$$\mathbb{P}\left[\acute{y}_l(\acute{P}_m(r_i, s_j))_{bst_y}\right] = \begin{cases} \dfrac{1}{X}, \ \textit{for } m = 1 \\[2ex] \dfrac{1}{X-(m-1)} \displaystyle\prod_{\acute{t}=1}^{\acute{T}=m\text{-}1} \dfrac{X-\acute{t}}{X-(\acute{t}-1)}, \textit{for } m \geq 2. \end{cases} \tag{3.24}$$

Inputs: Y, B, η, Δ, δ

Phase I: Exploratory bisectional search

For $y \geq 1$, $y \leq Y$, $\forall\{P_k(r_i, s_i) \in \hat{G}\}$ // *Construct bisections*

 For $x \geq 1$

   $\acute{P}_m^a \in \mathcal{B}_x$, $\acute{y}_l(\acute{P}_m^a)$, $x+1 \leftarrow x$ // *Select primary mesh points*

    $\acute{P}_1^a \in \mathcal{B}_1 | \Lambda_{\mathcal{B}_1} = (r_{\mathcal{B}_1}, s_{\mathcal{B}_1})$: $r_{\mathcal{B}_1} = U(r_{i_{min}}, r_{i_{min+\delta}})$, $s_{\mathcal{B}_1} = U(s_{j_{min}}, s_{j_{min+\delta}})$

   $\acute{P}_2^a \in \mathcal{B}_2 | \Lambda_{\mathcal{B}_2} = (r_{\mathcal{B}_2}, s_{\mathcal{B}_2})$: $r_{\mathcal{B}_2} = U(r_{i_{min+2\delta}}, r_{i_{min+3\delta}})$, $s_{\mathcal{B}_2} = s_{\mathcal{B}_1}$

   $\acute{P}_3^a \in \mathcal{B}_3 | \Lambda_{\mathcal{B}_3} = (r_{\mathcal{B}_3}, s_{\mathcal{B}_3})$: $r_{\mathcal{B}_3} = r_{\mathcal{B}_1}$, $s_{\mathcal{B}_3} = U(s_{j_{min+2\delta}}, s_{j_{min+3\delta}})$

   $\acute{P}_4^a \in \mathcal{B}_4 | \Lambda_{\mathcal{B}_4} = (r_{\mathcal{B}_4}, s_{\mathcal{B}_4})$: $r_{\mathcal{B}_4} = r_{\mathcal{B}_2}$, $s_{\mathcal{B}_4} = s_{\mathcal{B}_3}$

 End For

   $\acute{P}_m^{Hi} \leftarrow max\{\forall \acute{P}_m^a : \acute{y}_l(\acute{P}_1^a,..., \acute{P}_m^a)\}$ // *Primary mesh points test*

   $\mathcal{B}_x^{Hi} \leftarrow \mathcal{B}_x | \mathcal{B}_x \supset \acute{P}_m^{Hi}$

  If $\forall \acute{y}_l(\acute{P}_m^a) \neq \acute{y}_l(\acute{P}_{m+1}^a)$

    Phase II: Polling Search

      For $p \geq 1$,   // *Construct D polling directions*

       Ч$_p = \{\acute{P}_m^{Hi}(r_{i\pm\Delta}, s_{j\pm\Delta})\}$, $\acute{y}_l($Ч$_p)$

     End For

      Ч$_p^{Hi} \leftarrow max\{\acute{y}_l \forall ($Ч$_p) : \acute{y}_l($Ч$_1,..,$Ч$_p)\}$, $y+1 \leftarrow y$

  Else

    For $x \geq 1$

      $\acute{P}_m^b \in \mathcal{B}_x$, $\acute{y}_l(\acute{P}_1^b)$, $x+1 \leftarrow \boldsymbol{x}$ // *Select secondary mesh points*

    End For

     $\acute{P}_m^{Hi} \leftarrow max\{\acute{y}_l(\forall \acute{P}_m^{Hi} \in \mathcal{B}_x) : \acute{y}_l(\acute{P}_1^b,.., \acute{P}_m^b)\}$

     $\mathcal{B}_x^{Hi} \leftarrow \mathcal{B}_x | \mathcal{B}_x \supset \acute{P}_m^{Hi}$

     For $p \geq 1$,   // *Perform polling search*

        Ч$_p = \{\acute{P}_m^{Hi}(r_{i\pm\Delta}, s_{j\pm\Delta})\}$

     End For

        Ч$_p^{Hi} \leftarrow max\{\forall$Ч$_p : \acute{y}_l($Ч$_1,...,$Ч$_p)\}$, $y+1 \leftarrow y$

   End If

End For

Figure 3.16: CGPS scheme for initial beam access

The proposed CGPS scheme is also evaluated for a single BS and MS operating in a wideband setting, i.e., 1 GHz channel bandwidth. The design parameters used for the codebook, link budget, and access scheme parameters are also summarized in Table 3.3. Detailed results for

a range of performance evaluation metrics are now presented, and in particular comparisons are made versus the iterative, exhaustive, single-sided and subarrays search methods.

Table 3.3: System settings for the CGPS beam access

Category	Parameters	Value
System	f_c(GHz), BW (GHz)	38, 1
Channel	∂(dB), σ_w^2(dB), r(m),α(dB), Γ(dB), σ_s(dB)	0, 1, 50, 117, 0.4, 8.3
CGPS	η, δ, Δ	2,1, 1

First consider the worst-case number of objective function measurements at the beam indices pair (at each codebook stage y of the proposed CGPS scheme). This value is given by:

$$Q_y^{\text{CGPS}} = Y[Q(\acute{y}_l(\acute{P}_m^a)) + Q(\acute{y}_l(\acute{P}_m^b)) + Q(\acute{y}_l(Ч_p))], \tag{3.25}$$

where $Q(\acute{y}_l(\acute{P}_m^a))$, $Q(\acute{y}_l(\acute{P}_m^b))$, and $Q(\acute{y}_l(Ч_p))$, in order, are the number of objective function evaluations at the primary and secondary mesh points and polling points. Furthermore, the scheme complexity is also scaled by $O[Q_y^{\text{CGPS}}\log_4(B^2)]$, since the iterative search is repeated similarly in each codebook stage y using B number of predefined beams at the BS and MS nodes. The resultant complexity for the CGPS scheme is plotted in Figure 3.17. It is noticed here that the proposed scheme delivers very favorable (reduced) complexity overheads versus existing solutions. Namely, the proposed CGPS scheme here provides 99.12% less number of measurements for the objective function compared to the exhaustive search, 25% reduced computational complexity versus the iterative search, and 71.87% reduced complexity overheads than the subarrays, single-sided and GPS search methods.
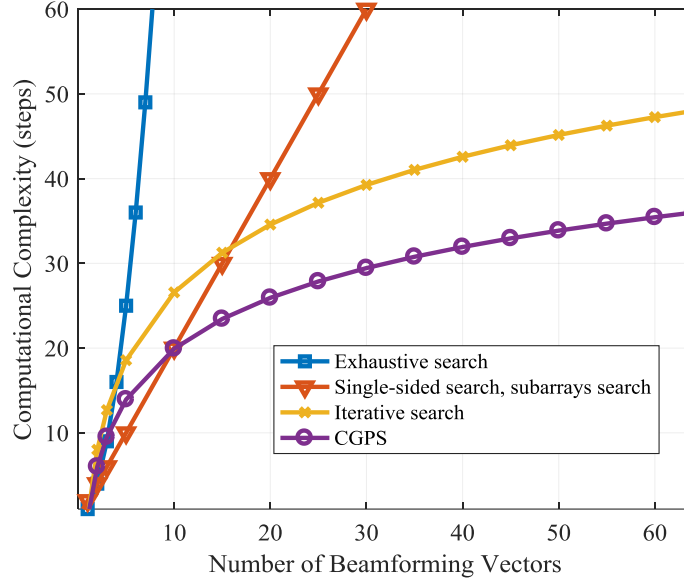
Figure 3.17: CGPS computational complexity for different beamforming vectors

Next, the access time is also gauged as $T_a = Q_y^{CGPS} \tau_{PSS}/R_{MS}$ similar to the LoS case (Section 3.3.2). These values are plotted in Figure 3.18, and show that the proposed CGPS access scheme delivers noticeable reduction rates in beam access times for the NLoS environments. Specifically, the proposed CGPS scheme here requires 7.2 ms to determine the spatial direction for the highest signal level. This is compared to the 9.6, 25.6, and 819.2 ms access times for the iterative, subarrays (single-sided and GPS) and the exhaustive search methods, respectively.
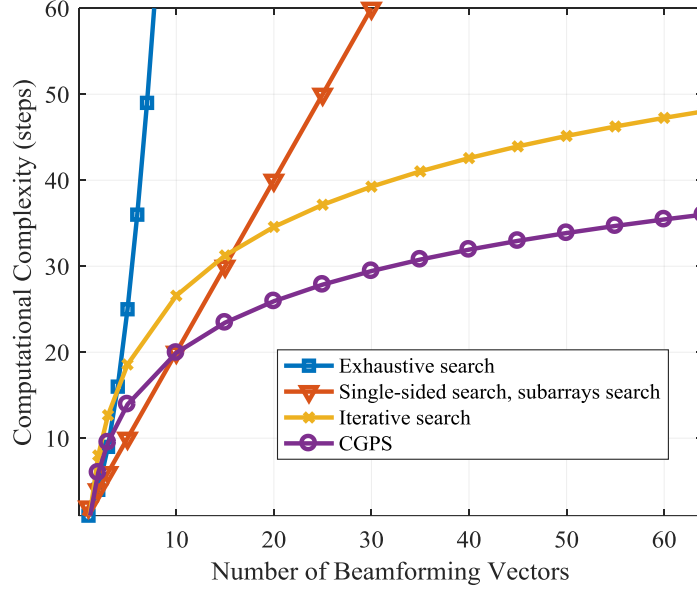
Figure 3.18: CGPS access times for different beamforming vectors

3.4.3 Adaptive Hooke Jeeves (HJ) Beam Access Scheme

Finally, a modified version of the Hooke Jeeves (HJ) adaptive search method is also developed to solve the beam access problem, see Figure 3.19. The HJ method was originally provides in [63],[64] and can be classified as a fast random pattern search technique due to its gradient-free nature. Hence this approach presents an effective option for initial beam access search as well. Again, the HJ scheme in Figure 3.19 comprises of two exploratory search phases, i.e., a primary (Phase I) and a secondary (Phase II). Consider some further details here.

In the initial Phase I search, the BS and MS nodes randomly select an initial beam indices pair, represented by the grid point $\mathcal{P}_1$, $\mathcal{P}_1(r_i, s_i) \in \hat{G}$, and measures the objective function at this point, $\hat{y}_l(\mathcal{P}_1)$. An exploratory search is then conducted by further perturbing $\mathcal{P}_1$ to find an improved value of the objective function. Namely, equal-length perturbation vectors are constructed in the vicinity of $\mathcal{P}_1$ and the HJ method is used to generate a total of $2^\eta + 2$ possible directional perturbations for each grid point. These vector perturbations are then further divided

71

Inputs: *Y*, *B*, i, j, δ, ϑ, δ = *B*/4
Initialization:
Perturbation vectors: ΔP_k^{pert}: ΔP_k^{UW}, ΔP_k^{DW}, ΔP_k^{SW}
For $y \geq 1$, $y \leq Y$, $\forall \{P_k(r_i, s_i): 1 \leq i \leq B, 1 \leq j \leq B\}$
 Phase I: // *Primary exploratory search*
 $P_1(r_i, s_i) \in (0, B)$, $y_l(P_1)$ // *Random initial point*
 $y_l(P_1^{UW1})$, $y_l(P_1^{UW2})$ // *Start upward perturbations*
 If $y_l(\Delta P_1^{UW}) > y_l(P_1)$, $P_1^{pert} \leftarrow max(\Delta P_1^{UW})$
    $P_2 = P_1 + \vartheta(P_1^{pert} - P_1)$, $y_l(P_2)$ // *Set tentative point*
    If $y_l(P_2) > y_l(P_1^{pert})$,
       Phase II: // *Secondary exploratory search around* P_2
        $y_l(P_2^{UW1})$, $y_l(P_2^{UW2})$ // *Upward perturbations*
        If $y_l(\Delta P_2^{UW}) > y_l(P_2)$, $P_2^{pert} \leftarrow max(\Delta P_2^{UW})$, $y \leftarrow y + 1$
          Else if
          $y_l(P_2^{DW}) > y_l(P_2)$, $P_2^{pert} \leftarrow max(\Delta P_2^{DW})$, $y \leftarrow y + 1$
          Else if
          $y_l(P_2^{SW}) > y_l(P_2)$, $P_2^{pert} \leftarrow max(\Delta P_2^{SW})$, $y \leftarrow y + 1$
          Else $P_2^{pert} \leftarrow P_2$, $y \leftarrow y + 1$
        End if
       Else $(r_i, s_j)_{bst_y} \leftarrow P_1^{pert}$ // *If* $P_2 \leq P_1^{pert}$
     End if
  Else if // *Downward perturbations*
    $y_l(P_1^{DW1})$, $y_l(P_1^{DW2})$
    $y_l(P_1^{DW}) > y_l(P_1)$, $P_1^{pert} \leftarrow max(\Delta P_1^{DW})$, $y_l(P_2)$
    If $y_l(P_2) > y_l(P_1^{DW})$, do Phase II for P_2
       $P_2^{pert} \leftarrow max\{P_2, \Delta P_2^{UW}, \Delta P_2^{DW}, \Delta P_2^{SW}\}$, $y \leftarrow y + 1$
      Else $(r_i, s_j)_{bst_y} \leftarrow P_1^{pert}$, $y \leftarrow y + 1$
    End if
  Else if // *Sideways perturbations*
    $y_l(P_1^{SW1})$, $y_l(P_1^{SW2})$
    $y_l(\Delta P_1^{SW}) > y_l(P_1)$, $P_1^{pert} \leftarrow max(\Delta P_1^{SW})$, $y_l(P_2)$
    If $y_l(P_2) > y_l(\Delta P_1^{SW})$, do Phase II for P_2
       $P_2^{pert} \leftarrow max\{P_2, \Delta P_2^{UW}, \Delta P_2^{DW}, \Delta P_2^{SW}\}$, $y \leftarrow y + 1$
      Else $(r_i, s_j)_{bst_y} \leftarrow max(\Delta P_1^{SW})$, $y \leftarrow y + 1$
    End if
  Else
       $(r_i, s_j)_{bst_y} \leftarrow y_l(P_1)$, $y \leftarrow y + 1$
 End if
End for

Figure 3.19: Adaptive Hooke Jeeves (HJ) initial beam access scheme

into three different categories, i.e., upward, ΔP_1^{UW}, downward, ΔP_1^{DW}, and sideways perturbations, ΔP_1^{SW}. Note that the lengths of these perturbation vectors are determined by the perturbation tolerance parameter, δ, as used in Figure 3.19. Subsequently the receives signal $y_l(P_1)$ is compared to the outputs at $y_l(\Delta P_1^{UW})$, $y_l(\Delta P_1^{DW})$, and $y_l(\Delta P_1^{SW})$, where the directional perturbations are defined as follows:

$$\Delta P_k^{UW} = \{P_k^{UW1}, P_k^{UW2}\}, \text{ where } P_k^{UW1} = (r_{i+\delta}, s_{j+\delta}), P_k^{UW2} = (r_{i-\delta}, s_{j+\delta}), \tag{3.26}$$

$$\Delta P_1^{DW} = \{P_k^{DW1}, P_k^{DW2}\}, \text{ where } P_k^{DW1} = (r_{i+\delta}, s_{j-\delta}), P_k^{DW2} = (r_{i-\delta}, s_{j-\delta}), \tag{3.27}$$

$$\Delta P_k^{SW} = \{P_k^{SW1}, P_k^{SW2}\}, \text{ where } P_k^{SW1} = (r_{i+\delta}, s_j), P_k^{SW2} = (r_{i-\delta}, s_j). \tag{3.28}$$

Now if the objective function fails to return an improved value using upward vectors, then the other directional perturbations are tested next. Specifically, if $y_l(\Delta P_1^{UW}) < y_l(P_1)$, then ΔP_1^{DW} is evaluated. Meanwhile, if $y_l(\Delta P_1^{DW}) < y_l(P_1)$, then the sideways perturbations are triggered, $y_l(\Delta P_1^{SW})$. Finally, if all directional perturbations do not yield any improvements, then P_1 is considered as the best point for stage y without the need for Phase II. However, if any of the perturbations exceeds P_1, then the search procedure proceeds to the follow-on exploratory search (Phase II), i.e., if $y_l(\Delta P_1^{UW}) > y_l(P_1)$ or $y_l(\Delta P_1^{DW}) > y_l(P_1)$ or $y_l(\Delta P_1^{SW}) > y_l(P_1)$. Namely the point with the highest received signal, P_1^{pert}, is used as input for Phase II (Figure 3.19). Also, the associated probabilities of detecting the highest signal via the upward, downward and sideways perturbations can also be written as:

$$\mathbb{P}\left[y_l(\Delta P_1^{UW})_{bst_y}\right] = \begin{cases} \dfrac{\mathcal{N}_{UW}}{B^2}, & \text{for } k = 1, \\ \dfrac{\mathcal{N}_{UW}}{B^2 - (k-1)} \displaystyle\prod_{\hat{t}=1}^{\hat{T}=k-1} \dfrac{B^2 - \hat{t}}{B^2 - (\hat{t}-1)}, & \text{for } k \geq 2. \end{cases} \tag{3.29}$$

$$
\mathbb{P}\left[y_l(\Delta P_1^{DW})_{bst_y}\right] = \begin{cases} \dfrac{\mathcal{N}_{DW}}{B^2}, & for\ k=1, \\[3ex] \dfrac{\mathcal{N}_{DW}}{B^2-(k-1)} \displaystyle\prod_{t=1}^{\check{T}=k\text{-}1} \dfrac{B^2-t}{B^2-(t-1)}, & for\ k \geq 2. \end{cases} \tag{3.30}
$$

$$
\mathbb{P}\left[y_l(\Delta P_1^{SW})_{bst_y}\right] = \begin{cases} \dfrac{\mathcal{N}_{SW}}{B^2}, & for\ k=1, \\[3ex] \dfrac{\mathcal{N}_{SW}}{B^2-(k-1)} \displaystyle\prod_{t=1}^{\check{T}=k\text{-}1} \dfrac{B^2-t}{B^2-(t-1)}, & for\ k \geq 2, \end{cases} \tag{3.31}
$$

where $\mathcal{N}_{UW}$, $\mathcal{N}_{DW}$, and $\mathcal{N}_{SW}$, are the number of upward, downward and sideward directional perturbation vectors in Phase I, respectively, i.e., $\mathcal{N}_{UW} = \mathcal{N}_{DW} = \mathcal{N}_{SW} = \eta$. Specifically, the above probabilities are derived based upon the memoryless properties of random beam access, i.e., discrete uniform probability distribution. Meanwhile, the second phase (Phase II) constructs a tentative point, P_2, based upon P_1 and P_1^{pert}, given by:

$$
P_2 = P_1 + \vartheta(P_1^{pert} - P_1), \tag{3.32}
$$

where ϑ is the acceleration coefficient, $\vartheta \in \mathbb{R} | \vartheta > 0$ that explores the neighborhood of P_1^{pert}. Akin to Phase I, a new set of directional perturbation vectors (upward, downward and sideways) are also constructed around P_2 to find the best beam pair with the highest received signal, i.e., $P_2^{pert} = (r_i, s_j)_{bst_y}$. Similarly, the probability of detecting the highest signal level at P_2 is given by:

$$
\mathbb{P}\left[y_l(P_2)_{bst_y}\right] = \begin{cases} \dfrac{B^2 - \mathcal{N}_{UW} - \mathcal{N}_{DW} - \mathcal{N}_{SW}}{B^2}, & for\ k=1, \\[3ex] \dfrac{B^2 - \mathcal{N}_{UW} - \mathcal{N}_{DW} - \mathcal{N}_{SW}}{B^2-(k-1)} \displaystyle\prod_{t=1}^{\check{T}=k\text{-}1} \dfrac{B^2-t}{B^2-(t-1)}, & k \geq 2. \end{cases} \tag{3.33}
$$

Overall, the adaptive HJ scheme does not exhaust all perturbations and usually converges to the highest signal level at an earlier stage. However the increased number of perturbations

improves overall success rates at the expense of higher computational complexity. Additionally, for LoS Gaussian channels with single cluster and severely-sparse channels, such as rural environment, this method can be further enhanced to improve detection by doubling the perturbation tolerance.

Several additional points are also noted here. Foremost, the perturbation tolerance parameter, δ, dictates the least possible perturbation vector length that can be explored in the vicinity of an initial point. Meanwhile, the acceleration coefficient, ϑ, plays a crucial role in controlling HJ convergence behavior. For example, large values can cause the scheme to terminate prematurely at a local point, whereas small values can confine the scheme to restricted sections of the search space. Finally, the implicit global search here resembles a gradient direction, and thereby yields improved search directions without having to compute derivatives of the objective function, i.e., classified as a quasi-gradient global search. This property allows the adaptive HJ method to achieve good accuracy with low complexity, a key saliency.

The proposed adaptive HJ scheme is now evaluated for a single BS and MS nodes operating in a wideband environment. Again, performance is measured for a range of metrics for various system parameters shown in Table 3.4. First, the worst-case number of objective function measurements/evaluations in codebook stage y (for the adaptive HJ scheme), Q_y^{HJ}, is computed as:

$$Q_y^{\mathrm{HJ}} = Y[Q(y_l(\mathrm{P}_1)) + Q(y_l\{\Delta \mathrm{P}_1^{\mathrm{UW}}\}) + Q(y_l\{\Delta \mathrm{P}_1^{\mathrm{DW}}\}) + Q(y_l\{\Delta \mathrm{P}_1^{\mathrm{SW}}\}) + Q(y_l(\mathrm{P}_2)) + Q(y_l\{\Delta \mathrm{P}_2^{\mathrm{UW}}\}) +$$

$$Q(y_l\{\Delta \mathrm{P}_2^{\mathrm{DW}}\}) + Q(y_l\{\Delta \mathrm{P}_2^{\mathrm{SW}}\})], \tag{3.34}$$

where $Q(y_l(\mathrm{P}_1))$, $Q(y_l\{\Delta \mathrm{P}_1^{\mathrm{UW}}\})$, $Q(y_l\{\Delta \mathrm{P}_1^{\mathrm{DW}}\})$, and $Q(y_l\{\Delta \mathrm{P}_1^{\mathrm{SW}}\})$, denote in order, the number of objective function evaluations at the initial point and its upward, downward and sideways perturbations locations. Also the variables, $Q(y_l(\mathrm{P}_2))$, $Q(y_l\{\Delta \mathrm{P}_2^{\mathrm{UW}}\})$, $Q(y_l\{\Delta \mathrm{P}_2^{\mathrm{DW}}\})$, and

$Q(\mathring{y}_l\{\Delta P_2^{SW}\})$ in Eq. (3.34) denote the number of times the objective function is evaluated at the tentative points and its upward, downward and sideways perturbation directions, respectively. Based on the above, Figure 3.20 plots the computational complexity of the adaptive HJ beam access scheme along with various other methods. For instance, the HJ scheme yields to the highest objective function value (received signal level) in 42 measurements (steps) versus is 4096, 128, and 48 steps for the exhaustive, iterative, and subarrays (single-sided) search methods.
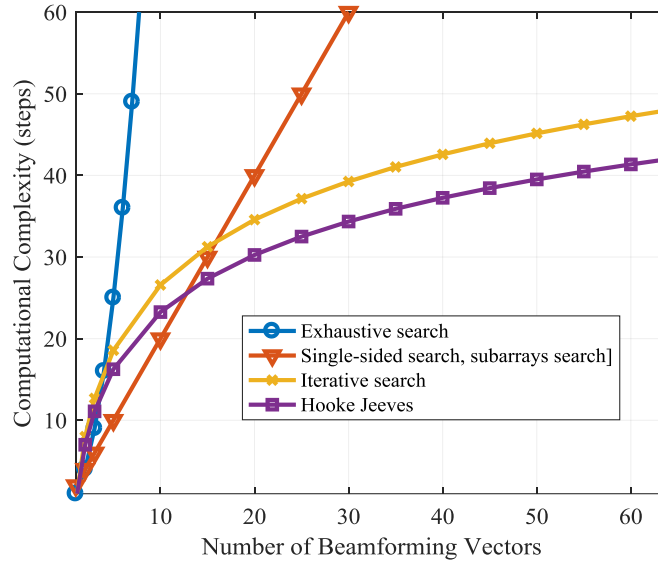
Figure 3.20: HJ computational complexity for different beamforming vectors

Table 3.4: System settings for the HJ beam access

Category	Parameters	Value
System	f_c(GHz), BW (MHz)	38, 500
Channel	∂(dB),σ_w^2(dB), r(m),α(dB), ρ(dB), σ_s(dB)	0, 1, 50, 117, 0.4, 8.3
HJ scheme	η, δ, ϑ, $\mathcal{N}_{UW}$, $\mathcal{N}_{DW}$, $\mathcal{N}_{SW}$	2, 1, 1, 2, 2, 2

Next, the access time for the HJ approach is also derived by $T_a = Q_y^{HJ}\tau_{PSS}/R_{MS}$, and plotted in Figure 3.21. The results here indicate the fastest access (lowest delays) with the proposed adaptive HJ solution, i.e., 98.9%, 67.2% and 12.5 % shorter access times and reduced

control latencies for $B \geq 15$ beams, compared to the exhaustive, iterative, and subarrays (single-sided) search methods.
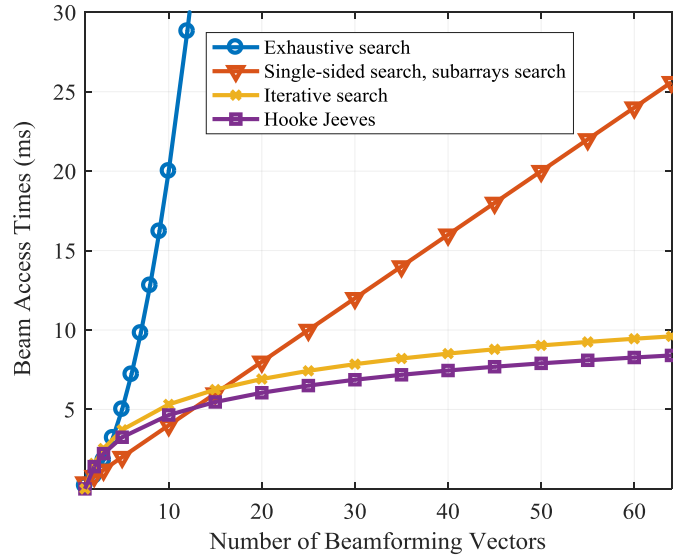
Figure 3.21: HJ access times for different beamforming vectors

Finally, the energy efficiency for the adaptive HJ scheme is also plotted in Figure 3.22. This value is measured by the power consumption during beam access times, i.e., $E_C = P_{MS}^{ABF} T_a$, as introduced in Section 3.3.2. The proposed scheme here features noticeable reduction in energy and power consumption levels due to the reduced time durations over which the RF transceivers are active. Namely, the adaptive HJ scheme here delivers 98.9%, 67.2% and 12.5 % enhanced energy efficiencies than the exhaustive, iterative and subarrays (single-sided) search methods, respectively.
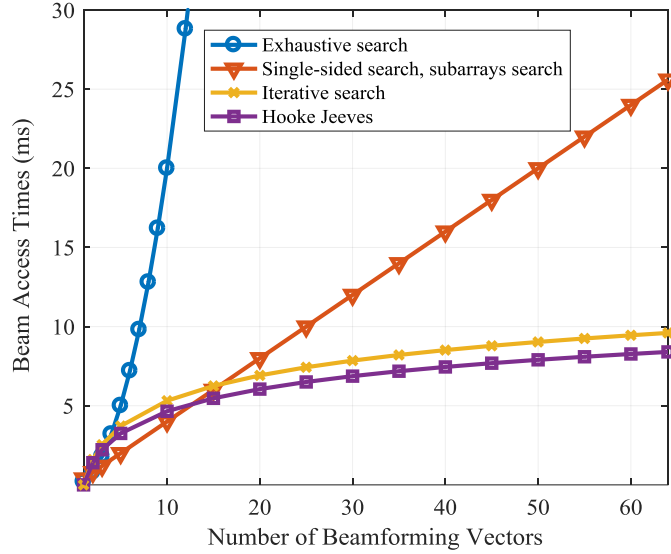
Figure 3.22: HJ energy consumption for different beamforming vectors

Some general observations are also noted here. Foremost, the findings across all the proposed schemes (NM, LJ, DC-TS, CGPS, and adaptive HJ) indicate that existing single-sided and subarrays schemes yield slightly lower access times when using limited number of beamforming vectors, i.e., less than 10. However these settings are largely infeasible in mmWave systems. In particular, the array gain generated from a small number of antennas is generally insufficient to compensate for high path loss (e.g., 130 dB) and noise power. Therefore, the received signal will be in permanent outage mode and no communication will be established. However, as the number of beamforming vectors increases, the single-sided search performance degrades significantly, whereas the proposed schemes in this chapter still yield reasonable access times in the 5-8 ms range (with 20-64 beams).

Overall, various direct pattern search schemes are proposed here for LoS and NLoS environments. Although these schemes feature approximate complexity and access times levels, their efficiency can differ based upon the channel rank, transmission bandwidth, fading class, and sparsity levels. Namely, the NM method is highly applicable for low-rank channels, i.e., since the procedure here applies vertex concept in search for a single-ray search at a distantly

located directions. Meanwhile, the LJ and DC-TS schemes perform much effectively in flat fading channels with long coherence times, i.e., due to the bisectional and Tabu search behavior. Furthermore, the CGPS scheme can be applied for wideband communications of dispersive and frequency-selective fading channels. Finally, the proposed adaptive HJ method is most applicable for low-sparsity levels with increased number of clusters, thereby it yields the highest computational complexity among the proposed schemes.

Chapter 4

Initial Beam Access Schemes: Beamforming Solutions

All of the proposed access schemes in Chapter 3 leverage analog beamforming techniques to improve power efficiency. However single beam transmission is a key limitation of any analog approach. Namely, codebook designs here only use the main lobes for beam access procedures, and this can result in prolonged beamforming scan cycle and access times. Hence in order to improve upon these designs, this chapter proposes additional multi-beam analog beamforming schemes. In particular, these methods can provide enhanced directivity, improved received signal levels, and higher detection probabilities. Furthermore, multi-beam access also gives reduced access times as compared to the proposed schemes in Chapter 3.

This chapter is organized as follows. Foremost, a novel approach is proposed, leveraging sidelobe information as an auxiliary factor to identify location of the best beam (main lobe) direction. Next, a new instantaneous analog beam scanning scheme is presented using beam coding and grating lobes to increase number of radiated beams from the same RF chain. Finally, a novel DC access scheme is introduced using instantaneous dual-beam scanning. Detailed performance results are also presented to gauge the efficiencies of the proposed multi-beam access schemes.

4.1   Sidelobe Exploitation for Beam Access

In general, sidelobe emissions are considered as deleterious due to their harmful effects on interference and secrecy. Although array tapering and binomial array designs can be utilized

to minimize such radiations, these schemes actually end up widening the main lobe. In turn this further compromises pencil beams requirements in mmWave systems. To address these concerns, a novel beam access scheme is presented here to leverage the presence of sidelobes and improve main beam direction discovery, albeit solely for LoS settings. Namely, sidelobes are exploited to determine the spatial direction returning the highest signal in order to reduce computational complexity and discovery times. Note that the sidelobes associated with the main lobe of the *signal of interest* (SoI) can be distinguished using beam coding (e.g., Walsh codes). Although sidelobe signal levels present detection challenges, the power intensity in the first SLL generally exceeds receiver sensitivity in most LoS scenarios. Hence the proposed approach is very feasible in mmWave systems operating with high receiver sensibility [65]. The detailed array model and codebook structure are now presented, followed by the beam access scheme and its associated performance results.

4.1.1 Array Model

Consider a single BS and MS pair operating in a LoS outdoor setting. It is assumed that both sides are equipped with an analog beamformer composed of two back-to-back cascaded ULA, where each array scans the $[0, \pi]$ angular space. Now in practice beam-broadening effects should be taken into consideration here, yielding a feasible angular space of $[\alpha_b, \pi\text{-}\alpha_b]$, where α_b is the beam-broadening factor. Now the array response vector for this beamformer at the MS for codebook stage y, A_{MS}^y is also given by Eq. (3.1), and similarly for the BS. Furthermore, the beamwidth for each array is given by Eq. (3.2)-(3.3), and the array gain at the MS is given by $G_{MS} = A_{MS}^y + G_a$. Additionally, the sidelobe gain at the MS is given by:

$$G_{SL}^{MS} = 20\log_{10}\left[\left|\sin(\pi(2q_{sl}+1)/2)/\sin(\pi(2q_{sl}+1)/2N_{MS}^y)\right|/N_{MS}^y\right], \tag{4.1}$$

where $q_{sl} = 1, 2, \ldots, Q_{sl}$ is the sidelobe level order.

4.1.2 Codebook Structure

Now consider the multi-resolution codebook proposed in Section 3.1.1. A sample codebook design with visible sidelobes structure is shown for Stages I and II in Figures 4.1 (a) and (b), respectively, where the sidelobes start to appear at $N_{MS}^y > 2$. Hence the sidelobe direction at the MS (and similarly at the BS) is given by $\theta_s^{MS} = (\Theta_\eta^{MS} + \Theta_{\eta+1}^{MS})/2$, where Θ_η^{MS} is the η-th null direction ($\eta = 1, 2, ..., N$) for each array given by [66]:

$$\Theta_\eta^{MS} = \begin{cases} \cos^{-1}\left[\dfrac{\lambda}{2\pi d}(-\beta_{MS} \pm \dfrac{2\eta\pi}{N_{MS}^y}) \right], \eta \neq N_{MS}^y, \; for \; 0 < \theta_0^{MS} \leq \pi, \\ \cos^{-1}\left[1 - \dfrac{\eta\lambda}{N_{MS}^y d} \right], \; for \; \theta_0^{MS} = 0, \pi. \end{cases} \tag{4.2}$$

(a) Codebook Stage I   (b) Codebook Stage II
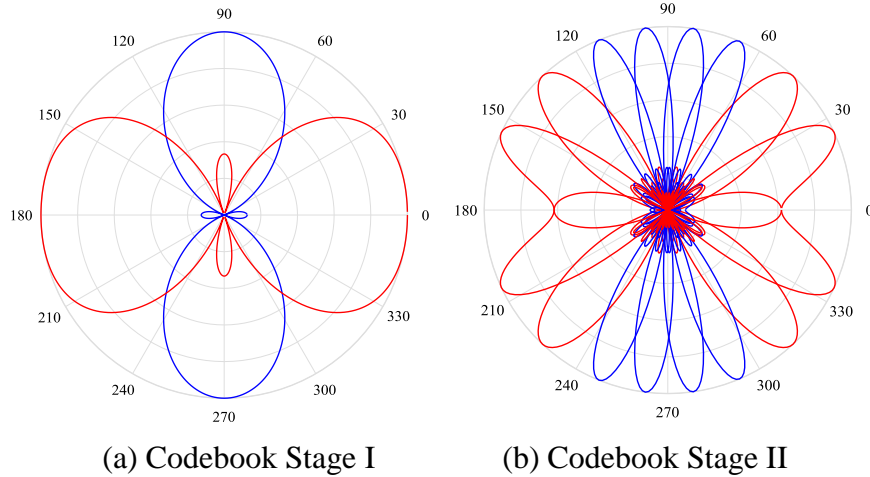
Figure 4.1: Sidelobes codebook structure with $Y = 2$ and $B = 4$

Furthermore, the spatial distance between the observation angle (θ_0^{MS}) and sidelobe direction (θ_s^{MS}) at the MS can be expressed as:

$$\Delta\Theta = \theta_0^{MS} - \theta_s^{MS} = \dfrac{\phi_\eta}{2} + \left| \dfrac{\Theta_1^{MS} - \Theta_2^{MS}}{2} \right|, \tag{4.3}$$

where ϕ_η is the *first null beamwidth* (FNBW) given by [74]:

$$\phi_\eta = \begin{cases} \left| 2\cos^{-1}\left[1 - \dfrac{\lambda}{N_{MS}^y d}\right] \right| for \ \theta_0^{MS}=0, \ \pi, \\ \left| 2\left[\dfrac{\pi}{2} - \cos^{-1}\left(\dfrac{\lambda}{N_{MS}^y d}\right)\right] \right| for \ 0 < \theta_0^{MS} \leq \pi. \end{cases}$$ (4.4)

Meanwhile the received baseband downlink signal is still given by Eq. (3.4) for a LoS channel gain given by Eq. (3.5).

4.1.3 Sidelobe Beam Access Procedure

Akin to the earlier beam access problem formulation in Section 3.2, again the beamforming and combining vectors (u_l and v_l) are represented by r_i and s_j beam indices, respectively, i, j=1, 2,.., B. Likewise, the objective function is still given by the received signal power level, $\acute{y}_l(r_i, s_j)$, and the overall goal is to find the best beam index pair P_k for the given search grid, i.e., Eq. (3.9). Now analog beam scanning always yields in a unique beam index pair returning highest signal level. However spatial leakage can occur when a sidelobe falls at the effective aperture of an array, i.e., when different beam indices are tested and main lobes are misaligned. Hence four possible signal combinations can result from the orientation of array-radiated lobes, as shown in Figure 4.2:

(a) Main lobe-to-main lobe, $\acute{y}_{MM}$ (b) Sidelobe-to-main lobe, $\acute{y}_{SM}$

(c) Sidelobe-to-sidelobe, $\acute{y}_{SS}$ (d) null reception, $\acute{y}_\eta$
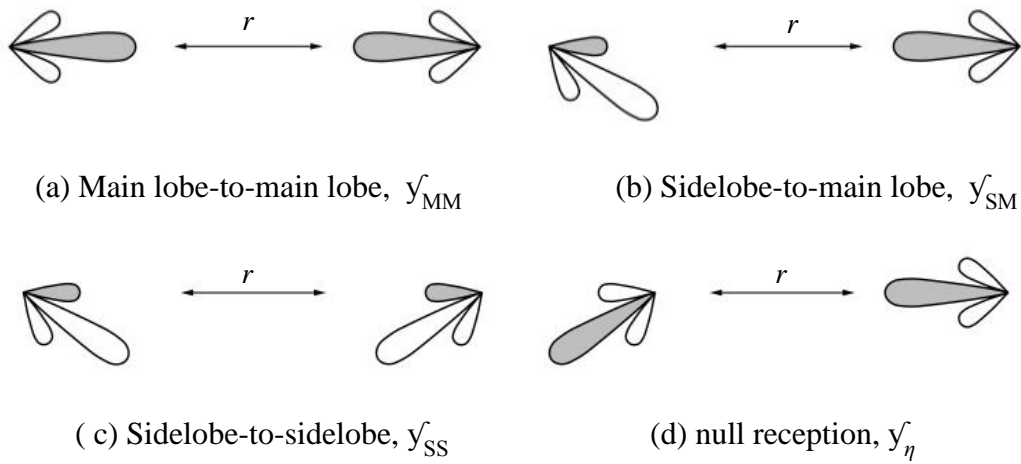
Figure 4.2: Spatial lobe orientations

- *Main lobe-to-main lobe* (MM) with signal level $\check{y}_{\mathrm{MM}}$, per Figure 4.2 (a)

- *Sidelobe-to-main lobe* (SM) with signal level $\check{y}_{\mathrm{SM}}$, per Figure 4.2 (b)

- *Sidelobe-to-sidelobe* (SS) with signal level $\check{y}_{\mathrm{SS}}$ ($\check{y}_{\mathrm{SS}} > \check{y}_{\mathrm{th}}$), per Figure 4.2 (c)

- Null reception with signal level $\check{y}_\eta$ ($\check{y}_\eta < \check{y}_{\mathrm{th}}$), per Figure 4.2 (d)

Of these, the MM signal gives maximum beamforming gain. Further details are now presented.

Overall, a SoI with low-power level (i.e., below Shannon capacity) detected during beam scanning can be used to estimate the location of the highest signal. Namely, the sequence of subsequent directional scans is adapted based upon the observed signal level in the instantaneous scan direction, i.e., θ_0^{MS} is rotated by $\Delta\Theta$ towards the detected signal. This rotation corresponds to the sidelobe or null locations where signals were originally observed, i.e., since the θ_s^{MS} and θ_0^{MS} directions are always adjacent and equally-spaced in ULAs. Consequently, this procedure can rapidly detect the highest signal levels and also allows for earlier termination of beam scanning, i.e., no exhaustive search. In turn, vital time-frequency resources are freed up earlier for subsequent data-plane transmission. Furthermore, this formulation also assumes a memoryless probability for the global maximum detection for each beam pair $\mathbb{P}_k(\mathrm{r_i}, \mathrm{s_j})$, i.e., as given by:

$$\mathbb{P}_1\left[\check{y}_l \geq \check{y}_{\mathrm{MM}}\right] = (\Omega_{\mathrm{SL}}^{\mathrm{MS}}\Omega_{\mathrm{SL}}^{\mathrm{BS}})/B^2, \tag{4.5}$$

where $\Omega_{\mathrm{ML}}^{\mathrm{MS}}$ and $\Omega_{\mathrm{ML}}^{\mathrm{BS}}$ are the number of main lobes at the MS and BS, respectively. Also, the probability of an event $\check{C}$ successfully detecting a high signal ($\check{y}_l \geq \check{y}_{\mathrm{MM}}$) at $\mathbb{P}_k(\mathrm{r_i}, \mathrm{s_j})$ after i trials with F previous failures ($\check{y}_l < \check{y}_{\mathrm{MM}}$) is given by:

$$\mathbb{P}(\check{C}\,|\,F) = \frac{\mathbb{P}(\check{C}\cap F)}{\mathbb{P}(F)} = \frac{\mathbb{P}(\check{C})\mathbb{P}(F)}{\mathbb{P}(F)} = \frac{1}{B^2 - (i-1)}, \ i = 1, 2.., k. \tag{4.6}$$

Furthermore, the detection probabilities for the SM, SS and null signals are given by:

84

$$\mathbb{P}_2\left[y_l' = y_{SM}'\right] = (\Omega_{SL}^{MS}\Omega_{ML}^{BS} + \Omega_{SL}^{BS}\Omega_{ML}^{MS})/B^2, \tag{4.7}$$

$$\mathbb{P}_3\left[y_l' = y_{SS}'\right] = (\Omega_{SL}^{MS}\Omega_{SL}^{BS})/B^2, \tag{4.8}$$

$$\mathbb{P}_4\left[y_l' = y_{\eta}'\right] = \mathbb{P}_4\left[y_l' < y_{SS}'\right] = 1 - \mathbb{P}_1 - \mathbb{P}_2 - \mathbb{P}_3 \tag{4.9}$$

$$= (B^2 - (\Omega_{SL}^{MS}\Omega_{ML}^{BS} + \Omega_{SL}^{BS}\Omega_{ML}^{MS}) - \Omega_{SL}^{MS}\Omega_{SL}^{BS} - 1)/B^2,$$

respectively, where $\Omega_{SL}^{MS} = 2\Omega_{ML}^{MS}$ and $\Omega_{SL}^{BS} = 2\Omega_{ML}^{BS}$ are the numbers of the *first sidelobe levels* (FSLL) in the MS and BS scans, respectively, associated with Ω_{ML}^{MS} and Ω_{ML}^{BS} main lobes at the MS and BS, respectively.

The sidelobe-based beam access algorithm is presented in Figure 4.3. This solution assumes that the MS and BS are separated by a distance of r and start the beam scanning process by choosing a random initial beam direction (r_i, s_j) from the directions defined in codebook Stage I ($y = 1$). Hence the MS and BS initial directions correspond to the initial beam index pair $\mathbb{P}_1(r_i, s_j)$ in the search grid, and the received signal observed at this random initial beam index pair is given by $y_l'(\mathbb{P}_1(r_i, s_j))$. Along these lines, Figures 4.4 (a)-(b) depict the received signal profile for two codebook stages at different lobe orientations. Note that the highest signal level here is observed at 80 dBm and 72 dBm for codebook stages I and II, respectively.

First of all, if the initial signal is sufficiently strong and exceeds Shannon link capacity requirements, then the main lobe-to-main lobe signal has been observed, i.e., $y_l'(\mathbb{P}_1(r_i, s_j)) \geq y_{MM}'$. Consequently, the signal level $y_l'(\mathbb{P}_1(r_i, s_j))$ here is compared with the received values at the neighboring beams which may potentially include additional SoI with different power levels, i.e., to determine whether the highest signal has been detected. Specifically, four perturbed index pairs are derived here, i.e., $\mathbb{P}_1^a = (r_{i+\delta}, s_j)$, $\mathbb{P}_1^b = (r_{i-\delta}, s_j)$, $\mathbb{P}_1^c = (r_i, s_{j+\delta})$, and $\mathbb{P}_1^d = (r_i, s_{j-\delta})$, where δ is the grid step size that specifics the spatial distance,

$\Delta\Theta$. The respective received power levels at these pairs are denoted as $\hat{y}_l(\mathcal{P}_1^a)$, $\hat{y}_l(\mathcal{P}_1^b)$, $\hat{y}_l(\mathcal{P}_1^c)$, and $\hat{y}_l(\mathcal{P}_1^d)$. Using these values, the beam index with the highest received signal is selected for additional refinement in the successive codebook stage, i.e., $(r_i,\ s_j)_{bst_y}$.


```
Inputs: δ, r₀
For y = 1, y ≤ Y, ∀ 𝒫(rᵢ, sⱼ) ∈ R
      𝒫₁ = (rᵢ, sⱼ), ŷₗ(𝒫₁)  // Random initial beam indices
  If  ŷₗ(𝒫ᵢ) ≥ ŷ_MM  // Main lobe-to-main lobe (MM)
      𝒫₁ᵃ,ᵇ = (rᵢ±δ, sⱼ), 𝒫₁ᶜ,ᵈ = (rᵢ, sⱼ±δ), ŷₗ(𝒫₁ᵃ), ŷₗ(𝒫₁ᵇ), ŷₗ(𝒫₁ᶜ), ŷₗ(𝒫₁ᵈ)
      (rᵢ, sⱼ)_bstᵧ ← max ŷₗ{𝒫₁,𝒫₁ᵃ,𝒫₁ᵇ,𝒫₁ᶜ,𝒫₁ᵈ}, y ← y + 1 // Terminate codebook stage
  Else If  ŷ_SM ≤ ŷₗ(𝒫₁) < ŷ_MM  // Sidelobe-to-main lobe (SM)
          r̄ᵢ = rᵢ±δ, ŷₗ(r̄ᵢ, sⱼ), (rᵢ, sⱼ)_bstᵧ ← max ŷₗ(𝒫(r̄ᵢ, sⱼ)),  y ← y + 1
  Else If  ŷ_ss ≤ ŷₗ(𝒫₁) < ŷ_SM  // Sidelobe-to-sidelobe (SS)
          𝒫ₙᵣᵃ,ᵇ(rᵢ₊δ, sⱼ±δ), 𝒫ₙᵣᶜ,ᵈ(rᵢ₋δ, sⱼ±δ), ŷₗ{𝒫ₙᵣᵃ,ᵇ,𝒫ₙᵣᶜ,ᵈ},
          (rᵢ, sⱼ)_bstᵧ ← max ŷₗ{𝒫ₙᵣᵃ,ᵇ,𝒫ₙᵣᶜ,ᵈ},  y ← y + 1 // Terminate codebook stage
  Else If  ŷₗ(𝒫₁) < ŷ_ss  // Locations at nulls
          𝒫_rad = (rᵢ₋δ, sⱼ₋δ), ŷₗ(𝒫_rad)  // Do radial perturbation
          If  ŷₗ(𝒫_rad) ≥ ŷ_ss,  𝒫₁ ← 𝒫_rad, ŷₗ(𝒫₁)  // Restart 𝒫₁ test
          Else 𝒫_dw = (rᵢ, sⱼ₋δ), ŷₗ(𝒫_dw)  // Downward perturbation
              If  ŷₗ(𝒫_dw) ≥ ŷ_ss, 𝒫₁ ← 𝒫_dw, ŷₗ(𝒫₁) // Restart 𝒫₁ test
              Else 𝒫_sd = (rᵢ₋δ, sⱼ), ŷₗ(𝒫_sd) // Do side perturbation
                  𝒫₁ ← 𝒫_sd, ŷₗ(𝒫₁)  // Restart 𝒫₁ test
              End If
          End If
  End If
End For
```

Figure 4.3: Sidelobe exploitation for initial beam access

Meanwhile, a sidelobe-to-main lobe (SM) signal level is received if $\hat{y}_{SM} \le \hat{y}_l(\mathcal{P}_1(r_i,\ s_j))$ $< \hat{y}_{MM}$, Figure 4.2(b). Hence the (MS or BS) node receiving the signal at the location of the main lobe stops scanning for τ_β^{BS} seconds (assuming BS). Meanwhile, the other side (MS) rotates its main lobe towards the location of the sidelobe where the signal was observed and measures the signal level after rotation, $\hat{y}_l(\mathcal{P}(\bar{r}_i, s_j))$, $\bar{r}_i = r_{i\pm\delta}$. Furthermore, if $\hat{y}_{SM} > \hat{y}_l(\mathcal{P}_1) \ge \hat{y}_{ss}$, then the sidelobe-to-sidelobe (SS) orientation has been observed. Hence two neighboring perturbations, i.e., $\mathcal{P}_{nr}^{a,b}$ and $\mathcal{P}_{nr}^{c,d}$, are tested here at which the MS and BS jointly rotate the direction of their

main lobes towards the direction of the detected signal (location of the sidelobe). The first sidelobes level adjacent to the main lobes are then tested, namely $\check{y}_l\{\mathcal{P}_{nr}^{a,b}, \mathcal{P}_{nr}^{c,d}\}$, $\mathcal{P}_{nr}^{a,b}=(r_{i+\delta}, s_{j\pm\delta})$, $\mathcal{P}_{nr}^{c,d} = (r_{i-\delta}, s_{j\pm\delta})$.

(a) Codebook Stage I   (b) Codebook Stage II
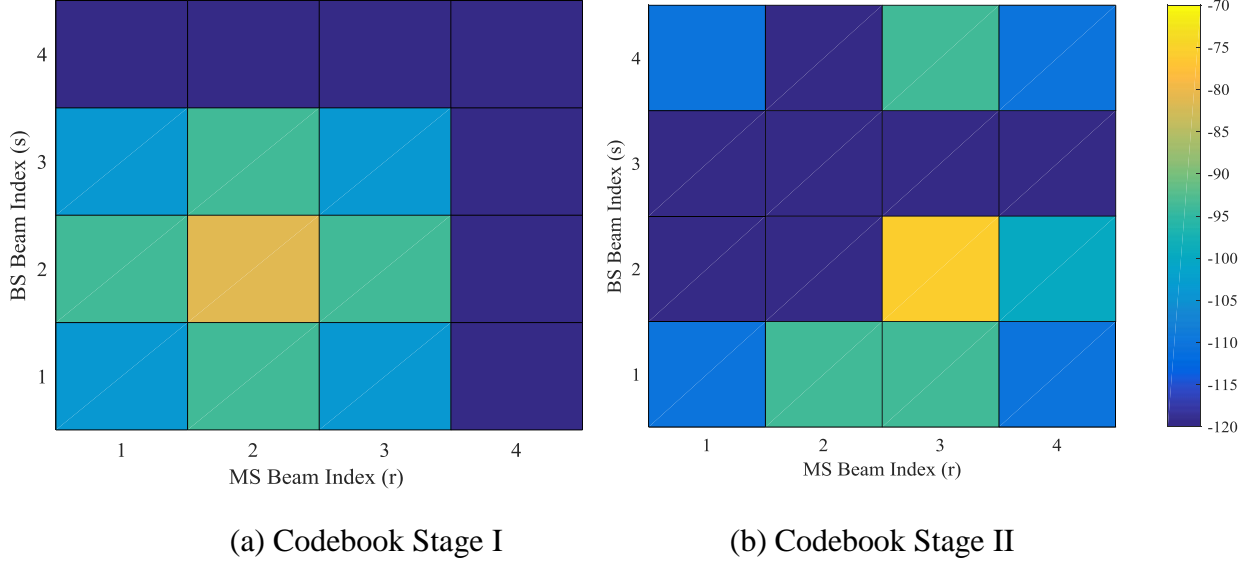
Figure 4.4: Sidelobe received signal levels for codebook Stages I and II

Finally, if $\check{y}_l(\mathcal{P}_1) < \check{y}_{SS}$, then the null region case has been detected, i.e., the main lobe or sidelobe point towards the nulls, $\check{y}_l(\mathcal{P}_1) = \check{y}_\eta$. Hence both the MS and BS change their beam indices (pointing directions) by the spatial distance, $\Delta\Theta$, in a radial manner, $\mathcal{P}_{rad} = (r_{i-\delta}, s_{j-\delta})$. Now if $\check{y}_l(\mathcal{P}_{rad}) < \check{y}_{ss}$, then the downward perturbation is tested, i.e., $\mathcal{P}_{dw} = (r_i, s_{j-\delta})$. Namely, only the BS (or MS) changes its direction (index), whereas the remote MS (or BS) maintains its current direction by delaying its scan cycle by τ_β^{MS}, i.e., dwell time for single progressive phase shift. Alternatively, if $\check{y}_l(\mathcal{P}_{dw}) < \check{y}_{ss}$, a final sideways perturbation is checked, i.e., $\mathcal{P}_{sd} = (r_{i-\delta}, s_j)$.

Table 4.1: System settings for sidelobe exploitation scheme

Category	Parameters	Value
System	f_c (GHz), bandwidth (MHz)	38, 100
Signal level (dBm)	y_{th}, y_{SS}, y_{SM}, y_{MM}	-120, -113, -95, -82
Channel	ζ, l, h_l, σ^2, r_0(m), r (m)	2, 1, 1, 1, 5, 350
ULA, Codebook	P_{tr} (dBm), G_a, N_{MS}^1, N_{MS}^2, N_{MS}^T, a_n, C, Q, Y, B_T^1, B_T^2, Ω_{ML}^{MS}, Ω_{SL}^{MS}, Ω_{ML}^{BS}, Ω_{SL}^{BS}	30, 3, 3, 7, 20, 1, 1, 1, 2, 4, 16, 1, 2, 1, 2
Time (μs), step size	t_{PSS}, τ_β^{MS}, τ_β^{BS}, δ	200, 200, 200, 1

4.1.4 Performance Evaluation of Sidelobe Access Scheme

The sidelobe-based access scheme is now evaluated for a single stationary BS-MS pair in a LoS environment. The related system parameters are listed in Table 4.1, and several performance metrics are evaluated. First, the computational complexity of this scheme is derived based upon the number of worst case measurements (for null reception, $y_l = y_\eta$) as follows:

$$S = S(\mathbb{P}_1) + S_\eta + S_{SS} \vee S_{SM} \vee S_{MM}, \quad S_\eta = S(\mathbb{P}_{rad}) + S(\mathbb{P}_{dw}) + S(\mathbb{P}_{sd}), \tag{4.10}$$

$$S_{MM} = S_{SS} = S(\mathbb{P}_{nr}^{a,\,b}) + S(\mathbb{P}_{nr}^{c,\,d}), \quad S_{SM} = S(\mathbb{P}(\bar{r}_i, s_j)),$$

where S_η, S_{SS}, S_{SM}, and S_{MM} are the processing step counts when receiving null, SS, SM and MM signal levels, respectively, with computational complexity scaled by $O(S \log_4(B^2))$.

The resultant complexity of the proposed solution is plotted in Figure 4.5 alongside that of existing schemes (as per Chapter 3). Overall these results confirm that the sidelobe-based scheme gives significant improvements here, i.e., 50% lower complexity than the iterative and single-sided schemes, 62.5% lower than the GPS search and 93.75% lower than the exhaustive search for 16 beams. These improvements also hold for larger beam sizes (results not shown).
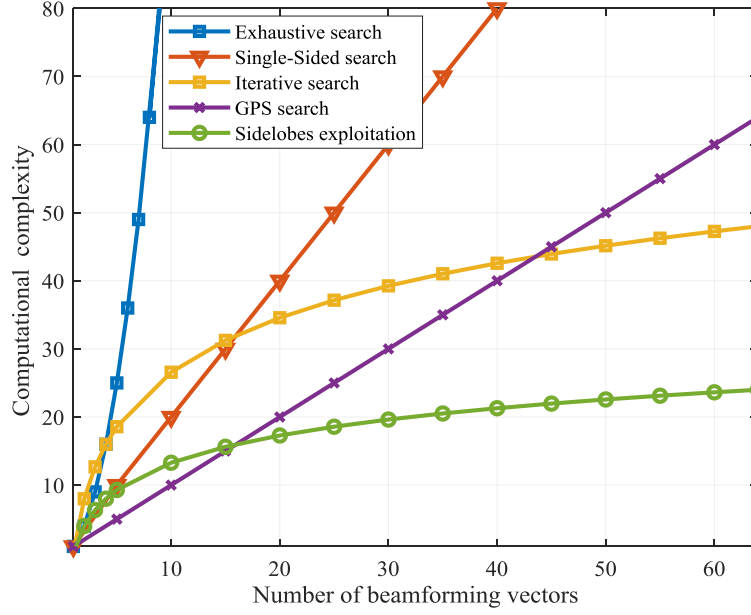
Figure 4.5: Computational complexity for the sidelobe exploitation scheme

Meanwhile, the access time, τ_d, is also plotted in Figure 4.6. This value is derived by computing the beamforming scan cycle time during which the PSS signal is periodically transmitted on each beamforming vector, i.e., $\tau_d = \tau_\beta^{MS}(P_{dw}) + \tau_\beta^{BS}(P_{sd}) + t_{PSS}/C$, where $\tau_\beta^{MS}(P_{dw})$, $\tau_\beta^{BS}(P_{sd})$, C, and t_{PSS} are the dwell times during the downward and sideways perturbations at the MS and BS, the number of RF chains, and the PSS duration, respectively. Again, the sidelobe-based scheme vastly outperforms all other methods here, particularly if there are a larger number of beams ($B = 64$), i.e., 44%, 48%, 60%, and 99.4% faster than the iterative, single sided, GPS, and exhaustive schemes respectively.
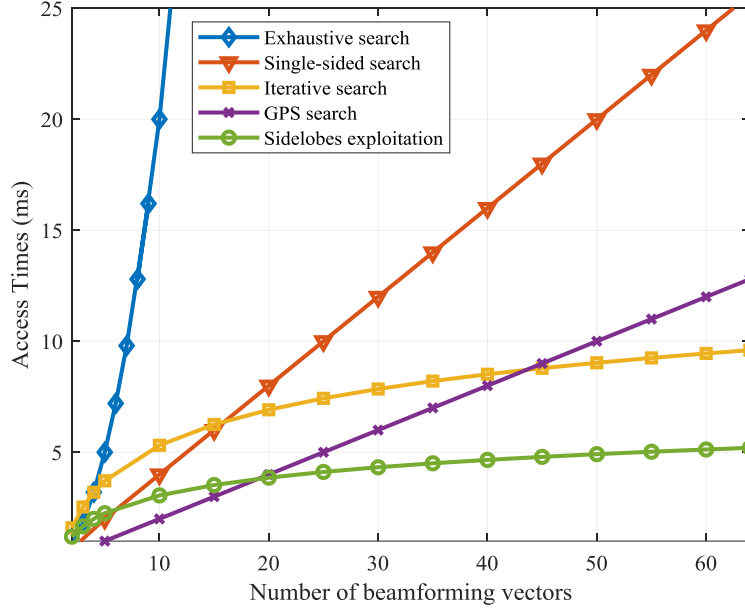
Figure 4.6: Sidelobe beam access times for different schemes

Finally, the outage probability is also gauged for random (uniformly-distributed) range values between $r_{\min}$ and $r_{\max}$. Specifically, this value is computed for the SS configuration as follows:

$$\mathbb{P}[y_l \leq y_{SS}] = \mathbb{P}\left[\frac{P_t G_{SL}^{MS} G_{SL}^{BS} |h_l|^2 16\pi^2 \lambda^2}{r^2} \leq y_{SS}\right] = \mathbb{P}\left[\sqrt{\frac{P_t G_{SL}^{MS} G_{SL}^{BS} |h_l|^2 16\pi^2 \lambda^2}{y_{SS}}} \leq r\right]$$

$$= \int_{\frac{P_t G_{SL} G_{SL} |h_l|^2 16\pi^2 \lambda^2}{y_{SS}}}^{r_{\max}^2} \frac{1}{2\sqrt{x}(r_{\max}-r_{\min})} dx, = \frac{1}{(r_{\max}-r_{\min})}\left[r_{\max} - \sqrt{\frac{P_t G_{SL}^{MS} G_{SL}^{BS} |h_l|^2 16\pi^2 \lambda^2}{y_{SS}}}\right] = \frac{r_{\max}-r_{out}}{(r_{\max}-r_{\min})}, \ x = r^2 \quad (4.11)$$

where r_{out} is the outage distance (meters) and G_{SL}^{MS} and G_{SL}^{BS} are sidelobe gains at the MS and BS, respectively (similar expressions can also be derived for other configurations). These probabilities are plotted in Figure 4.7 and indicate outages at 350 m and 450 m for codebook Stages I and II, respectively. A SM outage is also seen at 650 m and 750 m for Stages I and II, respectively. These results confirm that the proposed algorithm has very favorable detectable

ranges for LoS links. In particular, SS signals can be detected at longer distances up to 350m, making the proposed algorithm more reliable for larger LoS environments.
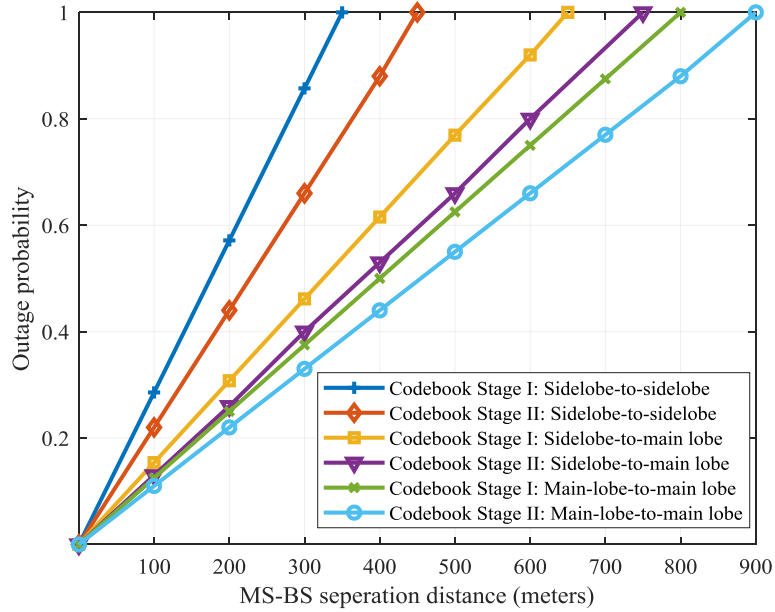
Figure 4.7: Outage probabilities for the different lobe configurations

4.2 Simultaneous Multi-Beam Initial Access

Another novel fast access scheme is also developed using multi-beam beamforming (along with grating lobes and beam coding). This upgraded beamformer design, termed as simultaneous *multi-beam analog beamforming* (MB-ABF), eliminates the gain and directivity deficiencies associated with wide beams in hierarchical codebooks. As a result, this approach is analogous to digital and hybrid beamforming as it provides spatial diversity at the expense of lower channel capacity. However, the MB-ABF scheme simultaneously generates multiple beams for the same input power, i.e., versus sequentially for the *single-beam analog beamforming* (SB-ABF) approach in Chapter 3.

Now antenna spacing is a key criterion in array design for any beamforming architecture. Specifically, smaller spacing (dense array) gives a host of concerns, e.g., such as mutual coupling, reduced directivity, pattern blindness and spatial under-sampling. Meanwhile larger

91

spacing (sparse array) generates grating lobes and also reduces channel sparsity, and also increases cluster richness. Since the antenna spacing here exceeds the coherence distance, distinct received angle of arrivals can also be resolved at adjacent antennas. In turn, this property leads to space-selective channels.

Based upon the above, the proposed MB-ABF access scheme deliberately generates grating lobes in simultaneous multi-beam arrays. Unique orthogonal codes are then assigned to each simultaneous beam and its affiliated grating lobe, i.e., in order to resolve spatial beam signatures and mitigate interference effects. Furthermore, narrow beams are also generated to simultaneously overlay the entire spatial domain. Therefore this overall solution mitigates the requirement for exhaustive beam spatial scanning using low-resolution codebook structures. However carefully note that some minimal refinement scanning is still required in limited directions.

The system model is now presented, including the design aspects for simultaneous beam, grating lobes and beam coding. The proposed access scheme is then detailed, followed by some detailed performance analysis results.

4.2.1 Simultaneous Multi-Beam Analog Beamformer

Consider two back-to-back linear arrays p and q, where each array is composed of N_T^p and N_T^q total antenna elements. The η_s^p and η_s^q adjacent antennas in p and q, respectively, are further combined into s sections, $s = 1, 2, \ldots, S$, where $\eta_s^p \subseteq N_T^p \in Z$, $\eta_s^q \subseteq N_T^q \in Z$, $N_T^p = S\eta_s^p$, and $N_T^q = S\eta_s^q$. Both arrays are also connected to a single RF chain to generate the simultaneous MB-ABF with $N_T \in Z$ total antenna elements, i.e., $N_T = N_T^p + N_T^q$, where the signal at the output of the RF chain is split and fed into S multiple sections. Furthermore, the weighting vectors of these sections are also adjusted to constructively add the antenna patterns of each section. Hence the

92

overall output from array p and q is a single primary beam which is radiated from each section s, i.e., $\Theta_s^p \in [0, \pi]$ and $\Theta_s^q \in [0, \pi]$ respectively. Note that the number of simultaneous beams is equal to the number of sections here. Consequently, the resultant array output consists of a total of B_T non-overlapping and independent simultaneous primary beams propagating in different directions, $B_T \in [0, 2\pi]$. The overall response vector for this MB-ABF at the MS can also be expressed by the periodic array factor for arrays p and q as follows:

$$
\begin{aligned}
\boldsymbol{U}_{MS} = & \frac{1}{N_T^p} \left[\sum_{n=1}^{\eta_1^p} a_n \exp(-jk_v d_n \cos\Theta_1^p), \sum_{\eta_1^p+1}^{\eta_2^p} a_n \exp(-jk_v d_n \cos\Theta_2^p), \dots \right. \\
& \left. \sum_{\eta_{S-1}^p}^{\eta_T^p} a_n \exp(-jk_v d_n \cos\Theta_S^p) \right]^T \\
& + \frac{1}{N_T^q} \left[\sum_{n=1}^{\eta_1^q} a_n \exp(-jk_v d_n \cos\Theta_1^q), \sum_{\eta_1^p+1}^{\eta_2^q} a_n \exp(-jk_v d_n \cos\Theta_2^q), \dots \right. \\
& \left. \sum_{\eta_{S-1}^p}^{\eta_T^q} a_n \exp(-jk_v d_n \cos\Theta_S^q) \right]^T,
\end{aligned}
\tag{4.12}
$$

Furthermore, the pointing direction for each beam at p (and similarly at q) is given by:

$$
\Theta_s^p = \cos^{-1}\left[\frac{-\beta_p \lambda}{2\pi d_n} \right],
\tag{4.13}
$$

where β_p is the progressive phase shift between the elements in p. Furthermore, the HPBW for each pointing beam Θ_s^p at array p (and similarly at array q) is given by:

$$
\phi_s^p = \begin{cases} \cos^{-1}(\lambda/2\pi d_n (k_v d_n \cos\Theta_s^p \pm 2.782/\eta_s^p)), \, for \; 0<\Theta_s^p<\pi, \\ 2\cos^{-1}(1-1.391\lambda/\eta_s^p d_n), \, for \; \Theta_s^p = 0, \pi. \end{cases}
\tag{4.14}
$$

As mentioned earlier, the simultaneous MB-ABF design implements a form of redundant transmit diversity, i.e., where each primary beam is maintained during the entire control signaling duration. This scheme contrasts with a typical SB-ABF design which conducts limited sequential scanning in TDM mode. For example, Figure 4.8 shows a case with 32 (sections) simultaneous adjacent primary beams. Furthermore, in order to establish full spatial coverage

93

during beam access, the remnant spatial nulls are also overlaid with grating lobes. Specifically, each primary beam Θ_s^p and Θ_s^q at arrays p and q, respectively, has g_s total grating lobes, i.e., $g_s = d_n/\lambda$ at Θ_g^p and Θ_g^q pointing directions.
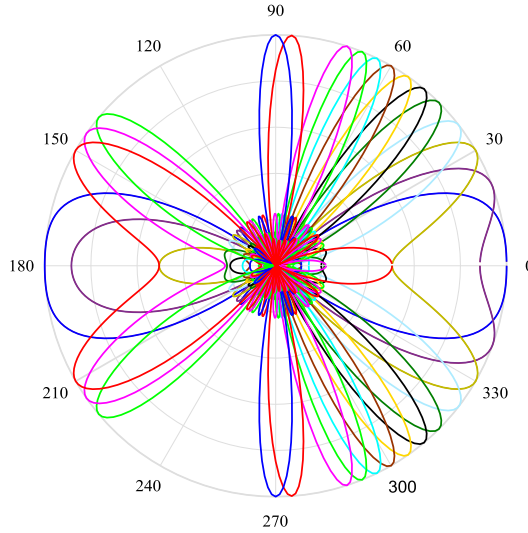
Figure 4.8: Simultaneous multi-beam transmission

4.2.2 Grating Lobes Generation

In general the wider beams (used in the initial scanning stage of cascaded codebook designs) yield poor directivity and blockage sensitivity [67]-[71]. However directivity can be significantly improved by using simultaneous beams with a spacing of $d_n = \lambda$, i.e., without increased power consumption or additional antenna elements. Namely, transmission power can now be divided between the primary beam and grating lobes (fringes) instead of concentrating it into a single wide beam. Consequently, the identical narrow beams (spatial images) generated here have higher directivity and transmit diversity. Also, this antenna spacing further increases scattering intensity and reduces sparsity levels for mmWave channels. Carefully note that a value of $d_n = \lambda$ also increases the visible region proportionally. Hence this region exceeds the Nyquist interval, and the grating lobes have the same magnitude as the primary beam, i.e., $-k_v d_n \leq (\varphi_{\text{vis}}^p, \varphi_{\text{vis}}^q) \leq k_v d_n$, where $\varphi_{\text{vis}}^p = k_v d_n cos\Theta_s^p + \beta_p$ and $\varphi_{\text{vis}}^q = k_v d_n cos\Theta_s^q + \beta_q$ at arrays p

94

and q, respectively. Furthermore the total number of grating lobes, G_T, in the radiation pattern of the proposed MB-ABF is now proportional to d_n, i.e., equal to the number of complete Nyquist intervals falling within the width of the visible region;

$$G_T = \frac{d_n(2S)}{\lambda} = g_p + g_q,\qquad(4.15)$$

where g_p and g_q denote the number of grating lobes in arrays p and q, respectively. For example, Figure 4.9 shows a sample radiation pattern for a MB-ABF composed of simultaneous primary beams and grating lobes, i.e., to be utilized for beam access as detailed later.
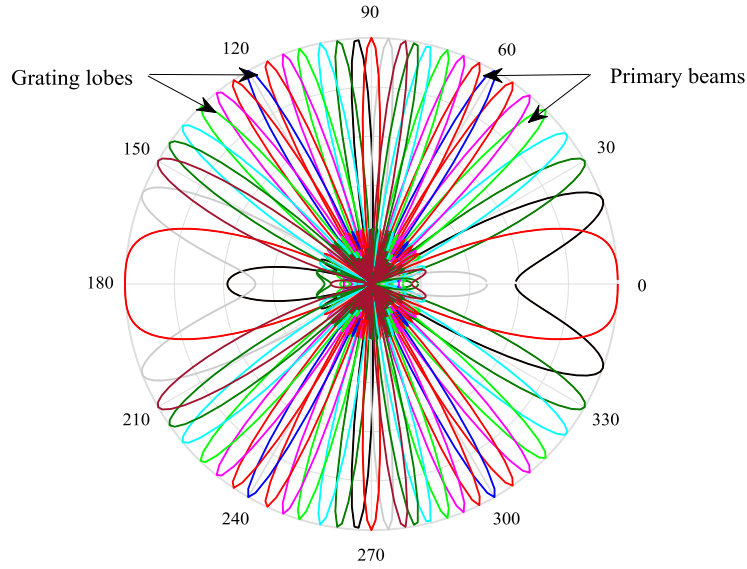
Figure 4.9: Simultaneous multi-beam with grating lobes

Note that the periodic locations of these grating lobes, Θ_g^p and Θ_g^q, can be also specified as a function of the simultaneous primary beam directions Θ_s^p and Θ_s^q as [72],[73]:

$$\Theta_g^p = \sin^{-1}\left[\sin\Theta_s^p \pm \frac{\lambda}{d_n}\right] \text{ and } \Theta_g^q = \sin^{-1}\left[\sin\Theta_s^q \pm \frac{\lambda}{d_n}\right].\qquad(4.16)$$

Finally, the total number of radiated beams in the MB-ABF is given by $B_T = (2S) + G_T$, whereas the radiated pointing directions at the MS are as follows (and likewise at the BS):

$$\Theta_{rad}^{\text{MS}} = \{\Theta_s^p, \ldots, \Theta_S^p, \Theta_s^q, \ldots, \Theta_S^q, \Theta_g^p, \ldots, \Theta_g^q\}. \tag{4.17}$$

4.2.3 Beam Coding

As noted earlier, orthogonal codes are also mapped onto the primary beams Θ_s^p and Θ_s^q in order to generate distinctive spatial signatures for the radiated patterns, see [74]. This step is essential since all radiated beams at the MS and BS $\left(\Theta_{rad}^{\text{MS}} \text{ and } \Theta_{rad}^{\text{BS}}\right)$ carry otherwise identical modulated signals (single RF chain). Furthermore, beam coding is also required to mitigate interference effects and extract the SoI. Overall, linear error correcting block-codes are most favorable choice here given their robust correlation properties. Hence an orthogonal extended Hamming code is used, i.e., C=$\{C^p, C^q\}$, where $C^p[e, N, d_H]$ and $C^q[e, N, d_H]$, and e is the codeword length, N is the code dimension (number of signature codeword), and d_H is the minimum Hamming distance. Some further details on the mapping process are now presented.

The linear p and q arrays are assigned C^p and C^q block-codes, respectively, where each block-code has S unique codewords (sequences), c_S^p and c_S^q, respectively. Each simultaneous primary beam (and its affiliated grating lobe) in p and q is also assigned a single unique codeword. Finally, each codeword in c_S^p and c_S^q has (in order) b_I^p and b_J^q codebits which linearly multiply the element amplitudes, a_n, in each section, where I=η_s^p=S/2, J =η_s^q = S/2. In notational form these block-codes can be written as:

$$C^P=[c_1^p, c_2^p, \ldots c_S^p]^{\text{T}} \text{ and } C^q=[c_1^q, c_2^q, \ldots c_S^q]^{\text{T}}, \tag{4.18}$$

$$c_s^p=[b_1^p, b_2^p, \ldots, b_I^p] \text{ and } c_s^q=[b_1^q, b_2^q, \ldots, b_J^q], \tag{4.19}$$

where b_I^p and b_I^q are the number of states in each codebit. Overall, the above block-codes are derived by using the $H(7,4)$ Hamming code and computing the parity check and complementary $\bar{H}$ matrix. The block-code generator matrices for C^p and C^q are also shown in Tables 4.2 and 4.3, respectively. Consider some properties here.

1) Hamming Weight

The Hamming weight is the number of codebits (symbols) that differ from negation (-1), expressed as:

$$W_H(b_I^p) \triangleq \left| \{I: b_I^p \neq -1\} \right| \tag{4.20}$$

Table 4.2: [8, 16, 4**]** Orthogonal block-code for array *p*

c_1^p=[-1 -1 -1 -1 -1 -1 -1 -1]	c_9^p=[-1 1 1 -1 -1 1 1 -1]
c_2^p=[1 -1-1 -1 1 1 1 -1]	c_{10}^p=[-1 1 -1 1 1 1 -1 -1]
c_3^p=[-11-1-1 1 -1 1 1]	c_{11}^p=[-1 -1 1 1 1 -1 1 -1]
c_4^p=[-1 -1 1 -1 1 1 -1 1]	c_{12}^p=[1 1 1 -1 1 -1 -1 -1]
c_5^p=[-1 -1 -1 1 -1 1 1 1]	c_{13}^p=[1 1 -1 1 -1 -1 1 -1]
c_6^p=[1 1 -1 -1 -1 1 -1 1]	c_{14}^p=[1 -1 1 1 -1 1 -1 -1]
c_7^p=[1 -1 1 -1 -1 -1 1 1]	c_{15}^p=[-1 1 1 1 -1 -1 -1 1]
c_8^p=[1 -1 -1 1 1 -1 -1 1]	c_{16}^p=[1 1 1 1 1 1 1 1]

Table 4.3: [8, 16, 4] Orthogonal block-code for array *q*

c_1^q=[-1 1 1 1 1 -1 -1 -1]	c_9^q=[1 -1 -1 -1 -1 1 1 1]
c_2^q=[1 -1 1 1 -1 1 -1 -1]	c_{10}^q=[-1 1 -1 -1 1 -1 1 1]
c_3^q=[1 1 -1 1 -1 -1 1 -1]	c_{11}^q=[-1 -1 1 -1 1 1 -1 1]
c_4^q=[1 1 1 -1 -1 -1 -1 1]	c_{12}^q=[-1 -1 -1 1 1 1 1 -1]
c_5^q=[-1 1 -1 1-1 1 1 -1]	c_{13}^q=[1 -1 1 -1 1 -1 -1 1]
c_6^q=[-1 1 -1 1 1 -1 -1 1]	c_{14}^q=[1 -1 1 -1 -1 1 1 -1]
c_7^q=[-1 1 1 -1 -1 1 -1 1]	c_{15}^q=[1 -1 -1 1 1 -1 1 -1]
c_8^q=[-1 1 1 -1 1 -1 1 -1]	c_{16}^q=[1 -1 -1 1 -1 1 -1 1]

2) Minimum Hamming Distance

The minimum Hamming distance, d_H , between any two successive and distinct codewords (c_s^p, c_{s+1}^p) and (c_s^q, c_{s+1}^q) at arrays *p* and *q* is expressed, respectively, as:

$$d_H(c_s^p, c_{s+1}^p) = min\{d_H(c_s^p, c_{s+1}^p) | c_s^p, c_{s+1}^p \in C^p, c_s^p \neq c_{s+1}^p\} = \sum_{s=1}^{S} |c_s^p - c_{s+1}^p|, \tag{4.21}$$

$$d_{\mathrm{H}}(c_s^q, c_{s+1}^q) = min\{d_{\mathrm{H}}(c_s^q, c_{s+1}^q) \big| c_s^q, c_{s+1}^q \in C^q, c_s^q \neq c_{s+1}^q\} = \sum_{s=1}^{S} \big| c_s^q - c_{s+1}^q \big|, \qquad (4.22)$$

additionally, $d_{\mathrm{H}}(c_s^q, c_{s+1}^q)$ is also equal to the Levenshtein distance at arrays p and q, i.e., termed

as $lev_{c_s^p, c_{s+1}^p}(|c_s^p|, |c_{s+1}^p|)$ and $lev_{c_s^q, c_{s+1}^q}(|c_s^q|, |c_{s+1}^q|)$, respectively.

3) Balanced Sequence

Since the codeword length is even, each codeword $c_s^p \in C^p$ and $c_s^q \in C^q$ is also a

balanced sequence, and the Hamming weight is equal to $e/2$.

4) Cross-Correlation

The cross-correlation between any codewords in arrays p and q is expressed in order as:

$$R_{c_s^p c_{s+1}^p}(0) = \sum_{s=1}^{S} c_s^p c_{s+1}^p = 0, \qquad (4.23)$$

$$R_{c_s^q c_{s+1}^q}(0) = \sum_{s=1}^{S} c_s^q c_{s+1}^q = 0. \qquad (4.24)$$

Overall, the zero cross-correlation obtained here preserves the orthogonal property of the

proposed block-codes. Hence the array factor for the MB-ABF (after beam coding) is given by:

$$U_{MS} = \frac{1}{N_T^p} \begin{bmatrix} \sum_{n=1}^{\eta_1^p} c_1^p a_n \exp(-jk_v d_n \cos\Theta_1^p), \sum_{\eta_1^p+1}^{\eta_2^p} c_2^p a_n \exp(-jk_v d_n \cos\Theta_2^p), \dots \\ \sum_{\eta_{S-1}^p}^{\eta_T^p} c_S^p a_n \exp(-jk_v d_n \cos\Theta_S^p) \end{bmatrix}^{\mathrm{T}}$$

$$+ \frac{1}{N_T^q} \begin{bmatrix} \sum_{n=1}^{\eta_1^q} c_1^q a_n \exp(-jk_v d_n \cos\Theta_1^q), \sum_{\eta_1^p+1}^{\eta_2^q} c_2^q a_n \exp(-jk_v d_n \cos\Theta_2^q), \dots \\ \sum_{\eta_{S-1}^p}^{\eta_T^q} c_S^q a_n \exp(-jk_v d_n \cos\Theta_S^q) \end{bmatrix}^{\mathrm{T}} \qquad (4.25)$$

$$= \frac{1}{N_T^p} \big[u_1^p, u_2^p, \dots, u_S^p \big]^{\mathrm{T}} + \frac{1}{N_T^q} \big[u_1^q, u_2^q, \dots, u_S^q \big]^{\mathrm{T}},$$

98

where the response vectors for each section s at arrays p and q at the MS is denoted by

$$u_s = [u^p_1 \dots u^p_S, u^q_1 \dots u^q_S].$$

4.2.4 Signal Model

A full-duplex link with CSI knowledge is also assumed at the BS and MS. Hence the transmitted signals from each section s at p and q at the BS is expressed, respectively, as:

$$x^p_s = v^p_s z_1 \text{ and } x^q_s = v^q_s z_1 \tag{4.26}$$

where v^p_s and v^q_s in order are the response vectors of section s at p and q, respectively. Meanwhile, z_1 in Eq. (4.26) represents the control signal that carries the BS codewords generated from each section at p and q. Hence the overall signal transmitted by the MB-ABF after beam coding is:

$$X_{\text{BS}} = \sum_{s=1}^{S} x^p_s + x^q_s. \tag{4.27}$$

Meanwhile the received signal model at p and q at the MS is also given by:

$$\Upsilon = \sqrt{P_{\text{tr}}} \left(\sum_{s=1}^{S} (u^q_s)^{\text{H}} + \sum_{s=1}^{S} (u^q_s)^{\text{H}} \right) X_{\text{BS}} H + w, \tag{4.28}$$

where P_{tr} is the transmitted signal (equally split between the primary beams and grating lobes). Note that this setup assumes a geometric channel and floating-intercept path loss model, i.e., Eq. (3.6) and Eq. (3.7), respectively.

4.2.5 Simultaneous Multi-Beam Access Procedure

Based upon the above architecture and notation, the multi-beam access procedure is now detailed, i.e., including beam signature discovery, feedback signaling, and grating lobe refinement.

1) Unique Primary Beam Signature Discovery

This stage broadcasts the PRCS in a directional and simultaneous manner over the entire azimuth plane, i.e., in order to avoid beam scanning and save time resources. Consider a BS and MS equipped with the proposed MB-ABF model. Hence, the main objective is to identify the maximum response vectors, $(u_s, v_s)_{max}$, and thereby determine the best simultaneous primary beams at the BS and MS which maximize the received signal levels, i.e., $\Theta_{s\_bst}^{BS}$ ($\Theta_{s\_bst}^{BS} \in \Theta_{rad}^{BS}$) and $\Theta_{s\_bst}^{MS}$ ($\Theta_{s\_bst}^{MS} \in \Theta_{rad}^{MS}$), respectively. In order to achieve this goal, the received signals at the MS and the BS are cross-correlated with the hamming block-codes, $C=\{C^P, C^q\}$, as follows:

$$(u_s, v_s)_{max} = max \ R_x(\Upsilon, C) \tag{4.29}$$

Now it is also assumed that the BS and MS use the same codewords for their primary beams. Therefore once a signal is impinged at the effective aperture of the MS, the maximum cross-correlation between the received signal and the block-codes is calculated (similar approach also employed for signals arriving at the BS). The above output is a unique codeword which is then used by the BS to achieve improved signal reception at the MS. Thereafter, the MS relays this information back to the BS via the *secondary reference control signal* (SRCS), termed as z_2.

2) Feedback Signal

The SRCS signals from the MS are sent in an open-loop feedback manner from each section *s*. These signals contain important information on the best-detected codeword at the BS, i.e., in order to notify the BS about its best codewords. Specifically:

$$y_s^p = u_s^p z_2 \text{ and } y_s^q = u_s^q z_2, \tag{4.30}$$

$$x_s^q = v_s^p z_2 \text{ and } x_s^p = v_s^p z_2. \tag{4.31}$$

Moreover, if the highest signal comes from the direction of the grating lobe, then the primary beam associated with this grating lobe is selected for refinement in the successive stage.

3) Grating Lobes Refinement

Since the maximum array response comes from the direction of the best primary beam, $\Theta_{s\_bst}^{BS}$, and its affiliated grating lobe, $\Theta_{g\_bst}^{BS}$, directional ambiguity can occur if signals are detected in the presence of grating lobes. In this case, the array cannot resolve the precise angle of the highest signal, which can either be $\Theta_{s\_bst}^{BS}$ or $\Theta_{g\_bst}^{BS}$. As a result, a further sequential refinement stage is implemented here in the directions of $\Theta_{s\_bst}^{BS}$ and $\Theta_{g\_bst}^{BS}$. Specifically, once $(u_s, v_s)_{max}$ are identified, then the directions $\Theta_{s\_bst}^{BS}$ and $\Theta_{g\_bst}^{BS}$, are fed to an adjacent series SB-ABF connected to the MB-ABF through an RF switch. This SB-ABF is composed of a ULA with an antenna spacing of $d_n = \lambda/2$, which helps suppress the grating lobes and radiate a single high-resolution beam. Note that sequential beam scanning is only done using this SB-ABF over $\Theta_{s\_bst}^{BS}$ and $\Theta_{g\_bst}^{BS}$, i.e., no need for additional beam coding in this stage. The beam direction returning the maximum channel capacity, i.e., $[\Theta_0^{MS}, \Theta_0^{BS}]_{bst}$ is finally selected for the data-plane, formulated as:

$$[\Theta_0^{MS}, \Theta_0^{BS}]_{bst} = max \, \log_2 \left[\frac{P_t \check{G}_{MS} \check{G}_{BS} |h_l|^2}{\Psi T_0 \textrm{б}} \right] \tag{4.32}$$

$$\Theta_0^{MS} = \left\{ \Theta_{s\_bst}^{MS}, \Theta_g^{MS} \,\middle|\, \Theta_0^{MS} \in u_s^{max}, \Theta_{g\_bst}^{MS} \in \Theta_{s\_bst}^{MS} \right\} \tag{4.33}$$

$$\Theta_0^{BS} = \left\{ \Theta_{s\_bst}^{BS}, \Theta_g^{BS} \,\middle|\, \Theta_0^{BS} \in v_s^{max}, \Theta_{g\_bst}^{BS} \in \Theta_{s\_bst}^{BS} \right\} \tag{4.34}$$

where б is the contiguous channel bandwidth (in MHz), Ψ is the Boltzmann constant and T_0 is the operating temperature (in Kelvin).

4.2.6 Simultaneous Multi-Beam Access Performance

The efficiency of the proposed multi-beam access scheme is examined for a single BS and MS operating in NLoS environment with regards to directivity and access times. Again,

comparisons are also made with the same set of existing mmWave initial access methods used in Chapter 3 and Section 4.1. The various (MB-ABF) system parameters used here are also summarized in Table 4.3.

1) Directivity

As mentioned earlier, large spacing between antenna elements will increase array aperture, thereby reducing beamwidth broadening rates and increasing directivity, i.e., if $\lambda/2 \leq d_n \leq \lambda$. By contrast, when $d_n > \lambda$, the array aperture and directivity start to decay significantly as the sidelobes become more enlarged, i.e., a substantial amount of radiated energy is dedicated to the sidelobes. Hence the highest possible directivity is achieved in the presence of grating lobes, i.e., by maintaining the maximum array response values *at $d_n = \lambda$*. Overall, the directivity for the proposed MB-ABF design at array p (and similarly at array q) in the broadside and endfire directions is given by [75]:

$$D_0[\text{dBi}]=\begin{cases} 10\log_2\left[2\eta_s^p\frac{d_n}{\lambda}\right], & \text{for } 0 < \{\Theta_{rad}^{MS}, \Theta_{rad}^{BS}\} < \pi, \\ 10\log_2\left[4\eta_s^p\frac{d_n}{\lambda}\right], & \text{for } \{\Theta_{rad}^{MS}, \Theta_{rad}^{BS}\} = 0, \pi. \end{cases} \tag{4.35}$$

Table 4.4: System parameters for the simultaneous multi-beam analog beamformer

Category	Parameters	Value
System	P_t(dBm), f_α(GHz), $\overline{6}$, T_0	30, 28, 800, 290
Channel	∂, σ_w^2, r	0, 1, 200
MB-ABF	η_s^p, N_T^p, S, N_T^{MS}, B_T, a_n, d_n, g_s, G_T	8, 128, 32, 256, 64, 1, 0.0107, 1, 32
Block-codes	d_H, W_H, ς, e, $\mathcal{N}$	4, 4, 2, 8, 16
SB-ABF	d_n, B_T, g_s, G_T, N_T^{MS}	5.3e-3, 1, 0, 0, 56
Time-slots	t_{PRCS} (μs)	200
μ, log$N$	Υ(dB), Γ(dB), σ(dB)	117, 0.4, 8.3

Overall, the results in Figure 4.10 confirm that the proposed MB-ABF scheme delivers 50% better directivity in the broadside and endfire directions, i.e., as compared to wide beam scanning using a SB-ABF desiggn, as propsoed in Chapter 3. Indeed, this increased directivity can potentially boost transmission ranges by compensating for penetration losses (~ 30dB). This saliency also reduces blockage sensitivity and enhances the richness of sparse mmWave channels. In light of these merits the MB-ABF scheme provides an efficient alternative for low-resolution codebooks in 802.11ad, 802.11ay, and mmWave cellular systems.
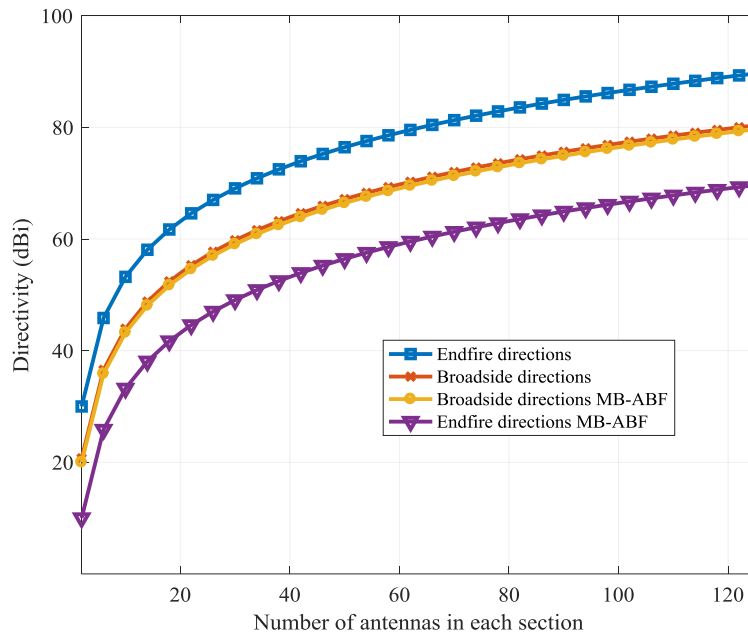
Figure 4.10: Directivity at broadside and endfire directions for MB-ABF

2) Initial Access Times

The proposed MB-ABF scheme also supports fast beam access times for narrow (pencil) beams ($\phi_s^p = 5.5^{\text{o}}$). Now the initial access time, τ_a, is defined here as the required duration for the BS (or MS) to transit from sleep-mode to active-mode. In other words, it is the time required for beam association prior to data-plane transmission, i.e., $\tau_a = M_T\, t_{\text{PRCS}}/R_{\text{MS}}$, where M_T, R_{MS} and t_{PRCS} are the number of time-slots dedicated for the beam control signals, number of RF

chains at the MS, and the PRCS duration, respectively. Now the total number of time slots prior to data plane transmission at the MS, M_T^{MS}, termed as is also given by:

$$M_T^{MS} = M_S^{MS} + M_{fb}^{MS} + M_{ref}^{MS},\qquad(4.36)$$

where M_S^{MS}, M_{fb}^{MS} and M_{ref}^{MS} in order represent the number of time-slots occupied (at the MS) during the transmission of the simultaneous primary beams, the number of time-slots for feedback signaling and the number of time-slots for refinement over the best primary beam and its affiliated grating lobe.

Next, Figure 4.11 plots the initial access times as a function of the transmitted primary beams (for a range of schemes). Now consider various numbers of transmitted beams in Figure 4.11. First, for small number of transmitted beams (e.g., B_T=16), single time-slot is occupied during the simultaneous primary beams control and feedback signaling transmission (M_S^{MS} =1 and M_{fb}^{MS} =1), whereas four time-slots are occupied during the refinement stage (M_{ref}^{MS} = 4). Similarly, for larger number of transmitted beams (e.g., B_T=64), PRBS control signaling is sent using one time-slot simultaneously over 32 beams. Additionally, one time-slot is used for feedback (i.e., sending z_2 signal), and four time-slots are used for refinement over the best primary beam and its grating lobe. Overall, the proposed scheme requires fixed number of time-slots for any number of transmitted primary beams. Hence the proposed scheme delivers notably faster access times versus all other methods [40]-[43], i.e., ranging from 75-88%. For example, the access time needed to acquire a pencil beam (ϕ_s^p = 5.5°) is 1.2 milliseconds versus 4.8 ~ 9.8 milliseconds for the other access methods. Overall, a key benefit of the proposed MB-ABF scheme is that it uses a fixed number of time-slots, i.e., regardless of the number of transmitted primary beams.
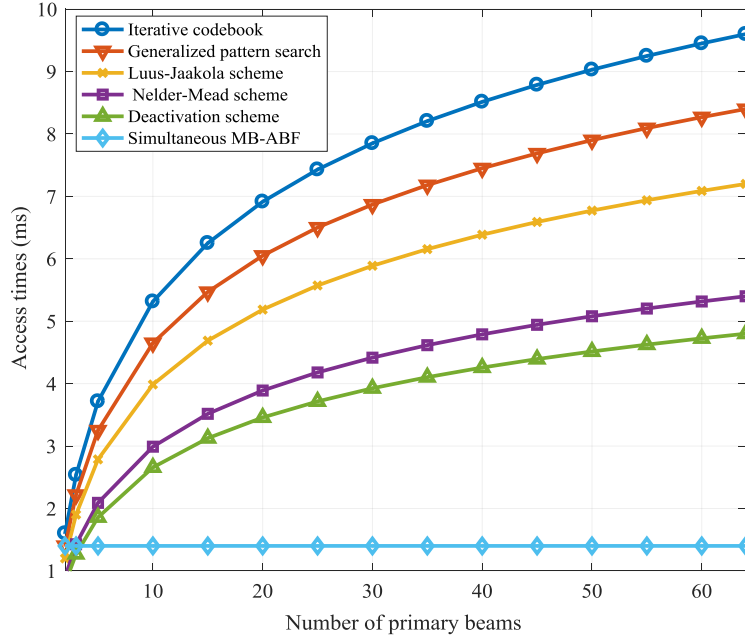
Figure 4.11: Beam access times for different number of primary beams

4.3 Dual-Beam (DB) Scanning for mmWave Initial Access

Finally, a new direct pattern search strategy is also developed here based upon the aforementioned simultaneous MB-ABF architecture, i.e., to achieve a combination of *dual-beam* (DB) codebook transmission and beam coding for faster initial access. Again, the access formulation model introduced in Section 3.1 is adopted here. The proposed algorithm adapts beam search by conquering the observed clusters profile. Namely, it tests the aggregated spatial locations of received clusters by using wide DB to capture the overall azimuthal spatial lobe of each cluster (and its affiliated rays at each codebook stage). An extended system model is first presented to introduce the proposed design, i.e., leveraging from the definitions in Chapter 3.1 Subsequently, the access scheme is detailed along with some performance results.

4.3.1 Codebook Structure for Dual-Beam Scanning

Now simultaneous *dual-beam analog beamformer* (DB-ABF) system is developed here based upon the array structure in Section 4.2. Namely, consider the codebook structure defined

in Section 4.2.1 with $y = 1, 2,.., Y$ stages and B simultaneous beams for $d = 1, 2, \ldots, D$ total radiated scanning directions per codebook stage ($D = 2B$). A sample single-stage codebook design with this DB structure is shown in Figure 4.12 in the broadside and endfire directions. The resultant array output at the MS (likewise at the BS) has b simultaneous beams in D directions pointing in Θ_S^{MS} directions, and this array is fed with a single RF unit. Hence the transmitted signal is simultaneously split into S multiple sections (transmissions) in the array.

Furthermore, orthogonal codes are also assigned to all D radiated beams in order to create distinguishable spatial signatures and retrieve the SoI. Specifically, an orthogonal extended Hamming block-code is also developed here (akin to Section 4.2.3) for each codebook stage y, $C_y[e, N, d_H]$, where each stage has $c_{y,D}$ unique codewords, i.e., each b beam at d direction is assigned a single codeword $c_{y,d}$, mapped as:

(a) Codebook Stage I (broadside)   (b) Codebook Stage I (endfire)
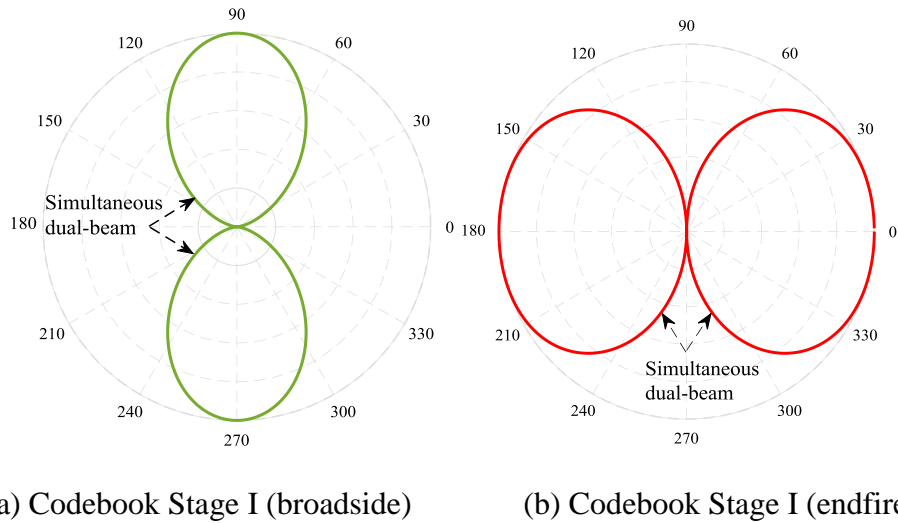
Figure 4.12: Simultaneous dual-beam transmission

$$c_{1,1}=[-1\ -1\ -1\ -1\ -1\ -1\ -1\ -1],\ c_{1,2}=[1\ -1\ -1\ -1\ 1\ 1\ 1\ -1],$$

$$c_{1,3}=[-1\ 1\ -1\ -1\ 1\ -1\ 1\ 1],\ c_{1,4}=[-1\ -1\ 1\ -1\ 1\ 1\ -1\ 1], \tag{4.37}$$

$$c_{2,1}=[-1\ 1\ 1\ 1\ 1\ -1\ -1\ -1],\ c_{2,2}=[1\ -1\ 1\ 1\ -1\ 1\ -1\ -1],$$

$$c_{2,3}=[1\ 1\ -1\ 1\ -1\ -1\ 1\ -1],\ c_{2,4}=[1\ 1\ 1\ -1\ -1\ -1\ -1\ 1], \tag{4.38}$$

$$c_{3,1}=[-1\ 1\ -1\ 1\ -1\ 1\ 1\ -1],\ c_{3,3}=[-1\ 1\ -1\ 1\ 1\ -1\ -1\ 1], \tag{4.39}$$

$$c_{3,3}=[-1\ 1\ 1\ -1\ -1\ 1\ -1\ 1],\ c_{3,4}=[-1\ 1\ 1\ -1\ 1\ -1\ 1\ -1].$$

Finally, each codeword has $Ƅ_F$, where $F=\eta_s^y$ codebits that linearly multiply the antenna's amplitude excitation, a_n, in each section s. In notational form this operation is represented as:

$$C_y=[c_{y,1},\ c_{y,2},\ldots,c_{y,D}]^T \text{ and } c_{y,d}=[Ƅ_1,\ Ƅ_2,\ldots,Ƅ_F], \tag{4.40}$$

whereas the cross-correlation between any two successive codewords is $R(0)=\sum_{d=1}^{D}c_{y,d}\ c_{y,d+1}=0$. Note that this property preserves the orthogonality of the proposed block-codes, which is essential for determining the unique angular direction.

4.3.2 Signal Model for Dual-Beam Scanning

Assuming a *time-division duplexing* (TDD) channel access scheme at the BS and MS, the overall DB-ABF transmitted signal (after beam coding at the BS) is given by:

$$X_{BS}=\sum_{s=1}^{S}x_s,\quad x_s=v_sz_1, \tag{4.41}$$

where x_s, v_s and z_1, in order, are the transmitted signal from s, the array response vectors of s, and the PSS carrying the BS control signals, e.g., *constant amplitude zero auto-correlation* (CAZAC) sequences. Meanwhile the received signal at the MS is also formulated as:

$$\Upsilon = \sqrt{P_{tr}}\left(\sum_{s=1}^{S}(u_s)^H\right)X_{BS}H+w, \tag{4.42}$$

where P_{tr} is the transmitted signal (equally-split between S antenna sections) and the channel, H, follows a geometric model given by Eq. (3.6).

4.3.3 Access Scheme for Dual-Beam Scanning

The overall DB access scheme is shown in Figure 4.15 and consists of several search phases. Akin to Section 3.2, the objective function here is also defined by the received power level, $y_l(P_m(r_i, s_j))$, and hence the goal is to find of the pair that maximizes the received signal, written as:

$$(r_i, s_j)_{bst_y} = max \{y_l(P_m(r_i, s_j)) | P_m \subset \hat{G}\}, \quad s.t. \text{ i, j, } \in [1, D]. \tag{4.43}$$

Now Figure 4.13 plots a sample received signal level profile for the first stage of the proposed DB codebook with a BS and MS separation distance of $r = 200$ m and narrowband settings, i.e., bandwidth (BW) $= 100$ MHz. Carefully note that this profile is composed of few dominant K clusters ranging between -100 and -110 dBm resulting from the DB transmission. Hence a novel recursive divide-and-conquer access algorithm is proposed to test a limited number of grid points at scattered locations in order to detect these K observed clusters. This search strategy resembles the received clusters profile of mmWave channels in NLoS settings. Namely, the channel exhibits a sparse cluster arrival rate, $P(K)$, with large void spatial distances between K, as per Figure 4.14, e.g., the spatial distance between observed clusters is approximately 180^0. Accordingly, the DB access scheme in Figure 4.15 implements three distinct search phases, i.e., inner, outer and edge searches. These are now detailed.
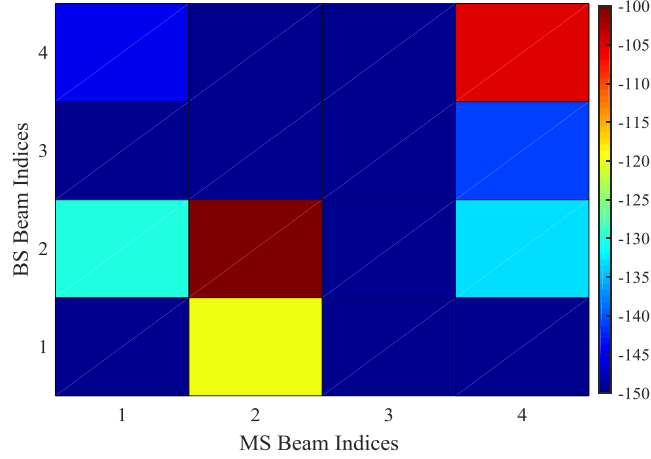
Figure 4.13: Received signal levels at different BS and MS beam indices
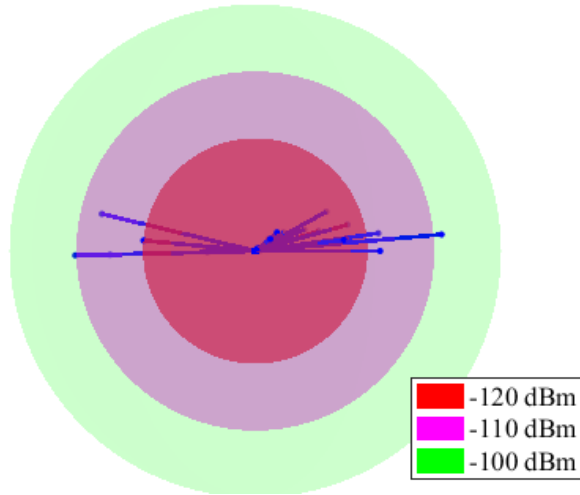
Figure 4.14: Received clusters profile

1) Phase I: Inner Exploratory Search for Best Cluster

Consider a MS and BS pair equipped with the above DB-ABF with both entities initiating asynchronous control plane communication. The initial search phase mainly tests the $\mathbb{P}_D^{in}$ adjacent centric grid points, $N = D$, for any $\mathbb{P}_m(r_i, s_j)$, i.e., to cover a large spatial region that exceeds the cluster (lobe) azimuth spread of k, $\phi_s^{MS} > A_k$. Namely, these $\mathbb{P}_D^{in}$ adjacent points are defined as:

$$\mathbb{P}_D^{in} = \{\mathbb{P}_1^{in}(r_{i_{min+\delta}}, s_{j_{min+\delta}}), \mathbb{P}_2^{in}(r_{i_{min+2\delta}}, s_{j_{min+\delta}}), \mathbb{P}_3^{in}(r_{i_{min+\delta}}, s_{j_{min+2\delta}}), \mathbb{P}_4^{in}(r_{i_{min+2\delta}}, s_{j_{min+2\delta}})\}, \qquad (4.44)$$

where δ is the step size of the search grid, which is also equivalent to the progressive phase shift between antennas, β. Hence this approach detects the K clusters with a limited number of measurements, eliminating the need for unnecessary exhaustive sequential search. Moreover this process also detects at least one ray within any cluster corresponding to the best point in Phase I, denoted as $\mathcal{P}_{bst}^{in}$.

2) Phase II: Outer Exploratory Search for Best Cluster

The second stage defines an additional set of points, $\mathcal{P}_D^{out}$, which are uniformly located at the edges of the search grid, given by:

$$\mathcal{P}_D^{out} = \{\mathcal{P}_1^{in}(r_{i_{min}}, s_{j_{min}}), \mathcal{P}_2^{out}(r_{i_{min}}, s_{j_{max}}), \mathcal{P}_3^{out}(r_{i_{max}}, s_{j_{min}}), \mathcal{P}_4^{out}(r_{i_{max}}, s_{j_{max}})\}. \tag{4.45}$$

The signal levels at these points are then tested to find the best outer point, $\mathcal{P}_{bst}^{out}$. Next, the received signal level, $y_l(r_i, s_j)$, is compared at the inner and outer exploratory searches, i.e., $y_l(\mathcal{P}_D^{in})$ and $y_l(\mathcal{P}_D^{out})$, and the point returning the maximum received signal, $\mathcal{P}_{bst}^I(r_i, s_j)$, is selected for refinement in the final phase, where:

$$\mathcal{P}_{bst}^I(r_i, s_j) = max\{y_l(\mathcal{P}_D^{in}), y_l(\mathcal{P}_D^{out})\} = max\{y_l(\mathcal{P}_{bst}^{in}), y_l(\mathcal{P}_{bst}^{out})\}. \tag{4.46}$$

The above point corresponds to the beam indices at which the best primary cluster (cursor), k_{bst}, is spatially located at Θ_k. Overall Phases I and II detect and measure all K clusters in $[0, 2\pi]$, since $\phi_s^{MS} > A_k$. Furthermore, since the grid step size δ between $\mathcal{P}_D^{in}$ and $\mathcal{P}_D^{out}$ is less than A_k, all K clusters are detected here, yielding improved robustness.

3) Phase III: Edge Exploratory Search for Best Ray

In general, the K observed clusters are composed of l rays with the lobe azimuth spread given by a normal distribution within each cluster, i.e., $N(\rho, \varsigma^2)$, where ρ and ς^2 are the mean and standard deviation of the RMS angular ray spreads. Similarly, the pre-cursor and post-cursor

110

ray arrival rates, i.e., l_{pre} and l_{post}, generally also follow normal distributions [8], i.e., given by $N(M_{pre}, \vartheta_{pre}^2)$ and $N(M_{post}, \vartheta_{post}^2)$, where M_{pre}, ϑ_{pre}^2, M_{post}, and ϑ_{post}^2 in order are the means and variance of the number of the pre- and post- cursors. Each cluster k also has l_k rays with l_p and l_a pre- and post- cursor rays, i.e., $l_k = l_p + l_a$, and $L = Kl_k$. Hence the proposed algorithm exploits this property by testing any group of adjacent points in Phases I and II (resembling l_c arrival profile in k).

Now the highest signal direction likely exists at points adjacent to the best point $\mathcal{P}_{bst}^{I}(r_i, s_j)$, i.e., at the local rays of the cursor k_{bst}. Hence the precise spatial direction within k_{bst} must be further resolved to enable pencil beam transmission, i.e., 5-6^0 range. Hence the final phase implements an adjacent points search for $\mathcal{P}_{bst}^{I}(r_i, s_j)$ in the upward, downward or sideway directions. Namely signal levels are tested at adjacently-located rays to the sides of the cursors (pre- and post- locations). Based upon these measurements, the best primary ray returning the highest signal level, l_{bst}, is resolved at $\mathcal{P}_{bst}^{II}(r_i, s_j)$, and the directions for these beam indices are adopted for data plane transmission, see Figure 4.15.

Overall, the DB-ABF initially transmits B instantaneous beams in D directions during the beam search, and each beam tests $D/2$ grid points in Phases I-III. The unique beamforming and combining vectors (beam indices) returning the best cluster (k_{bst}) and best primary ray (l_{bst}) are then determined. Now beam coding is a vital for eliminating ambiguity in the highest received signal direction, i.e., since the D radiated beams carry data generated from a single RF chain. The direction of the highest received signal also corresponds to the maximum cross-correlation at the receiving side. Hence the received signals at the MS and BS are cross-correlated with the block-code at each codebook stage, C_y, i.e., $(u_s, v_s)_{max} = \max R(\acute{y}_l, C_y)$. Furthermore, the best

point detected across all Phases I-III is chosen as the unique codeword, $c_{y,d}^{bst}$, yielding the highest

signal level. Note that the remaining codewords are distorted as they experience high fading i.e.,

low cross-correlation.

Inputs: *Y, B, D,* δ
For $y \geq 1$, $y \leq Y$,
For $P_m(r_i, s_j) \in \hat{G}$
 Phase I
   $y_l\{P_D^{in}\}$ // *Test inner points*
   $P_{bst}^{in} \leftarrow max \; y_l\{P_D^{in}\}$ // *Best inner point*
 Phase II
   $y_l\{P_D^{out}\}$ //*Test outer points*
   $P_{bst}^{out} \leftarrow max \; y_l\{P_D^{out}\}$ // *Best outer point*
   $P_{bst}^{I} \leftarrow max\{y_l(P_{bst}^{in}), y_l(P_{bst}^{out})\}$ // *Comparison between best inner and outer points*
 Phase III
 If $P_{bst}^{I} = P_m(r_{i_{min+\delta}}, s_{j_{min+\delta}})$ // *Test adjacent point*
   $P_{bst}^{II} \leftarrow max \; \{y_l(P_m(r_{i_{min+\delta}}, s_{j_{min}}), y_l(P_m(r_{i_{min}}, s_{j_{min+\delta}})\}$, $y +1 \leftarrow y$
 Else If $P_{bst}^{I} = P_m(r_{i_{min+2\delta}}, s_{j_{min+\delta}})$
     $P_{bst}^{II} \leftarrow max \; \{y_l(P_m(r_{i_{max}}, s_{j_{min+\delta}}), y_l(P_m(r_{i_{min+2\delta}}, s_{j_{min+\delta}})\}$, $y +1 \leftarrow y$
 Else If $P_{bst}^{I} = P_m(r_{i_{min+\delta}}, s_{j_{min+2\delta}})$
     $P_{bst}^{II} \leftarrow max \; \{y_l(P_m(r_{i_{min+\delta}}, s_{j_{min+2\delta}}), y_l(P_m(r_{i_{min+\delta}}, s_{j_{min+2\delta}})\}$, $y +1 \leftarrow y$
 Else If $P_{bst}^{I} = P_m(r_{i_{min+2\delta}}, s_{j_{min+2\delta}})$
     $P_{bst}^{II} \leftarrow max \; \{y_l(P_m(r_{i_{max}}, s_{j_{min+2\delta}}), y_l(P_m(r_{i_{min+2\delta}}, s_{j_{max}})\}$, $y+1 \leftarrow y$
 Else If $P_{bst}^{I} = P_m(r_{i_{min}}, s_{j_{min}})$
     $P_{bst}^{II} \leftarrow max \; \{y_l(P_m(r_{i_{min+\delta}}, s_{j_{min}}), y_l(P_m(r_{i_{min}}, s_{j_{min+\delta}})\}$, $y +1 \leftarrow y$
 Else If $P_{bst}^{I} = P_m(r_{i_{min}}, s_{j_{max}})$
     $P_{bst}^{II} \leftarrow max \; \{y_l(P_m(r_{i_{min}}, s_{j_{max-\delta}}), y_l(P_m(r_{i_{min+\delta}}, s_{j_{max}})\}$, $y +1 \leftarrow y$
 Else If $P_{bst}^{I} = P_m(r_{i_{max}}, s_{j_{min}})$
     $P_{bst}^{II} \leftarrow max \; \{y_l(P_m(r_{i_{max-\delta}}, s_{j_{min}}), y_l(P_m(r_{i_{max}}, s_{j_{min+\delta}})\}$, $y +1 \leftarrow y$
 Else If $P_{bst}^{I} = P_m(r_{i_{min}}, s_{j_{min}})$
     $P_{bst}^{II} \leftarrow max \; \{y_l(P_m(r_{i_{max-\delta}}, s_{j_{max}}), y_l(P_m(r_{i_{max}}, s_{j_{max-\delta}})\}$, $y +1 \leftarrow y$
 End For
 End For

Figure 4.15: Direct-pattern search for dual-beam mmWave access

4.3.4 Performance Evaluation of Dual-Beam Scanning

The performance of the proposed DB-ABF access scheme is also evaluated versus the existing methods used in Chapter 3. All related system parameters here are listed in Table 4.5. Foremost, the computational complexity of the proposed DB-ABF scheme is derived as:

$$Q_T^{DB} = (Q_{in} + Q_{out} + Q_{adj})/B, \qquad (4.47)$$

where Q_{in}, Q_{out} and Q_{adj}, are the number of objective function evaluations at the inner, outer and adjacent exploratory phases, respectively. Note that the complexity of this algorithm is modeled as $O(Q_T^{DB} \log_4(D^2))$. The resulting values here are plotted in Figure 4.16 and confirm that the proposed algorithm delivers sizeable complexity reduction versus several existing methods. For example, with pencil beam transmission ($D=64$), the proposed DB-ABF scheme only requires 15 measurements as opposed to 24-48 measurements with all the other methods, i.e., 32-60% higher.

Table 4.5: System parameters for the dual-beam scheme

Category	Parameters	Value
System	f_c (GHz), bandwidth (MHz), P_{tr}	38, 100, 30
DB-ABF	$Y, \eta_s^1, \eta_s^2, \eta_s^3, B, \breve{b}, D$	3, 2, 6, 19, 2, 2, 4
Received clusters profile	$L, K, l_k, l_p, l_a, M_{pre}, \vartheta_{pre}^2, M_{post}, \vartheta_{post}^2, \rho, \varsigma^2$	8, 2, 4, 2, 2, 2, 1, 2, 1, 4, 2
DB access scheme	i, j, δ, F, e, N, d_H, M_T, Q_T^{DB}, Q_{in}, Q_{out}, Q_{adj}	4, 4, 1, 8, 8, 4, 4, 5, 5, 4, 4, 2
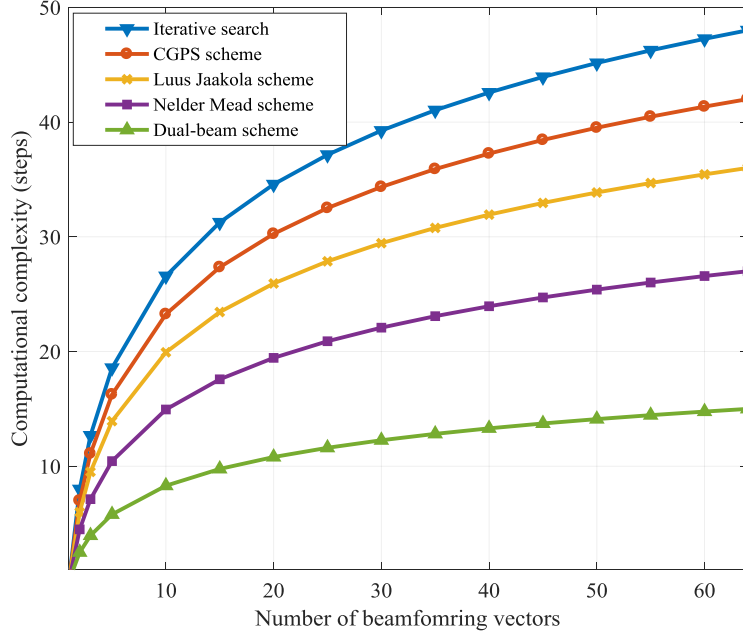
Figure 4.16: Computational complexity for the dual-beam access scheme

Finally, the initial beam access times for the proposed DB scheme τ_a is also defined as:

$$\tau_a = M_T \, t_{PSS} \, / R_{MS}, \qquad (4.48)$$

where M_T is the number of time-slots dedicated for z_1 transmission, i.e., $M_T = Q_T^{DB}$. Accordingly, Figure 4.17 plots the access times for varying numbers of simultaneously-transmitted beams for the different schemes. Again, the proposed method gives much faster performance here. For instance, the results show 40-70% lower access times when transmitting 64 beams. Namely, 3 ms are required to resolve the best beam indices (primary ray detection) at the third codebook stage versus 5-9.6 ms with the other methods.
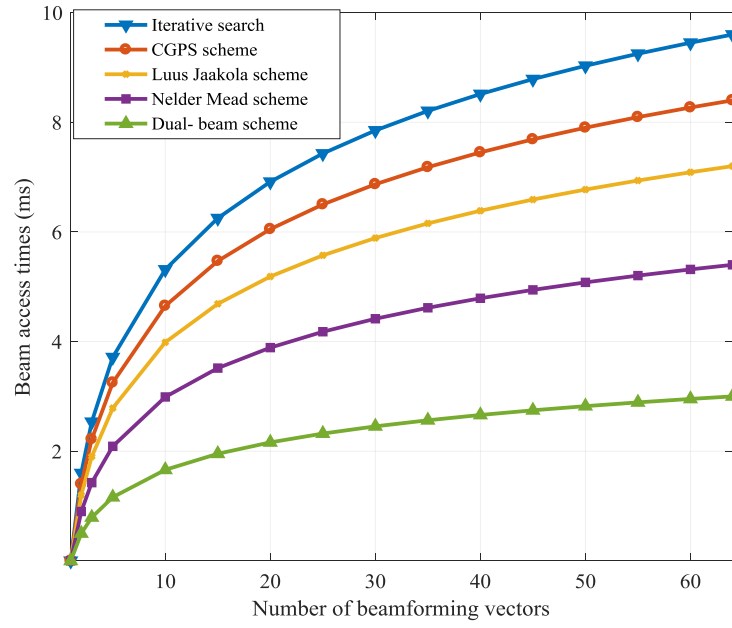
Figure 4.17: Beam access times for different transmitted beams

Chapter 5

Hybrid Beamforming Method for Link Recovery

As noted in Chapter 2, mmWave links are highly sensitive to obstacles/objects in the propagation channel, as they can cause blockage and signal degradation. For instance, obstacles such as pedestrians can yield an additional 20 dB [76] in path loss during link transition from LoS-to-NLoS operation. In turn, this drop can cause received signal levels to fall below critical receiver sensitivity levels, i.e., resulting in blockage-based outage and link failure. In addition, MS mobility can also yield alternating channel gain and fading effects. As a result, instantaneous CSI can vary rapidly, further causing link recovery times to exceed coherence times.

Now conventional link recovery techniques generally reset the spatial beam scanning procedure when the primary link between the BS and MS degrades, e.g., due to channel blockage. Namely, hierarchical codebooks are used to determine new beam directions for the highest received signal. Alternatively other strategies try to test directions that are adjacent to the recently-failed beams [77]. However, these techniques have longer recovery times, potentially resulting in a connection drop (failures). As a result, fast link adaptation and recovery (beam-maintenance) methods are required to sustain communication sessions between BS and MS in both the control- and data- planes.

In light of the above, this chapter proposes a novel dual-beam recovery method for blocked links in outdoor mmWave settings. Namely, *hybrid beamforming* (HBF) techniques are used to achieve transmit diversity and establish recovery beams. Furthermore, *equal-gain combining* (EGC) is also applied to incoming dual-beam signals if the direct LoS link is blocked,

116

i.e., to compensate for signal degradation. Overall this method mitigates the effects of link blockage and reduces link loss in Rician channels. Furthermore, the proposed link recovery method also provides near-instantaneous beam recovery without the need for a recursive exhaustive or iterative search for an alternative spatial direction. Finally, a HBF architecture is also developed based upon a ULA (along with its associated signal and blockage models). The proposed link recovery method is then presented, followed by detailed simulation and performance evaluation results to validate its effectiveness in a range of settings.

5.1 Hybrid Multi-Beam Beamformer

Consider BS and MS nodes equipped with ULA frontends with N_{BS} and N_{MS} antennas each, respectively. It is assumed that $n_{BS} \in N_{BS}$ and $n_{MS} \in N_{MS}$ adjacent antennas are also combined into $s=1,2,...,S$ sections, and each section s is connected to a single RF chain to generate a single data stream. The total number of RF chains at the MS is also denoted by R_{MS}, i.e., $S = R_{MS} << N_{MS}$. Hence the overall array and chains here form a HBF structure, which consists of a limited number of data streams radiated by $b=1,2,\dots,B$ simultaneous beams (beamforming and combining vectors) in Θ_s pointing directions. Now the design of the pointing directions of S antenna sections is determined by the precoding matrix at the BS, i.e., P_{BS}, which is composed of p precoding vectors. Specifically, P_{BS} is constructed as $P_{BS} = P_{bb}P_{an}$, where P_{bb} and P_{an} are the baseband and analog precoding stages, i.e., $P_{bb} = S \times R_{BS}$ and $P_{an} = R_{BS} \times N_{BS}$. Carefully note the RF chains are still exploited to support transmit diversity (diversity modulation) even though the HBF supports spatial multiplexing,. Hence this approach can provide link recovery and signal aggregation to compensate for signal degradation due to blockage.

5.2 Signal Model

The HBF framework here assumes a full-duplex downlink channel with reciprocal CSI knowledge at the BS and MS nodes. Hence the received RF signal at the antenna lenses in the MS (analog side of the precoder) is expressed as:

$$y_{an} = P_{BS}Hz + w_l, \tag{5.1}$$

where the complex channel H incorporates blockage effects for sparse-scattering propagation at mmWave frequencies. Specifically, this channel is represented as:

$$H = \sqrt{\frac{N_{BS}N_{MS}}{\Gamma_{bl}}} \sum_{k=1}^{K} \sum_{l=1}^{L} h_l V_{BS} U_{MS}^{H}, \tag{5.2}$$

where Γ_{bl} is the blockage path loss (in dB), and V_{BS} and U_{MS} are the array response vectors at the BS and MS, respectively, i.e., RF precoder of the HBF where the channel is captured. Note that the LoS path gains follow a Rician distribution model, i.e., $h_l \sim R(0, \zeta_c)$, where ζ_c is the ratio between the power in dominant first (direct) path component and the available power in the other paths (reflected and scattered links). Meanwhile, the overall received signal at the MS after the combiner stage C_{MS} at the baseband unit is given by:

$$y_{bb} = P_{tr}C_{MS}^{H}P_{BS}Hz + C_{MS}^{H}w_l, \tag{5.3}$$

where C_{MS} is the MS combiner and is composed of two baseband and analog combiners, i.e., $C_{MS} = C_{bb}C_{an}$. Meanwhile, the instantaneous received signal generated by the p and c beamforming and combining vectors a6 the MS, respectively, ($p \in P_{BS}$, $c \in C_{MS}$) is expressed as:

$$y_{c,p}^{inst} = P_{tr}c^{H}pHz + c^{H}w_l. \tag{5.4}$$

Hence the overall response vector for the HBF system at the MS is given by the RF precoding matrix, i.e., expressed by periodic array factor in Eq. (3.1). Furthermore, the pointing direction Θ_s at the BS and MS for each radiated beam b is also given by:

$$\Theta_s = \cos^{-1}\left[\frac{-\beta_{MS}\lambda}{2\pi d_n}\right],\tag{5.5}$$

and the HPBW is still given by Eq. (3.2)-(3.3).

5.3 Blockage Model

As mentioned earlier, mmWave direct links are very vulnerable and sensitive to obstacles. Therefore a blockage model is also incorporated here to capture the transition from LoS-to-NLoS operation in the presence of mobile obstacles. This path loss model leverages the blockage and distance parameters in [78] as follows:

$$\Gamma_{bl}=\mathbb{I}[\mathbb{p}(r)]\,\Gamma_{\text{LoS}}(r)+\mathbb{I}[1-\mathbb{p}(r)]\,\Gamma_{\text{NLoS}}(r),\tag{5.6}$$

where $\mathbb{I}$ is an indicator function that determines the adopted path loss based upon the link-blockage state, i.e., $\mathbb{I}(x)=1$ *iff* $x=1$, and 0 otherwise. Furthermore, $\mathbb{p}(r)$ and $(1-\mathbb{p}(r))$ in Eq. (5.6) represent the LoS and NLoS probabilities at distance r, i.e., $\mathbb{p}(r)=exp\,(-\varphi r)$, where φ is the blockage parameter representing obstacles size and density. Note that the LoS link length is proportional to $1/\varphi$. Also, the terms $\Gamma_{\text{LoS}}(r)$ and $\Gamma_{\text{NLoS}}(r)$ in Eq. (5.6) denote the LoS and NLoS path losses and are given by [79]:

$$\Gamma_{\text{LoS}}(r)=10\log_{10}(r_0) + 10\,\delta_{\text{LoS}}\log_{10}(r),\ \textit{for}\ \text{LoS},\tag{5.7}$$

$$\Gamma_{\text{NLoS}}(r)=10\log_{10}(r_0) + 10\,\delta_{\text{NLoS}}\log_{10}(r),\ \ \textit{for}\ \text{NLoS},\tag{5.8}$$

where δ_{LoS} and δ_{NLoS} represent in order, the PLE for the LoS and NLoS links, respectively. Hence if a LoS link is unaffected by blockage, then the NLoS term decays to zero. Overall, this

formulation indicates that the probability of encountering denser obstacles increases with larger distance (r) values, and hence $\mathbb{p}(r)$ decreases.

5.4 Link Recovery Method

In general, initial beam access procedures have to be completed before any link recovery can be attempted. Hence the proposed recovery scheme implements the following set of procedures.

1) Initial Access

Consider BS and MS nodes operating with B predefined beams generated by R_{BS} and R_{MS} RF chains, respectively, as shown in Figure 5.1. Here both sides start by initiating an exhaustive brute-force search to find the best beamforming and combining vectors. This operation returns a primary signal level of $y_{c,p}^{pri}$, corresponding to the single direct LoS path for data-plane transmission:

$$(c,p)_{bst} = max\ (y_{c,p}^{inst}). \tag{5.9}$$

Now since the BS and MS have already tested the signal levels at all p and c beamforming and combining vectors for B possible signal levels, they can readily identify the second highest signal level. Specifically, this secondary value is denoted as $y_{c,p}^{sec}$ and is associated with another pair of beamforming and combining vectors, i.e., $(c,p)_{sec}$. Similarly, the third highest signal level, $y_{c,p}^{ter}$, can also be resolved, i.e., tertiary value associated with beamforming and combining vectors $(c,p)_{ter}$. Also, the total number of selected redundant links is denoted by R_{MS}-1 (R_{BS}-1 in uplink), and only three directions are analyzed here (although further extension to multiple directions is also feasible).

Now once the primary link selection/establishment procedure is complete using $(c,p)_{pri}$, the subsequent data-plane stage is initiated. Namely, the BS and MS use the primary link

(dominant LoS link) for data transmission, i.e., this direct link provides the highest signal levels for increased channel capacity. Meanwhile, the RF chains associated with the secondary and tertiary signals are also deactivated to reduce power consumption. However, if a high level of instantaneous channel capacity is detected, then these chains can be reactivated to achieve spatial multiplexing. Namely, secondary and tertiary beam directions are reserved to establish redundant beams. Carefully note that $y_{c,p}^{pri} > y_{c,p}^{sec} > y_{c,p}^{ter} > y_{th} > y_{rx}$, where y_{th} and y_{rx} represent the threshold signal level exceeding channel capacity and receiver sensitivity, respectively, as given by Eq. (4.32). Also note that the initial access procedure can be similarly performed by adopting codebook structures.
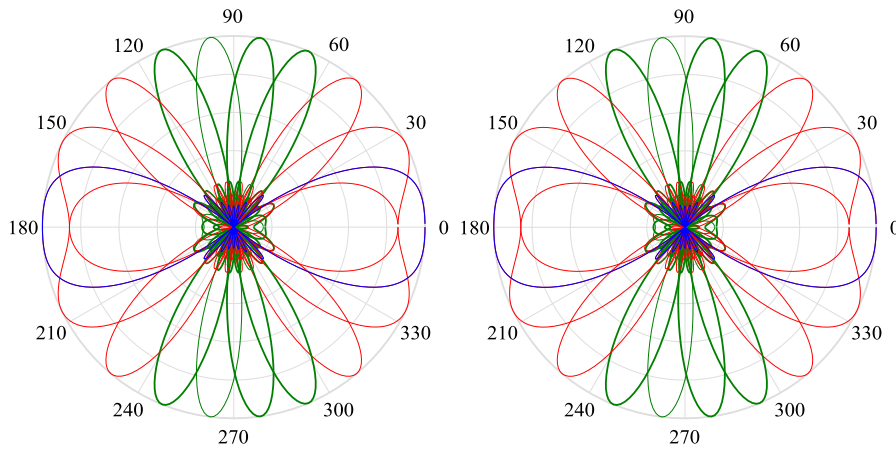
Figure 5.1: Beamforming and combining vectors at the BS and MS nodes

2) *Link Recovery Procedure*

Overall, the multiple favorable directions recorded during beam scanning are used during the recovery stage. In particular, the best beam direction returning the primary signal is used for data transmission as shown in Figure 5.2(a). Meanwhile, the secondary and tertiary beam directions are used when the main beam is blocked, see Figure 5.2(b). Hence once a blockage effect is introduced, the BS and MS utilize the simultaneous dual-beam and apply EGC to compensate for the blocked LoS link. Consider the details.

121
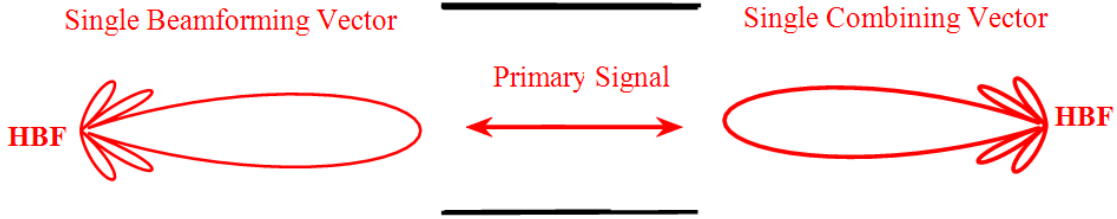
(a) Single beamforming and combining vectors returning primary signal
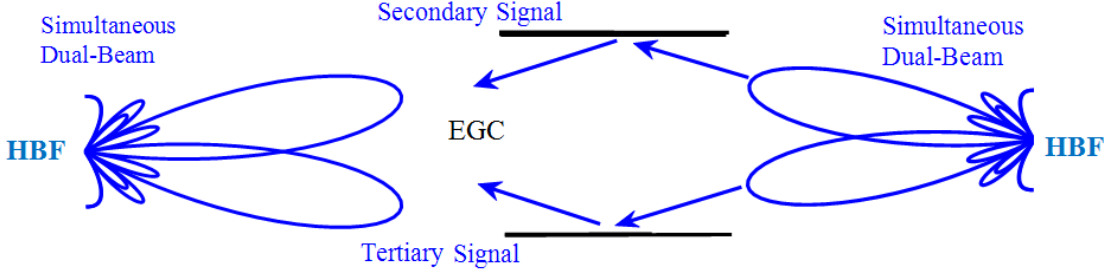
(b) Simultaneous dual-beam returning secondary and tertiary highest signals

Figure 5.2: Proposed link recovery method using simultaneous dual-beam hybrid beamforming

As noted earlier, if the primary link exhibits high signal quality, i.e., $y_{c,p}^{inst} \geq y_{c,p}^{pri}$, then the HBF only utilizes a single beam generated by a single RF chain. In other words, the remaining $(R_{MS}-1)$ chains are deactivated and their affiliated beam vectors are set to null. Thus the HBF acts as an analog beamformer in order to reduce power and energy consumption. However, if the primary link degrades, these $(R_{MS}-1)$ chains are now reactivated and data-plane transmission is recovered over these redundant links. Specifically, the redundant beam sections provide transmit diversity when the received signal level degrades due to increased blockage, i.e., $y_{c,p}^{inst} < y_{c,p}^{pri}$. Furthermore, the same data stream is redundantly transmitted across all beamforming vectors. Hence the receiving side, e.g., MS node applies the EGC method to magnify $y_{c,p}$ from all reflected paths, i.e., since the dominant link has been blocked. The received EGC signal from each redundant link (incorporating blockage) is therefore expressed as:

$$y_{c,p}^{EGC} = y_{c,p}^{sec} + y_{c,p}^{ter} = P_{tx}\, c_{sec}^{H}\, p_{sec} Hz + c_{sec}^{H} w_l + P_{tx}\, c_{ter}^{H}\, p_{ter} Hz + c_{ter}^{H} w_l. \tag{5.10}$$

122

Although the primary signal exceeds the secondary and tertiary signals, i.e., $y_{c,p}^{ter} < y_{c,p}^{sec} < y_{c,p}^{pri}$, the use of EGC here in Eq. (5.10) compensates for this differential if $y_{c,p}^{EGC} \geq y_{c,p}^{pri}$. Note that this design also assumes non-coherent channels in the secondary and tertiary links, i.e., resulting in non-coherent fading and noise correlations. By contrast, coherent channels may cause similar signal increments and hence provide zero diversity gain.

Overall the proposed HBF design implements a form of diversity switched combining at the BS and MS, i.e., where $y_{c,p}^{sec}$ and $y_{c,p}^{ter}$ are co-phased and added constructively. This approach magnifies the received signal level to compensate for a degraded/blocked primary link. In general EGC is more effective than a *maximal ratio combining* (MRC) strategy since the best directions have already been estimated during the exhaustive search stage (considering independent fading channel gains). Hence, the BS and MS nodes can simply establish alternative protection links to maintain communication without conducting new search.

5.5 Performance Evaluation

The performance of the proposed HBF link recovery scheme is compared to default recovery methods in terms of instantaneous received signal level and beam recovery times. The study assumes stationary BS and MS nodes operating in a LoS outdoor urban environment with a carrier frequency of 38 GHz and channel bandwidth of 500 MHz. Additional network test parameters are also summarized in Table 5.1.

Table 5.1: System parameters for the link recovery scheme

Category	Parameters	Value
System	f_c(GHz), BW (MHz), y_{rx}(dBm)	38, 500, -110
Channel	ζ_c, r_0, r	1.8, 5, 200
HBF	$P_{tr}, g_n, N_{BS}, N_{MS}, a, R_{BS}, R_{MS}$	30, 5, 16, 16,1 ,3, 3
Path loss	$\delta_{LoS}, \delta_{NLoS}$	2, 4

5.5.1 Received Signal Level

The received signal levels at the MS are plotted in Figure 5.3 for various blockage parameter settings In general, when the blockage parameter $\varphi = 0$, then the NLoS probability is $(1-\mathbb{p}(r)) = 0$, and the MS and BS simply operate in LoS mode over a single primary link, $y_{c,p}^{pri} > y_{th}$ (Section 5.3). However when $\varphi > 0$, the density and size of obstacles along the primary link path increase, causing severe signal degradation and link failure (NLoS operation).
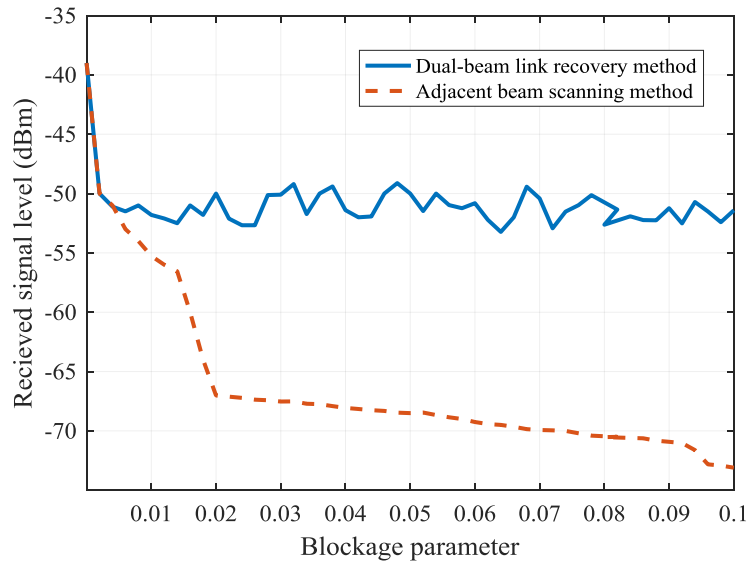
Figure 5.3: Received signal level at different blockage parameter values

Now the effectiveness of the proposed scheme method is clearly demonstrated in Figure 5.3. For example, when the link initially transits from LoS-to-NLoS operation at $\varphi = 0.002$, the redundant beams are quickly reactivated to magnify incoming signal levels from the dual-beam using EGC, i.e., to build alternative links without any iterative beam search. By contrast, the (default) adjacent beam scanning method can only maintain the signal level for a short duration, after which the link is completely blocked at $\varphi = 0.005$. Furthermore, the proposed HBF link recovery method only yields a slight degradation in the received signal level, i.e., 10 dBm from approximately -40 dBm to -50 dBm. Again, this value compares very favorably to the larger 25

dBm loss seen with the adjacent beam scanning technique. In this latter case, the levels fall below the receiver sensitivity, resulting in connection drop and repeated beam scanning and channel estimation (complexity).

5.5.2 Link Recovery Times

Link recovery time is another key performance metric here, and this value is basically defined as the scan cycle time to find an alternative (best) link, i.e., to replace a blocked primary link. Specifically, the link recovery duration is computed as $T_r = Q_{c,p}\tau_{pss}/R_{MS}$ (in microseconds), where $Q_{c,p}$ is the number of signal measurements at different combining and beamforming vectors (c, p) for detecting a new best direction. Now in the default adjacent beam scanning approach, the BS and MS nodes are forced to reset their spatial search to find a new direction after link blockage. Specifically, new beamforming and combining vectors are needed here, and these repeated beam search operations will result in prolonged recovery (re-access) times. By contrast, the proposed HBF recovery solution delivers near-instantaneous link switchovers. Accordingly, the link recovery times are also plotted in Figure 5.4 and confirm much faster operation versus the default beam scanning approach in [85], i.e., 50% lower recovery times across all tested beamforming vector sizes. Note that the proposed method also maintains constant recovery times regardless of the number of transmitted beams and their affiliated beamwidths, a key saliency.
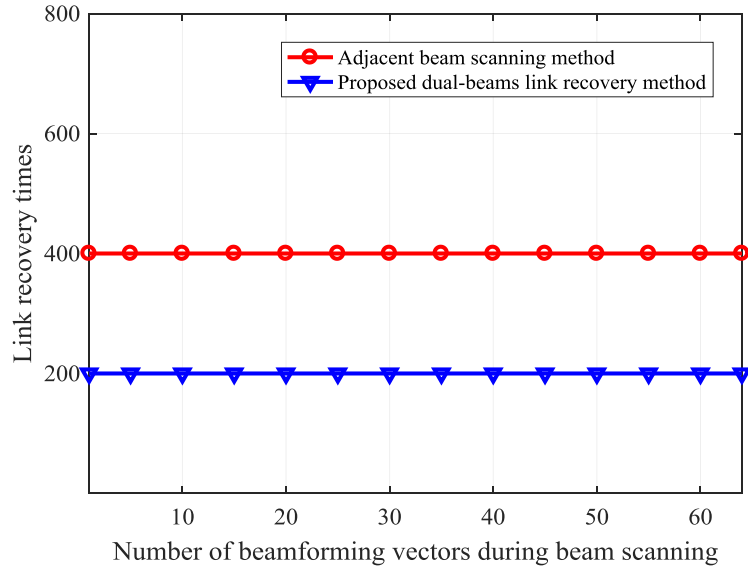
Figure 5.4: Recovery times at various number of beamforming vectors

Chapter 6

Conclusions and Future Work

This dissertation studies the topic of initial beam access challenges in beamforming-based millimeter wave (mmWave) cellular networks. First, Chapter 2 presents a background review of mmWave channel propagation characteristics. Existing research on analog, digital and hybrid beamforming designs for mmWave transceivers is then presented. Novel initial beamforming solutions are then presented in Chapter 3 based upon several meta-heuristic access strategies, i.e., Nelder Mead, Luus Jaakola, hybrid divide-and-conquer and Tabu search, coordinated generalized pattern search, and Hooke Jeeves methods. This is followed by analog beamforming architectures leveraging sidelobes, grating lobes and beam coding in Chapter 4. Finally, a link recovery method is proposed in Chapter 5 to mitigate blockage effects using hybrid beamforming. A summary of the major findings from this research are now presented along with potential future directions and extensions.

6.1 Conclusions

This dissertation research assumes directional BS and MS nodes operating in standalone outdoor mmWave network environments. Hence all of the access schemes developed here do not require any assistance from out-of-band networks. Also, the proposed beam access procedures are designed for various mmWave frequencies (28, 38 and 73 GHz) and distances (100, 200, 500 and 800 m) with provisions for varying sparsity levels.

Foremost, initial access is formulated as a search model using analog beamforming and codebook designs for random access in the control- or data- plane (Chapter 3).

Efficient meta-heuristic schemes are then developed to achieve rapid and efficient beam access. Overall, some of the key contributions and findings include:

- Novel cascaded codebook design is proposed based upon uniform linear arrays for analog beamforming transceivers. This practical solution considers beam-broadening effects and adopts practical microstrip antenna gains for array factor computations.

- A modified geometric channel model is presented to incorporate sparsity and rank levels. The model here also considers a cluster arrival pattern which composed of independent and identically distributed rays

- Novel direct pattern search schemes are proposed to solve the search model in LoS (rank-one) environments, i.e., based upon Von Neumann and Levy Flight Nelder Mead techniques. These solutions give notably better performance as compared to existing access methods, i.e., in terms of computational complexity, access times, energy consumption and success rates

- Access schemes for NLoS environments are also proposed here based upon uniform local search procedures for flat-fading channels of long coherence times, i.e., Luus Jaakola (LJ), divide-and-conquer with Tabu search (DC-TS) methods. The use of localized sub-region searches here also increases detection probabilities and lowers the confinement tendency in plateau regions

- Further, CGPS scheme is built to enhance beam access efficiency for frequency-selective fading wideband channels. This method constructs bisectional filtering to measure spatial regions with higher detection probabilities. Also, the construction of the polling directions here resembles rays arrival distribution in the received clusters profile

- Modified Hooke Jeeves access scheme is also presented for improved success rates in wideband channel bandwidths. This method evaluates multiple directional perturbation vectors (upward, downward and sideways) to improve detection of the highest signal levels and determine best beamforming and combining vectors

Nevertheless, despite the above-detailed advantages, conventional analog beamforming techniques can prolong beamforming scan cycle and access times due to the use of single beamforming and combining vectors. Hence in order to further reduce these times and meet the low latency requirements for 5G and beyond standards, novel access schemes are also proposed based upon more advanced multi-beam analog beamformers (Chapter 4). Namely, the main contributions here are as follows:

- One of the first schemes is presented to exploit sidelobe information as auxiliary information to detect the location of the main lobe during the initial access procedure. This approach mitigates the need for exhaustive beam search in multi-resolution codebooks. Associated results here show that the sidelobe-based method scheme outperforms existing solutions by substantial margins for large BS and MS distances (> 800 m) LoS settings

- Multi-beam analog beamforming transmission is proposed here that leverages grating lobes and beam coding for highly-directive initial access. This multi-beam approach is analogous to digital and hybrid beamforming techniques in terms of spatial diversity and time-division duplexing channel capacity, but yields reduced power consumption.

- Improved antennas spacing design is presented to avoid enlarged sidelobes and mutual coupling. This technique is one of the first to generate grating lobes to increase to increase the number of main lobes visible in one beamforming scan cycle

- Furthermore, orthogonal block-codes are also developed to be assigned to the radiated beams in order to generate distinctive spatial signatures. This orthogonality is preserved here by the zero cross-correlation properties of the proposed codes

- The proposed multi-beam approach is well-suited for highly-directive access and hence compensates for low gains associated with wide beams. Also, access times achieved here represent one the shortest reported times in mmWave standalone access, i.e. 3-5 ms

- A novel direct pattern search algorithm is also developed to leverage simultaneous dual-beam analog beamforming transmissions, i.e., motivated by clusters and rays arrival profile of sparse mmWave channels to achieve faster access times

Channel obstacles and user (MS) mobility can result in mmwave link failure. As a result, conventional recovery techniques have to reset spatial search to find alternative beamforming and combining vectors. To address these concerns, a new link recovery procedure is also presented to mitigate signal degradation using equal gain combining at the receiver (Chapter 5). The key contributions and outcomes here are summarized as follows:

- A novel hybrid beamforming recovery method is proposed for instantaneous link recovery during transition from LoS to NLoS settings in Rician channels. This solution utilizes the first highest received direction (direct path) for data-plane transmissions and further redundant dual-beam along second and third highest directions. These backup beams activated/deactivated based upon instantaneous channel capacity status, i.e., power efficient recovery scheme

- The proposed solution incorporates various channel blockage parameters in order to model obstacles with different size and shape

- Equal gain combining technique is also utilized for the first time in mmWave transceivers to enhance the received signal levels

- Overall, the proposed recovery method eliminates the need for repeated beam scanning for alternative spatial directions associated with high received signal levels. Also, the solution here yields near-instantaneous recovery times and thereby avoiding connection drops

6.2 Future Work

This dissertation presents some new innovations and findings for initial beam access design in mmWave networks. Furthermore, these contributions also open up several new avenues for future research. Some potential major future directions here include:

- *Channel coherence time modeling:* Here channel coherence time models need to be developed for wide and narrow beamforming and combining vectors, and these solutions must also take into account MS mobility and Doppler effects

- *Multi-user beam access:* The proposed schemes designed in this dissertation also need to be evaluated for more complex multi-user access scenarios. These settings will require digital beamforming designs at the BS to support multi-stream transmission. Furthermore, co-channel interference effects must also be considered here, and interference exploitation and mitigation techniques can also be applied to resolve signals of interest

- *Channel estimation:* Geometric channel models are generally composes of multiple path gains and angles of arrivals/departures (beamforming/combining vectors). Note that work in this dissertation has only looked at estimating the latter quantities. As a result, future extensions can develop path gains estimation schemes based upon sparse approximation algorithms to estimate overall channel components

- *Edge-user beam access:* A MS located near the edge of a cell in an overlay network will requires further coordinated multi-point access schemes which incorporate beamforming

131

transmissions. These solutions must necessary consider a wider set of design metirics, e.g., such as aggregated power gains, channel ranks, diversity gains, and cell breathing and off-loading

- *Beam-tracking:* User mobility and channel fluctuations can cause mmWave link degradation. Hence other key focus areas also include instantaneous link quality estimation and the design of rapid beam-tracking schemes to maintain BS and MS mode locations

References

[1]   Third Generation Partnership (3GPP), "NR user equipment radio transmission and reception; Part 1: Range 1 standalone", TS 38.101-1, 3GPP Specifications Series, December 2017.

[2]   Federal Communication Commission, "In the matter of use of spectrum bands above 24 GHz for mobile radio services", FCC 16-89, July 2016.

[3]   A. Swindlehurst, E. Ayanoglu, P. Heydari, and F. Capolino, "Millimeter-wave massive MIMO: The next wireless revolution?" *IEEE Communications Magazine*, Vol. 52, No. 9, September 2014, pp. 56-62.

[4]   J. G. Andrews *et al.*, "What will 5G be?" *IEEE Journal of Selected Areas in Communications*, Vol. 32, No. 6, June 2014, pp. 1065-1082.

[5]   W. Roh *et al.*, "Millimeter-wave beamforming as an enabling technology for 5G cellular communications: Theoretical feasibility and prototype results," *IEEE Communications Magazine*, Vol. 52, No. 2, February 2014, pp. 106-113.

[6]   Z. Pi and F. Khan, "An introduction to millimeter-wave mobile broadband systems," *IEEE Communications Magazine*, Vol. 49, No. 6, June 2011, pp. 101-107.

[7]   T. S. Rappaport *et al.*, "Millimeter wave mobile communications for 5G cellular: It will work!" *IEEE Access*, Vol. 1, May 2013, pp. 335-349.

[8]   M. Akdeniz *et al.*, "Millimeter wave channel modeling and cellular capacity evaluations," *IEEE Journal of Selected Areas in Communications*, Vol. 32, No. 6, June 2014, pp. 1164-1179.

[9]   H. Zhao *et al.*, "28 GHz millimeter wave cellular communication measurements for reflection and penetration loss in and around buildings in New York City," *in 2013 IEEE International Conference on Communications (ICC)*, June 2013. Budapest, Hungary.

[10]   S Nie, G. MacCartney, S. Sun, T. S. Rappaport, "72 GHz Millimeter eave indoor measurements for wireless and backhaul communications," *in 2013 IEEE International Symposium on Personal, Indoor and Mobile Radio Communications (PIMRC)*, September 2013, London, UK.

[11] T. S. Rappaport, Y. Qiao, J. Tamir, J. Murdock, E. Ben-Dor, "Cellular broadband millimeter wave propagation and angle of arrival for adaptive beam steering systems," in *2012 IEEE Radio Wireless Symposium (RWS)*, January 2012. Santa Clara, CA, USA.

[12] Y. Azar, G. Wong, K. Wang, R. Mayzus, J. Schulz, H. Zhao, F. Gutierrez, D. Hwang, and T. S. Rappaport, "28 GHz propagation measurements for outdoor cellular communications using steerable beam antennas in New York City," in *2013 IEEE International Conference on Communications (ICC)*, June 2013, Budapest, Hungary.

[13] W. Heath, T. S. Rappaport, R. Daniels, J. Murdock, "Radio wave propagation for mmWave," Millimeter Wave Wireless Communications, 1st ed., New York City, Prentice Hall Communications Eng., Pearson, 2014, Ch. 3, Sec. 2, pp. 105-135.

[14] S. A. Saberali, N. C. Beaulieu, "New expressions for TWDP fading statistics," *IEEE Wireless Communications Letters*, Vol. 2, No. 6, December 2013, pp. 643–646.

[15] International Mobile Telecommunications, "Minimum requirements related to technical performance for IMT-2020 radio interface," ITU-R Study Group 5, No. R15-SG05-C-0040, Feburay 2017, pp. 6-7.

[16] C. Balanis, "Electric Properties of matter" in Advanced Engineering Electromagnetics, 1st ed., New York, Wiley Press, 1989, Ch. 2, Sec. 1.5, pp. 12-17.

[17] S. Seidel *et al.*, "The impact of surrounding buildings on propagation for wireless in-building personal communications system design," in *1992 IEEE Vehicular Technology Conference (VTC)*, May 1992, Denver, CO, USA, USA.

[18] E. Bahar, P. Crittenden, "Stationary solutions for the rough surface radar backscatter cross sections based on a two scale full wave approach," *in 1999 IEEE Antennas and Propagation Society International Symposium*, August 1999, Orlando, FL, USA.

[19] T. S. Rappaport et. *al*, "Radio Wave Propagation for MmWave," *Millimeter Wave Wireless Communications*, 1st Ed., New York City, Pearson, 2014, Ch. 3, Sec. 3.7, p. 186.

[20] H. Kim, G. de Veciana, X. Yang, M. Venkatachalam, "Distributed α-optimal user association and cell load balancing in wireless networks," *IEEE/ACM Transactions on Networks*, Vol. 20, No. 1, February 2012, pp. 177-190.

[21] M. Samimi *et al.*, "28 GHz angle of arrival and angle of departure analysis for outdoor cellular communications using steerable beam antennas in New York City," in *2013 IEEE Vehicular Technology Conference (VTC 2013)*, June 2013, Dresden, Germany.

[22] E. Ben-Dor et al., "Millimeter wave 60 GHz outdoor and vehicle AOA propagation measurement using a broadband channel sounder," in *2011 IEEE Global Communications Conference (GLOBECOM)*, December 2011, Houston, TX, USA.

[23]   T. Rappaport *et al*., "Broadband millimeter wave propagation measurements and models using adaptive-beam antennas for outdoor urban cellular communications," *IEEE Transactions on Antennas and Propagation*, Vol. 61, No. 4, April 2013, pp. 1850–1859.

[24]   T. Rappaport, E. Ben-Dor, J. Murdock, Y. Qiao, "38 GHz and 60 GHz angle-dependent propagation for cellular & peer-to-peer wireless communications," in *2012 IEEE International Conference on Communications (ICC)*, June 2012, Ottawa, Canada.

[25]   T. Wu, T. Rappaport, C. Collins, "The human body and millimeter-wave wireless communication systems: interactions and implications," in *2015 IEEE International Conference on Communications (ICC)*, June 2015, London, UK.

[26]   W. Roh, "Performances and feasibility of mmWave beamforming prototype for 5G cellular communications," DMC R&D Center, Samsung Electronics Corp, June 2013.

[27]   O. Orhan, E. Erkip, S. Rangan, "Low power analog-to-digital conversion in millimeter wave systems: Impact of resolution and bandwidth on performance," in *2015 Information Theory Applications (ITA) Workshop*, February 2015 San Diego, CA, USA.

[28]   A. Poon, M. Taghivand, "Supporting and enabling circuits for antenna arrays in wireless communications," *Proceedings of the IEEE*, Vol. 100, No. 7, July 2012, pp. 2207-2218.

[29]   E. Dahlman, S. Parkvall, J. Skold, P. Beming, "Multi-antenna techniques," in 3G Evolution: HSPA and LTE for Mobile Broadband, 2nd Ed., 2010, Academic Press, Oxford, UK, Ch.6, Sec. 6.2, pp. 82-83.

[30]   D. Pepe, D. Zito, "Two mmWave vector modulator active phase shifters with novel IQ generator in 28 nm FDSOI CMOS," *IEEE Journal of Solid-State Circuits*, Vol. 52, No. 2, February 2017, pp. 344-356.

[31]   M.Tsai, A. Natarajan, "60 GHz passive and active RF-path phase shifters in silicon," in *2009 IEEE Radio Frequency Integrated Circuits Symposium (RFIC)*, June 2009, Boston, MA, USA.

[32]   S. Ryu, H. Vardhan, B. Banerjee, R. Prakash, "Continuous active phase shifter design and analysis for millimeter wave circuits" *IEEE Transactions on Circuits and Systems*, Vol. 60, No. 10, October 2013, pp. 627-631.

[33]   R. Guo *et al*., "Joint design of beam selection and precoding matrices for mmWave MU-MIMO systems relying on lens antenna arrays," *IEEE Journal of Selected Topics in Signal Processing*, Vol. 99, No.1, March 2018.

[34]   F. Sohrabi, W. Yu, "Hybrid analog and digital beamforming for mmWave OFDM large-scale antenna arrays," *IEEE Journal of Selected Areas in Communications*, Vol. 35, No. 7, July 2017, pp. 1432- 1443.

[35]   W. Abbas, M. Zorzi, "Context information based initial cell search for millimeter wave 5G cellular networks," in *2016 European Conference on Networks and Communications (EuCNC)*, June 2016, Athens, Greece.

[36]   A. Capone, I. Filippini, V. Sciancalepore, "Context information for fast cell discovery in mm-wave 5G networks," in *2015 European Wireless Conference (EW)*, May 2015, Budapest, Hungary.

[37]   Millimeter Wave Evolution for Backhaul and Access (MiWEBA) , Channel Modeling and Characterization, FP7-ICT-608637, MiWEBA Project Deliverable D5.1, June 2014. [Online]. Available: http://www.miweba.eu/wp-content/uploads/2014/07/MiWEBA D5.1 v1.01.pdf

[38]   I. Filippini, V. Sciancalepore, F. Devoti, A. Capone, "Fast cell discovery in mmWave 5G networks with context information," *IEEE Transactions on Mobile Computing*, Vol. 99, No. 1, December 2017.

[39]   S. Payami, M. Shariat, M. Ghoraishi, M. Dianati, "Effective RF codebook design and channel estimation for millimeter wave communication systems," in *2015 IEEE International Conference on Communication Workshop (ICCW)*, June 2015, London, UK.

[40]   C. Jeong, J. Park, H. Yu, "Random access in millimeter wave beamforming cellular networks: issues and approaches," *IEEE Communications Magazine*, Vol. 53, No. 1, January 2015, pp. 180-185.

[41]   A. Alkhateeb, O. ElAyach, G. Leus, R. W. Heath Jr, "Channel estimation and hybrid precoding for millimeter wave cellular systems," *IEEE Journal of Selected Areas in Signal processing*, Vol. 8, No. 5, October 2014, pp.831-846.

[42]   L. Zhou, Y. Ohashi, "Fast codebook-based beamforming training for mmWave MIMO systems with subarray structures," *in 2015 IEEE Vehicular Technology Conference (VTC),* September 2015, Boston, MA, USA.

[43]   M. Rahman and K Josiam, "Low complexity RF beam search algorithms for millimeter wave systems," in *2014 IEEE Global Communications Conference (GLOBECOM)*, December 2014, Austin, TX, USA.

[44]   J. Luo, N. Vucic, M. Castaneda, Y. Li, W. Xu, "Initial access assisted by an auxiliary transceiver for millimeter wave networks," in *2017 International Workshop on Smart Antennas (WSA)*, March 2017, Berlin, Germany.

[45]   L. Zhou, Y. Ohashi, "Effective codebook training for mmWave massive MIMO systems with subarray structures," in 2016 *IEEE Vehicular Technology Conference (VTC)*, September 2016, Montreal, Canada.

[46]   C. Barati *et al.*, "Directional cell discovery in millimeter wave cellular networks," *IEEE Transaction on Wireless Communications*, Vol. 14, No. 12, December 2015, pp. 6664-6678.

[47]   Y. QI, M. Nekovee, "Coordinated initial access in millimeter wave standalone networks," in *2016 IEEE Conference on Computer Communications (INFOCOM)*, April 2016, San Francisco, CA, USA.

[48]   C. Balanis, "Arrays: Linear, Planar and Circular," *Antenna Theory: Analysis and Design*, 3rd Ed., John Wiley, 2005, pp. 290-398.

[49]   W. Stutzman, G. Thiele, "Array Antennas," *Antenna Theory and Design*, 3rd Edition, John Wiley & Sons, 2012, pp. 294-295.

[50]   R. Alhalabi, G. Rebeiz, "Design of high-efficiency millimeter wave microstrip antennas for silicon RFIC applications," in *2011 IEEE Antennas and propagation Society International Symposium*, July 2011, Spokane, WA, USA.

[51]   S. Sun *et al.*, "Path loss, shadow fading, and line-of-sight probability models for 5G urban macro-cellular scenarios," in *2015 IEEE Global Communications Conference (GLOBECOM)*, December 2015, San Diego, CA, USA.

[52]   G. MacCartney, T. S. Rappaport, "Path loss models for 5G millimeter wave propagation channels in urban microcells," in *2013 IEEE Global Communications Conference (GLOBECOM)*, December 2013, Atlanta, GA, USA.

[53]   J. Mathews, K. Fink, "Numerical optimization," in *Numerical Methods Using Matlab*, 4th Ed., Prentice Hall, 2004, pp. 430-434.

[54]   J. Nelder, R. Mead, "A simplex method for function minimization" *Computer Journal*, Vol. **7**, No. 4. January 1965, pp. 308-313.

[55]   M. Giordani, M. Mezzavilla, M. Zorzi, "Initial access in 5G mmWave cellular networks," *IEEE Communications Magazine*, Vol. 54, No. 11, November 2016, pp. 40-47.

[56]   R. Méndez-Rial *et al.*, "Channel estimation and hybrid combining for mmWave: phase shifters or switches?" in *Information Theory and Applications Workshop* (ITA), February 2015, San Diego, CA, USA.

[57]   J. Andrews *et al.*, "Modeling and analyzing millimeter wave cellular systems**,**" *IEEE Transactions on Communications*, Vol. 65, No. 1, Jan. 2017, pp. 403-430.

[58]   W. Yuan, S. Armour, A. Doufexi, "An efficient and low complexity beam training technique for mmWave communication," in *2015 IEEE International Symposium on Personal*, *Indoor and Mobile Radio Communications (PIMRC)*, September 2015.

[59]   R. Luus, T Jaakola, "Optimization by direct search and systematic reduction of the size of search region," *American Institute of Chemical Engineers Journal*, Vol. 19, No. 4, 1973, pp. 760-766.

[60]   F. Glover, "Future paths for integer programming and links to artificial intelligence," *Computers and Operations Research*, Vol. 13, No. 5, 1986, pp. 533-549.

[61]   X. Chen, J. Xu, "New method for millimeter wave signal high sensitivity receiving and testing in range," *International Journal of Computer and Electrical Engineering*, Vol. 5, No. 4, 2013, pp. 1-2.

[62]   J. Dennis, V. Torczon, "Derivative-free pattern search methods for multidisciplinary design problems," in *5th Symposium on Multidisciplinary Analysis and Optimization*, September 1994, Panama City Beach, FL, USA.

[63]   R. Hooke, T. Jeeves, "Direct search solution of numerical and statistical problems," *Journal of the Association for Computing Machinery*, Vol. 8, No. 2, April 1961, pp. 212-229.

[64]   J. Chinneck, Practical Optimization: A Gentle Introduction [Online]. Available: http://www.sce.carleton.ca/faculty/chinneck/po.html. Ch. 17.

[65]   A. Tang, Q. Gu, M. Chang, "CMOS Receivers for Active and Passive mm-Wave Imaging," *IEEE Communications Magazine*, Vol. 49, No. 19, 2011, pp. 190-198.

[66]   C. Balanis, "Arrays: Linear, Planar and Circular," *Antenna Theory: Analysis and Design*, 3rd Ed., John Wiley, 2005, pp. 300-301.

[67]   M. Jasim, N. Ghani, "Fast beam discovery for mmWave cellular networks," in *2017 IEEE Wireless and Microwave Technology Conference (WAMICON)*, Cocoa Beach, FL, USA, April 2017.

[68]   M. Jasim, N. Ghani, "Adaptive initial beam search for sparse millimeter wave channels," in *Wireless and Optical Communication Conference (WOCC)*, Newark, NJ, USA, April 2017.

[69]   M. Jasim, N. Ghani, "Generalized pattern search for beam discovery in millimeter wave systems," in *2017 IEEE 86th Vehicular Technology Conference (VTC-Fall)*, Toronto, Canada, Sept. 2017.

[70]   M. Jasim, A. Aldalbahi, A. Khreishah, N. Ghani, "Hooke Jeeves search method for initial beam access in 5G mmWave cellular networks", in *2017 IEEE International Symposium on Personal, Indoor and Mobile Radio Communications (PIMRC)*, Montreal, Canada, October 2017.

[71]   M. Jasim, N. Ghani, "Sidelobe exploitation for beam discovery in line of sight millimeter wave systems", *IEEE Wireless Communications Letters*, Vol 7, No. 2, April 2018, pp. 234-237.

[72]   N. Fourikis, "From array theory to shared aperture arrays," in Advanced Array Systems: Applications and RF Technologies, 1st Edition, Academic Press, 2000, pp. 116-117.

[73]   A. Brown, "Electronically scanned array fundamentals" in Electronically Scanned Arrays MATLAB Modeling and Simulation, 1st Edition, CRC Press, 2012, pp. 10-11.

[74]   Y. Tsang, A. Poon, S. Addepalli, "Coding the beams: Improving beamforming training in mmWave communication system," in *IEEE Global Communications Conference (GLOBECOM)*, December 2011, Houston, TX, USA.

[75]   R. Haupt, "Array factor analysis" in *Antenna Arrays: A Computational Approach*, 2nd Ed., John Wiley & Sons, 2010, Ch. 2, Sec. 2.6, pp. 78-81.

[76]   T. D. Rappaport *et al.*, "Channel reliability due to human blockage," in Millimeter Wave Wireless Communications, 1st Edition, Prentice Hall, 2014, pp. 503-504.

[77]   B. Gao *et al.*, "Double-link beam tracking against human blockage and device mobility for 60-GHz WLAN," in *2014 IEEE Wireless Communications and Networking Conference (WCNC)*, May 2014, Istanbul, Turkey.

[78]   T. Bai, V. Desai, R. W Heath, "Millimeter wave cellular channel models for system evaluation", in *2014 International Conference on Computing*, *Networking and Communications (ICNC)*, Honolulu, HI, USA, February 2014.

[79]   I. Sulyman, A. T. Nassar, M. K. Samimi, G. R. MacCartney, T.S. Rappaport, and A. Alsanie, "Radio propagation path loss models for 5G cellular networks in the 28 GHz and 38 GHz millimeter-wave bands", *IEEE Communications Magazine*, Vol. 52, No. 9, 2014, pp. 78-86.

Appendices

Appendix A: Glossary of Terms

AOA   *angle of arrival*

AOD   *angle of departure*

AWGN   *additive white Gaussian noise*

ADC   *analog-to-digital-converts*

AWV   *antenna weight vectors*

BS   *base stations*

AMP   *baseband amplifier*

BB   *baseband combiner*

BSC   *bi-static cross section*

BRCS   *bi-static radar cross section*

CGPS   *coordinated generalized pattern search*

CSI   *channel state information*

CP   *cyclic prefix*

CW   *clockwise*

CCW   *counter-clockwise*

CCI   *co-channel interference*

CAZAC   *constant amplitude zero auto-correlation*

DC-TS   *divide-and-conquer* with *Tabu search*

DIC   *data interface cards*

DB   *dual-beam*

DGS   *discovery greedy search*

DoF   *degree of freedom*

DAC   *digital-to analog-concerts*

DB-ABF   *dual-beam analog beamformer*

EIRP	*effective isotropic radiated power*
EDP	*enhanced discovery procedure*
EGC	*equal-gain combining*
eNodeB	*evolved NodeB*
eMBB	*enhanced mobile broadband*
EHF	*extremely high frequency*
FCC	*Federal Communications Commission*
FSLL	*first sidelobe levels*
FDMA	*frequency division multiple access*
GPS	*global positioning systems*
HJ	*Hooke Jeeves*
HBF	*hybrid beamforming*
HPBW	*half-power beamwidth*
ISI	*inter-symbol interference*
IMT	*International Mobile Telecommunications*
IR	*impulse response*
LTE	*long term evolution*
LTE-A	*LTE-Advanced*
LJ	*Luus Jaakola*
LoS	*line-of-sight*
LO	*local oscillator*
LPF	*low pass filter*
LNA	*low-noise amplifiers*
MIB	*master information block*
mmSCs	*mmWave small cells*

MB-ABF   *multi-beam analog beamforming*

M   *mixer*

MIMO   *multiple-input multiple-output*

mmWave   *millimeter wave*

MM   *Main lobe-to-main lobe*

MCS   *monostatic cross section*

MS   *mobile station*

MRC   *maximal ratio combining*

MPC   *multipath components*

mWatts   *milliwatts*

NM   *Nelder Mead*

NR   *new radio*

NLoS   *non-line-of-sight*

OFDM   *orthogonal frequency-division multiplexing*

PDP   *power delay profiles*

PLE   *path loss exponents*

PDF   *probability distribution function*

PDP   *power delay profile*

PA   *power amplifiers*

PSS   *primary synchronization signal*

QAM   *quadrature amplitude modulation*

RCS   *radar cross section*

RRH   *remote radio heads*

RF   *radio frequency*

RMS   *root mean square*

SNR	*signal-to-noise ratio*
SSS	*secondary synchronization signal*
SLL	*side lobe levels*
SoI	*signal of interest*
SM	*sidelobe-to-main lobe*
SS	*sidelobe-to-sidelobe*
SB-ABF	*single-beam analog beamforming*
SRCS	*secondary reference control signal*
SIB	*system information blocks*
TDD	*time-division duplexing*
3GPP	*3rd Generation Partnership Project*
TWDP	*two-wave with diffuse power*
TDM	*time-division multiplexing*
UHF	*ultra-high frequencies*
UE	*user equipment*
VCO	*voltage-controlled oscillators*
VN	*Von Neumann*

Appendix B: Copyright Notices

Permissions below are the permissions for the use of material in Chapters 3 and 4 of this

dissertation.

IEEE Requesting permission to reuse content from an IEEE publication	**Title:**	Adaptive initial beam search for sparse millimeter wave channels	Logged in as: Mohammed Jasim
	Conference Proceedings:	Wireless and Optical Communication Conference (WOCC), 2017 26th	LOGOUT
	Author:	Mohammed Jasim	
	Publisher:	IEEE	
	Date:	April 2017	
	Copyright © 2017, IEEE		

Thesis / Dissertation Reuse

The IEEE does not require individuals working on a thesis to obtain a formal reuse license, however, you may print out this statement to be used as a permission grant:

Requirements to be followed when using any portion (e.g., figure, graph, table, or textual material) of an IEEE copyrighted paper in a thesis:

1) In the case of textual material (e.g., using short quotes or referring to the work within these papers) users must give full credit to the original source (author, paper, publication) followed by the IEEE copyright line © 2011 IEEE.
2) In the case of illustrations or tabular material, we require that the copyright line © [Year of original publication] IEEE appear prominently with each reprinted figure and/or table.
3) If a substantial portion of the original paper is to be used, and if you are not the senior author, also obtain the senior author's approval.

Requirements to be followed when using an entire IEEE copyrighted paper in a thesis:

1) The following IEEE copyright/ credit notice should be placed prominently in the references: © [year of original publication] IEEE. Reprinted, with permission, from [author names, paper title, IEEE publication title, and month/year of publication]
2) Only the accepted version of an IEEE copyrighted paper can be used when posting the paper or your thesis on-line.
3) In placing the thesis on the author's university website, please display the following message in a prominent place on the website: In reference to IEEE copyrighted material which is used with permission in this thesis, the IEEE does not endorse any of [university/educational entity's name goes here]'s products or services. Internal or personal use of this material is permitted. If interested in reprinting/republishing IEEE copyrighted material for advertising or promotional purposes or for creating new collective works for resale or redistribution, please go to http://www.ieee.org/publications_standards/publications/rights/rights_link.html to learn how to obtain a License from RightsLink.

If applicable, University Microfilms and/or ProQuest Library, or the Archives of Canada may supply single copies of the dissertation.

149

About the Author

Mohammed Jasim was born in Baghdad, Iraq in 1987. He earned his bachelors degree in Communications & Electronics Engineering with honors from the Applied Science University (Amman, Jordan) in 2010. He obtained his masters degree with distinction in Wireless Communications Systems from Brunel University (London, United Kingdom) in 2010. He started his doctoral studies in 2014, in the Department of Electrical Engineering at the University of South Florida (Florida, United States) majoring in Wireless Communication Systems. His research interests include cellular networks, millimeter wave communications, phased arrays, beamforming, sparsity recovery, in addition to direct pattern search methods and network function virtualization.